

ANISOTROPIC NEUTRON IMAGING

A Dissertation

by

CAROL GWYN ROSAIRE IV

Submitted to the Office of Graduate and Professional Studies of
Texas A&M University
in partial fulfillment of the requirements for the degree of

DOCTOR OF PHILOSOPHY

Chair of Committee,	Pavel V. Tsvetkov
Co-Chair of Committee,	Shannon Bragg-Sitton
Committee Members,	Donald G. Naugle
	Ryan G. McClarren
	Sean McDeavitt
Head of Department,	Yassin Hassan

May 2016

Major Subject: Nuclear Engineering

Copyright 2016 Carol Gwyn Rosaire IV

ABSTRACT

Anisotropic neutron imaging presents a unique method to process images in order to produce a human-readable, singular, isotropic image from a set of anisotropic neutron images. These images were created using a Söller-slit collimator in a rotating device to change the azimuthal orientation of the slits with respect to the imaging plane. A multi-level, 2D-discrete wavelet transform (2D-DWT) was used to extract the information contained within each image and fuse the data into an isotropic resolution image.

The footprint of the experimental system is small when compared to other neutron radiography facilities of comparable L/D and has the advantage of a relatively low acquisition time while maintaining high resolution image capture. The 2D-DWT algorithm developed within this dissertation is able to enhance the sharpness of the edges within the final image and remove the artifacts created by the slit-type collimator, which increased human readability in the test circumstance.

DEDICATION

This dissertation is dedicated to all who would question the world around them and put to test, to see the truth for themselves. Do not be afraid, for the universe holds the answer and is waiting for the right question. Explore, dream, and discover the universe.

Ode to the Neutron

With the first flash of light
into the Universe,
she birthed your might

Arbiter of forces strong and weak,
you are not lonely for long,
and your mass is deceptively meek
POOF! Proton and electron!

Alas, the Neutron hides in all matter.
With polonium and beryllium
Neutrons are offered on a platter.

To find your power,
it took a mighty cranium,
and in our darkest hour
we threw you at uranium.

Bockscar makes her dash;
we unleash the supernova.
With another flash
Behold! The power of Jehovah!

Fission was your mission, Servant,
but we repent.
The world never forgets this grievance.
It is not your fault for this malfeasance.

Astronomers bore witness,
through you, we have nucleosynthesis.
Finally, the long sought after alchemy,
with you, we can probe atom anatomy.

You still hold promise,
a savior of all humankind
and here I find solace.
The people must not be blind.

Neutron, you must release that energy.
For woes, you hold the remedy.
If only the world could see what I see:
your perfect synergy.

I can only see you indirectly,
for my eyes detect radiation ineptly,
but I can see your pride
you interact with lithium and zinc
sulfide.

What? You made me an image?
You are so sweet!
Now, I take my leave for I must
scrimmage.
Off to my professor, I must meet.

ACKNOWLEDGEMENTS

I would like to thank Dr. Pavel Tsvetkov for supporting me through this journey to find an experimentally focused topic. If it were not for Dr. Shannon Bragg-Sitton, I would not have had the chance to prove myself in the department to be a stellar student. I credit you, Shannon, for all of the wonderful things that have happened since.

I would like to thank Dr. Donald Naugle for allowing me the opportunity to overcome a mistake I made while working in his lab, and trusting that I would never make the same mistake twice. His and Daya Rathnayaka's mentorship during my undergraduate years helped mold me into a skilled young scientist with the ability to form apparatus from formless stock as an artist would sculpt a masterpiece from stone.

Dr. Radek Skoda gave me funding and a project that utilized all of my talents along with the encouragement to determine my own direction. I would like to thank Dr. Sean McDeavitt for graciously extending support for my project, its funding, and access to the Nuclear Science Center. Jerry Newhouse was an indispensable source of assistance. Without him, it would have been impractical to perform many of the experiments. I would like to also thank Victor Vlassov for his help during the renovation and construction of the experimental system.

NOMENCLATURE

ARRT	Anisotropic Resolution Reconstruction Techniques
BR	Branching ratio
CCD	Charge Coupled Device
CT	Computed Tomography
CWT	Continuous Wavelet Transform
DIO	Digital input/output
DoE	Department of Energy
DPF	Diesel Particulate Filter
DWT	Discrete Wavelet Transform
HPGe	High Purity Germanium
IDWT	Inverse Discrete Wavelet Transform
FFT	Fast Fourier Transform
LSF	Line Spread Function
LoG	Laplacian of a Gaussian
MeV	Megaelectron volts
MTF	Modulation Transfer Function
NAA	Neutron Activation Analysis
NASA	National Aeronautics and Space Administration
NDS	Neutron Detection Screen
NIS1	Neutron Imaging System 1

NIS2	Neutron Imaging System 2
NMRI	Nuclear Magnetic Resonance Imaging
ORNL	Oak Ridge National Laboratory
OS	Operating System
OTF	Optical Transfer Function
PSF	Point Spread Function
RMS	Root-mean-squared
ROI	Region of Interest
SNM	Special Nuclear Material
SNR	Signal-to-noise ratio
TEES	Texas Engineering Experiment Station
Variables	
A_0	Activity of sample immediately after irradiation
A_1	Measured activity of sample
A_∞	Saturation activity
f	Image or 2-D field
f_I	Image field
f_P	Sampled image
G	Gaussian function
I_0	Resonance integral Cross Section
j	Imaginary unit
m	Sample mass

N	Number of atoms
r	Radius
R	Reaction rate
t	Time
t_0	Point in time immediately after irradiation
t_1	Point in time of activity measurement
$T_{1/2}$	Half-life
S	Sampling function
V	Volume of sample
x	X coordinate
y	Y coordinate
σ	Standard deviation
σ_0	Thermal absorption cross section
Σ_{act}	Activation cross section
λ	Decay constant
ρ	Sample density
ϕ	Neutron flux
ψ	Wavelet
$\hat{\psi}$	Wavelet mean

TABLE OF CONTENTS

	Page
ABSTRACT	ii
DEDICATION	iii
ACKNOWLEDGEMENTS	iv
NOMENCLATURE	v
TABLE OF CONTENTS	viii
LIST OF FIGURES	xi
LIST OF TABLES	xvii
1. INTRODUCTION.....	1
1.1. Proposed Method.....	1
1.2. Dissertation Objectives	2
2. NEUTRON IMAGING COMPONENTS AND THEORY	4
2.1. Neutron Sources	4
2.1.1. Fission Sources.....	4
2.1.2. Accelerator Sources.....	5
2.1.3. Fusion Sources	6
2.1.4. Radioisotope Decay Sources	7
2.2. Neutron Optics	9
2.3. Neutron Detection	11
2.4. Neutron Imaging Methods	13
2.4.1. Limitations	15
2.4.2. Recent Advances in Neutron Imaging	15
2.5. Neutron Imaging Applications	17
3. RECONSTRUCTION ALGORITHM AND IMAGE PROCESSING.....	28
3.1. Image Sampling.....	28
3.2. Digital Image Filters.....	32
3.2.1. Edge Detection and Enhancement.....	32
3.2.2. Gamma Radiation-Induced Noise Filtration	35
3.2.3. Optical Transfer Function	37

3.2.4.	PSF	37
3.2.5.	LSF	38
3.2.6.	MTF.....	38
3.2.7.	Image Registration and Alignment	40
3.3.	FFT	42
3.4.	Discret Wavelet Transform (DWT).....	44
3.5.	Anisotropic Resolution Neutron Image Reconstruction	51
3.6.	Development of the Combined DWT and ARRT.....	53
3.6.1.	One Level 2-D DWT MatLab Method.....	54
3.6.2.	Bayesian Inference DWT Method.....	55
3.7.	Multilevel DWT Edge Enhancement	60
3.8.	Multilevel DWT Artifact Rejection	62
3.9.	Image Reconstruction Test Image.....	64
3.9.1.	Test Image Objects.....	64
3.9.2.	Simulated Anisotropic Blur and Noise.....	66
3.9.3.	DWT Reconstruction Method Results	67
3.10.	Implementation of the Developed Reconstruction Algorithm	74
4.	EXPERIMENTAL SETUP AND MEASUREMENTS.....	76
4.1.	Layout.....	76
4.2.	Beam Port Cave Renovations.....	77
4.2.1.	Cave Assessment.....	78
4.2.2.	Film Equipment Removal	80
4.3.	Experimental System Setup	86
4.3.1.	Neutron Collimator	87
4.3.2.	Neutron Imaging System 1.....	88
4.3.3.	Neutron Imaging System 2.....	92
4.4.	Data Acquisition System.....	93
4.4.1.	Computer.....	95
4.4.2.	Digital Input/Output (DIO) Device	95
4.4.3.	System Articulation.....	96
4.4.4.	XY Positioning System	96
4.4.5.	Collimator Positioning	97
4.4.6.	Camera and Lens	99
4.4.7.	Neutron Scintillation Screen	100
4.5.	Neutron Beam Flux Measurements.....	100
4.5.1.	NAA Procedure	102
4.5.2.	Measurements for Flux Determination	110
4.5.3.	Cadmium Ratio	111
4.6.	Neutron Image Data	112
5.	RESULTS AND DISCUSSION	115

5.1.	Preprocessing	115
5.2.	Simple Linear Combination	120
5.3.	Discreet Wavelet Transformation	121
5.3.1.	One-level DWT	122
5.3.2.	Cauchy Distribution and One-level DWT.....	123
5.3.3.	Multilevel DWT Artifact Rejection	124
5.3.4.	Multilevel DWT Artifact Rejection Wavelet Sensitivity	125
5.3.5.	Multilevel DWT Edge Enhancement	125
5.3.6.	Multilevel DWT Edge Enhancement Wavelet Sensitivity.....	127
5.4.	Data Analysis Summary.....	129
6.	CONCLUSIONS AND FUTURE WORK.....	131
	REFERENCES	133
	APPENDIX A	138
	Test Items	138
	Undergraduate Laboratory Items	148
	Zircaloy Cladding Samples	156
	APPENDIX B	160
	APPENDIX C	163

LIST OF FIGURES

	Page
Figure 1. TEES-NSC reactor operating at 1 MW, shown with the coupler box, neutron shutters, beam tubes, and thermal column.....	5
Figure 2. Divergent collimator.....	10
Figure 3. Söller (left) and honeycomb (right) collimators, both manufactured by EuroCollimators Ltd [13].	10
Figure 4. Neutron absorption cross sections for select isotopes [18].....	12
Figure 5. Neutron images of irradiated nuclear fuel produced at the Neutron Radiography reactor (NRAD) using dysprosium (left) and indium (right) conversion foils [25].....	18
Figure 6. (a) 3D uneven hydrogen (colored in red) distribution in a hydrided Zircaloy-4 cladding sample, (b) top-view neutron image of oxidized Zircaloy-4 ring sample showing high hydrogen concentrations in the middle, (c) plot of the ring sample's neutron intensity vs. hydrogen content [26].....	19
Figure 7. PEM fuel cell flow channel water blockage [27].....	20
Figure 8. Series of neutron images depicting the startup and operation of a heat pipe over several power ranges [28].....	22
Figure 9. Neutron imaging sequence during foam expansion and ageing [29].....	23
Figure 10. Sagittal slices through the tomographic reconstructions. (a) The total attenuation coefficients of (a) the empty bed, (b) the bed filled with 94.5 L of D ₂ , and (c) the bed after desorbing approximately 60 L of D ₂ . Black and white correspond to attenuation coefficients of 0 cm ⁻¹ and 1.0 cm ⁻¹ , respectively. Subtracting the empty bed attenuation coefficient yields the D content of the bed: (d) after the absorption of approximately 100 L and (e) after desorption of approximately 60 L of D ₂ [30].....	24
Figure 11. X-ray image of a diesel particulate filter (top left) [32], neutron tomograph (bottom left) with a 40 μm resolution [33], and a diesel injector (right) taken at ORNL in April 2012 with 75 μm resolution.....	25
Figure 12. Dirac delta function sampling array.....	29

	Page
Figure 13. Signal and noise impacts on measurements.....	31
Figure 14. LoG filter with a standard deviation of 1.....	35
Figure 15. One-dimensional representation of the MTF illustrating the ability of an imaging system to reproduce the input according to the spatial frequency spectrum [43].....	39
Figure 16. Daubechies 4 wavelet decomposition and reconstruction filters.....	51
Figure 17. Data associated with 2 anisotropic NMRI scans and the reference image from which the two images were formed [50].....	52
Figure 18. One-Level, 2D-DWT reconstruction process.....	54
Figure 19. One level Bayesian inference DWT method.....	55
Figure 20. Cauchy distribution derivation concept.....	56
Figure 21. Cauchy distribution of intensity values.....	59
Figure 22. Edge enhancement DWT decomposition and reconstruction process.....	61
Figure 23. Artifact rejection DWT decomposition and reconstruction process.....	63
Figure 24. Ground truth image before degradation.....	65
Figure 25. ROI for the initial image before degradation.....	65
Figure 26. X-direction blur (left); Y-direction blur (right).....	66
Figure 27. ROI for test images.....	67
Figure 28. Image reconstruction using the simple two-dimensional DWT method using the built-in MatLab functions.....	68
Figure 29. ROI for one-level, 2D-DWT reconstruction method.....	69
Figure 30. Wavelet reconstruction (left), image average (right).....	70
Figure 31. ROIs for Haar wavelet reconstruction (left) and average (right).....	70
Figure 32. ROI close up comparison of the reconstruction method and average of the two images.....	71

	Page
Figure 33. Approximation cascade.....	72
Figure 34. Sensitivity of wavelet complexity.....	73
Figure 35. ROI of off angle edges.	74
Figure 36. General layout of the neutron radiography facility at the TEES NSC.....	77
Figure 37. Measurement of the width of the perpendicular portion of the radiography cave.....	79
Figure 38. Measurement of the height of the perpendicular portion of the radiography cave.....	80
Figure 39. Neutron radiography film tray and trolley track rack.	81
Figure 40. Hydraulic vertical lift support blocks.	82
Figure 41. View of the radiography cave as seen from the beam port opening.....	84
Figure 42. Portion of the shielding wall that was removed to allow the removal of the neutron radiography film tray and trolley track rack.	85
Figure 43. View from inside the perpendicular portion of the cave after the removal of the film tray and trolley track rack.	86
Figure 44. Collimator A (left) and Collimator B (right).	88
Figure 45. Lower camera rack frame with precision sliding track.....	88
Figure 46. Assembled camera rack with front surface mirror mount and camera sled.....	90
Figure 47. Side-view of the assembled camera rack with mirror mount.	91
Figure 48. Images of the NIS1 with the scintillator and holder (left) and the camera and sled (right).	92
Figure 49. Experimental, high-resolution neutron camera, NIS2.	93
Figure 50. Conceptual representation of the neutron imaging data acquisition and control system.....	95
Figure 51. Stepper motor driver board and the added pull down resistors.	97

	Page
Figure 52. Micro-stepper driver for the collimator rotator. This driver is capable of 1/64th step sizes.....	98
Figure 53. Left to right, the stepper motor driver, the NI USB DIO, and the Arduino board that was used as a power supply for the signal amplifier.....	99
Figure 54. Nikon AF-S Nikkor 70-200mm f/2.8 ED VR-II lens.	100
Figure 55. Total interaction cross-section and radiative capture cross-sections for natural cadmium [17].....	102
Figure 56. Radioisotope buildup and decay curve.	106
Figure 57. Mass measurement scale.....	108
Figure 58. Detail of placement of the activation foils on the sample holder.	109
Figure 59. Location of the Au foils in the beam port.	110
Figure 60. Unfiltered images with the collimator in the horizontal orientation.....	113
Figure 61. Unfiltered images with the collimator in the vertical orientation.	114
Figure 62. Filtered images with the collimator in the horizontal orientation.....	117
Figure 63. Filtered images with the collimator in the vertical orientation.	118
Figure 64. Unfiltered and unnormalized signals.	119
Figure 65. Filtered and normalized signals.	120
Figure 66. Simple linear average of neutron images.....	121
Figure 67. Daubechies 20, one-level wavelet decomposition.	122
Figure 68. Cauchy distribution Bayesian method.	123
Figure 69. Daubechies 8 wavelet method	124
Figure 70. Artifact rejection wavelet sensitivity.	126
Figure 71. Edge enhancement using Daubechies 8 wavelet method.	127
Figure 72. Sensitivity of image reconstruction to Wavelet complexity.	128

	Page
Figure 73. Comparison of images before reconstruction and post reconstruction structures.....	129
Figure 74. Cell phone (left) and hard disk drive (right).	139
Figure 75. Cathode ray tube television.....	140
Figure 76. Ion chamber beta and gamma radiation detector (without batteries).....	141
Figure 77. Two-stroke leaf blower motor with the outer plastic shroud removed.	142
Figure 78. 3/8" socket driver inside of an aluminum tube.	143
Figure 79. Micropixel neutron camera (left), Swagelok valve (middle), heat pipe (right).	144
Figure 80. Open field image.....	145
Figure 81. Diesel particulate filter.....	146
Figure 82. Normalized image using the ratio of the object image to the open field image.....	147
Figure 83. BIC lighter with butane lighter fuel.	148
Figure 84. TI-89 calculator.....	149
Figure 85. Charger and rubber ball.	150
Figure 86. Battery operated drill.	151
Figure 87. Television remote.	152
Figure 88. Desktop graphics card (left) and an XBOX 360™ controller (right).	153
Figure 89. Ion chamber beta and gamma radiation detector.	154
Figure 90. Safe combination lock.	155
Figure 91. Master lock (left), wrist watch (middle), safe combination lock (right).....	156
Figure 92. Raw image of the two Zircaloy samples.....	157
Figure 93. Open field image used to normalize the final image.	158

Figure 94. Zircaloy control (left) and hydrided Zircaloy (right) samples. 159

LIST OF TABLES

	Page
Table 1 Radioisotopes for Neutron Sources.....	8
Table 2 Degradation Parameters	67
Table 3 Gold Neutron Absorption Cross-Section Values	107
Table 4 Measured Values for Neutron Flux Determination.....	111
Table 5 Neutron Flux Values	111
Table 6 Outlier Filter Values.....	115

1. INTRODUCTION

Neutron imaging is an important tool for non-destructive testing (NDT) and investigation of materials for industrial, academic, military applications, and research [1]. Neutrons interact with the nucleus of the atoms of materials, which gives the neutral fundamental particle its peculiar properties. Neutrons can penetrate materials that are opaque to x-rays to yield images superior to x-rays for that specific object. Neutrons can be used to interrogate special nuclear materials (SNM) with suitable detectors. Digital neutron images are often lower resolution than their x-ray counterparts and suffer from a low signal-to-noise ratio (SNR). Methods to improve the SNR and the resolution of the imaging system, while minimizing data acquisition time, are the focus of this dissertation. The discrete wavelet transform is a signal processing technique with broad applications: if the data can be graphed with two or more variables, it can be processed by discrete wavelet transformation (DWT) methods. The use of high and low-pass filters allows the decomposition of a set of anisotropic-resolution images into the high resolution and low resolution components of the images set. It is then possible to recombine the high or low resolution components into a single high resolution image (edge enhancement) or low resolution image (improved noise and artifact rejection).

1.1. Proposed Method

A method is proposed to use discrete wavelet transforms (DWT) to parse the relevant detail from each anisotropic image set. Anisotropic resolution reconstruction

techniques (ARRT) utilizing DWTs have yet to be envisioned for a neutron radiography system in conjunction with the high admittance, high aspect ratio collimator; this method has the potential to reduce the acquisition time of high-resolution neutron imaging.

1.2. Dissertation Objectives

The objective of this dissertation is to develop a new neutron radiographic method that uses a high-luminosity, highly-anisotropic beam structure to acquire fine structure data on a quantifiable basis and demonstrate anticipated fast acquisition times associated with the method. This method is a novel form of neutron imaging in that multiple images are acquired with orthogonal, anisotropic resolution to reconstruct an image that would otherwise be unobtainable within the same time frame. The algorithm is based on a discrete wavelet transform used for image compression that decomposes the image into orthogonal subsets of detailed information with a diagonal correlation. It was developed from the standpoint of acquisition of orthogonal image data that is used to reconstruct an isotropic, higher resolution image. The objective of the work was to perform a full reconstruction on an electronic circuit board of suitable size and materials construction. The resultant image was then compared to the human readability of the original dataset and the linear average of the dataset. The method and objectives are summarized in the following list.

1. Develop a method based on DWT to decompose an orthogonal image dataset into its fundamental constituents.
2. Develop a system to utilize a high-luminosity, highly anisotropic collimator.

3. Perform image reconstructions using the developed DWT method to demonstrate its performance.
4. The proposed method should be noticeably better than a simple linear average of the two datasets.

2. NEUTRON IMAGING COMPONENTS AND THEORY

The components of a neutron imaging system can be broken down into three main subsystems: the neutron source, neutron optics, and the neutron detection system. Of these three subsystems, the neutron detection system has received the most attention, followed by beam collimation, and finally the neutron source receiving little attention at all. Improving neutron sources has proven to be the most difficult of these three components due to the technological and financial complexities of these systems [2].

2.1. Neutron Sources

Neutron sources can be grouped into four general classes: fission, decay, fusion, or spallation. The fission class is simply a nuclear reactor in which part of its reflector is coupled (neutronically) to a beam port in which the neutrons are allowed to stream out of the reflector and down a tube to the neutron collimator. Nuclear reactors have been successfully used for neutron imaging for the past six decades and have been extensively used for NDT for the past four decades. More recently, spallation neutron sources have been used successfully to produce high neutron fluxes for quality images [3].

2.1.1. *Fission Sources*

Nuclear reactor sources are typically large facilities that are expensive to operate but offer the best luminosity, and, therefore, the best resolution performance. The reactor has another advantage over the other methods in that the core is typically moderated to

facilitate the fission process; therefore, it does not lose additional neutrons to the moderation process [2]. As of this writing, there are 68 research reactors worldwide that are set up to perform neutron imaging at the commercial level [4]. Due to the “under construction” state of the radiography facility at the TEES-NSC, it is not included in the list of neutron imaging facilities worldwide. Figure 1 shows a picture of the beam port coupler box and reactor at full power at the TEES-NSC. The experimental system is located down the beam tube to the right of the coupler box.

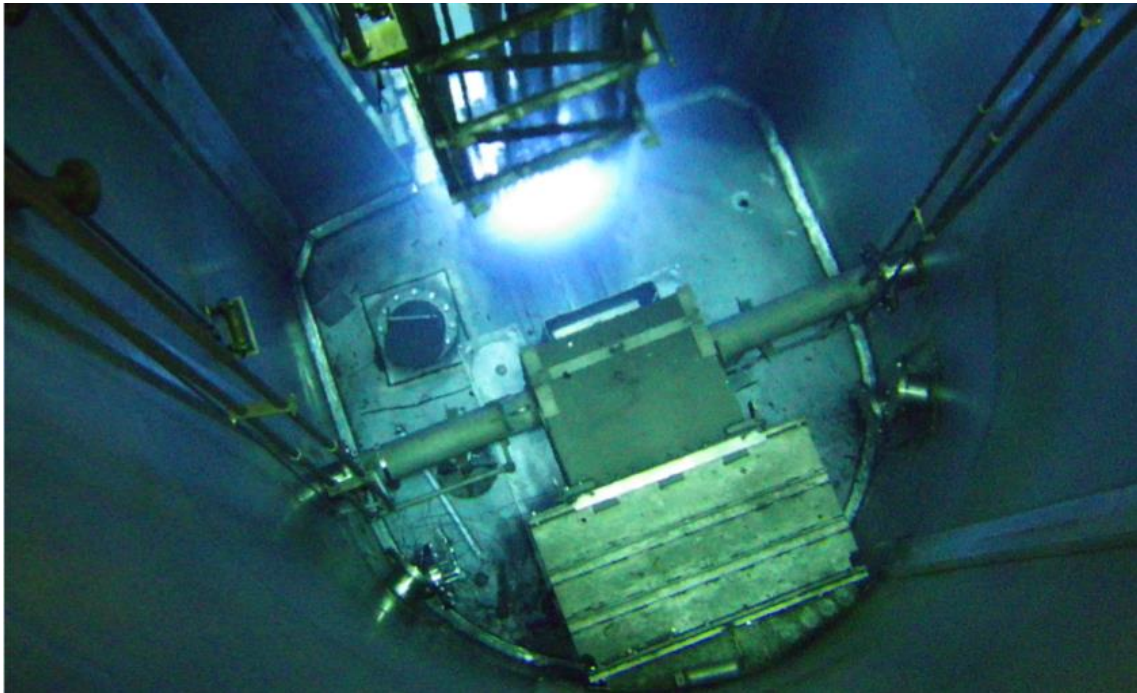


Figure 1. TEES-NSC reactor operating at 1 MW, shown with the coupler box, neutron shutters, beam tubes, and thermal column.

2.1.2. Accelerator Sources

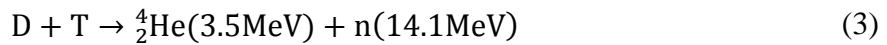
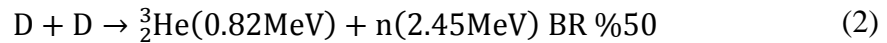
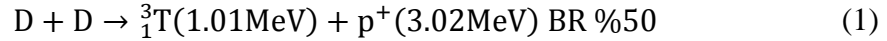
A spallation neutron source requires a much more elaborate system of linear accelerators that accelerate protons to energies greater than 500 MeV that then collide

with a heavy metal target such as mercury, lead, bismuth, tantalum, or tungsten [2], [5]. These methods produce neutrons with energies in the MeV range; hence they must be moderated to thermal and epithermal energy ranges for practical imaging [2]. Spallation neutron sources can be relatively simple when compared to a nuclear reactor. The main drawback of spallation sources is that neutron flux is limited by spallation beam intensity [6].

2.1.3. Fusion Sources

The most common use of fusion neutron generators is for compact, portable neutron sources for moisture content monitoring of soil. Fusion neutron sources typically use an electrostatic ion accelerator in a mixture of deuterium (D) or deuterium-tritium (D-T) gas that produces (nearly) monoenergetic 2.45 or 14.1 MeV neutrons, respectively [7]. Fusion neutron sources require high voltages and vacuum chambers to produce the necessary ion beams or hot plasmas. These systems, in general, require the relatively rare isotopes of hydrogen: deuterium D and tritium (T). Deuterium can be isolated from natural water, but tritium must be produced in a fission or fusion reactor. Other neutron producing fusion fuels are available, but the D-D and D-T reactions are by far the most common neutron-producing fusion fuels [8]. The kinematic analysis of these two fusion neutron source fuels is simplified due to the two-body nature of the fusion products. This gives very sharp peaks about the neutron energies with a Maxwellian distribution that is determined by the fusing plasma temperature. However, D-D plasma has two competing reactions that occur on nearly a 1:1 branching ratio (BR); one reaction path produces an

energetic neutron, while the other produces an energetic proton. These reactions are provided in Eq. (1)-(3) with the reaction Q-values.



2.1.4. Radioisotope Decay Sources

The first neutron source was an (α , n) source that used ${}^{210}\text{Po}$ as the alpha emitter and a beryllium target. Decay sources can be a spontaneous fission isotope such as ${}^{252}\text{Cf}$, a photoneutron source such as a $\text{D}(\gamma, \text{n})\text{H}$ reaction, or an (α , n) type source in which an alpha emitter (i.e. ${}^{238}\text{Pu}$) is mixed with beryllium [2]. Decay neutron sources have the advantage of typically being small, simple, and portable, but they have the major disadvantages of limited thermal neutron fluxes and degraded output from the deterioration of the target material and decay of the source. The lack of the ability to turn off the neutron source is also considered a disadvantage [2].

There are four main isotopes that are found in various (α , n) sources which are ${}^{238}\text{Pu}$, ${}^{239}\text{Pu}$, ${}^{241}\text{Am}$, and ${}^{244}\text{Cm}$. Pu-238 is no longer produced in the US although the National Aeronautics and Space Administration (NASA) and the Department of Energy (DoE) laboratories Oak Ridge National Laboratory (ORNL) and Idaho National

Laboratory (INL) are restarting production for radioisotope batteries for space exploration [9]. Am-241 is the most common alpha emitter used for modern (α , n) neutron sources, and ^{252}Cf is the only spontaneous fission neutron source that can give sufficient neutron strength for practical neutron imaging purposes. The table below was compiled from several sources to give the reader a better understanding of what is possible with radioisotope neutron sources [10].

Table 1 Radioisotopes for Neutron Sources

Source	Decay Emission	$T_{1/2}$	Practical Emission (n·s ⁻¹ Ci ⁻¹)
Cm-242	Alpha	163d	3.0×10^6
Th-228	Alpha	1.91y	2.0×10^7
Cm-244	Alpha	18.1y	2.5×10^6
Ac-227	Alpha, Beta	21.8y	2.0×10^7
Pu-238	Alpha	87.7y	2.2×10^6
Am-241	Alpha	432.2y	2.2×10^6
Cf-252	SF~3.1%; Alpha~96.9%	2.65y	4.3×10^9

It can be seen from Table 1 that radioisotope sources offer neutron fluxes that are several orders of magnitude less than fission reactor sources.

2.2. Neutron Optics

Once the neutrons are produced, they need to be formed into a usable beam. The neutron optic section is an important component of the imaging system. This component has the strongest effect on the fraction of transmitted neutron luminosity, relative acquisition times, and beam divergence (which determines the maximum resolution of the resulting image) [11]. There are three broad classes of neutron optics: geometrical, wave, and crystal optics [12].

The simplest neutron beam forming device is the pinhole aperture, which consists of a small hole in a strong neutron absorbing material like cadmium or gadolinium. It is much like the first optical cameras that used pinhole apertures to form images on a piece of photosensitive paper. A pinhole aperture unfortunately has the side effect of significantly reducing the neutron fluence and thus increases the acquisition time. A larger aperture increases the neutron fluence, but reduces the resolution [6]. Systems that use pinhole apertures for phase contrast imaging typically have a pinhole turret that allows the user to quickly switch between apertures to get the best compromise between acquisition time and resolution [6]. Basic particle beam collimation follows geometric principles. As can be seen from Figure 2, a perfect collimator absorbs all rays that are not travelling within the divergence of the beam axis.

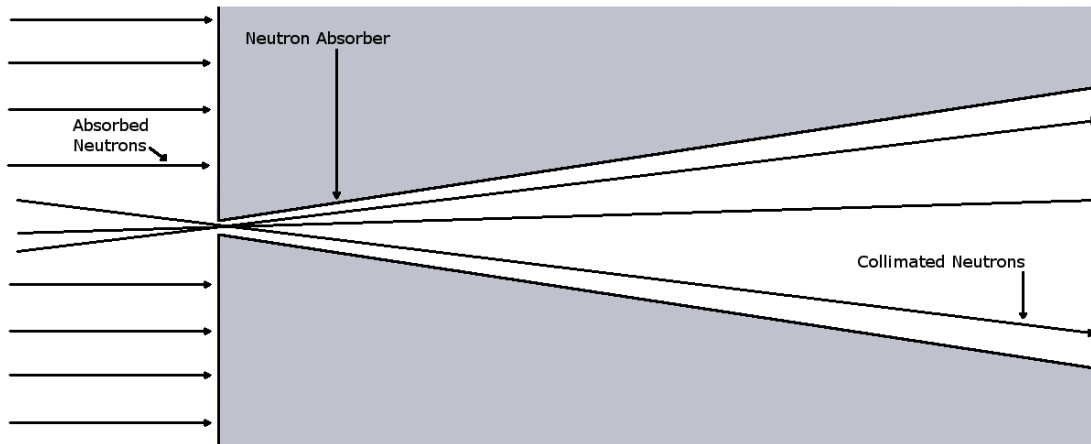


Figure 2. Divergent collimator.

More advanced collimators are commercially available, but are typically more expensive to procure than a simple pinhole-aperture, diverging collimator. These include the Söller slit, straw, and honeycomb collimators. These advanced designs provide for enhanced beam parameters that result in higher beam luminosity and low beam divergence, thus providing sharper images and quicker acquisition times.

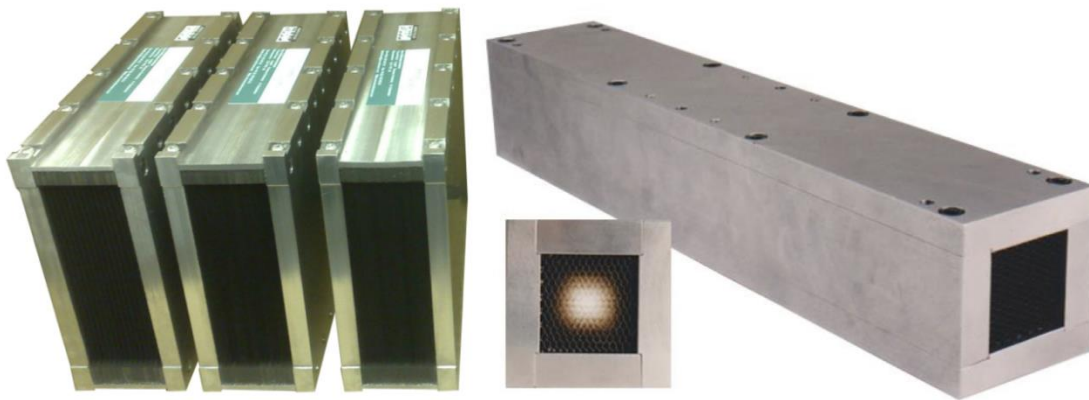


Figure 3. Söller (left) and honeycomb (right) collimators, both manufactured by EuroCollimators Ltd [13].

Neutron attenuation within the collimator is attributed to scattering with air (roughly 5% per meter) and can be reduced by either backfilling the beam tube with helium (1% per meter) or vacuum [14].

Refraction of cold neutrons enables beam-line optics that approach the characteristics of visible light optics in that the neutrons can be reflected off axisymmetric, grazing-incidence mirrors to form converging and diverging neutron beams that form the basis of neutron microscopy [15], [16].

2.3. Neutron Detection

Neutron detection involves some form of registering a neutron interaction. Neutrons are unique among the nuclear particle family due to the fact that they are the only massive, charge-neutral subatomic particle, and they interact with only the nucleus of an atom rather than interacting directly with the atomic electron cloud. Neutrons can be produced in several ways that are relatively simple by today's modern standards. With a theoretical half-life of approximately 1000 seconds, neutrons are not free for long, and their primary interactions consist of scattering and absorption [17]. The primary means of detecting neutrons for imaging purposes is by the detection of photon emission as a product of charged particle emission from a radioisotope created by the captured neutron.

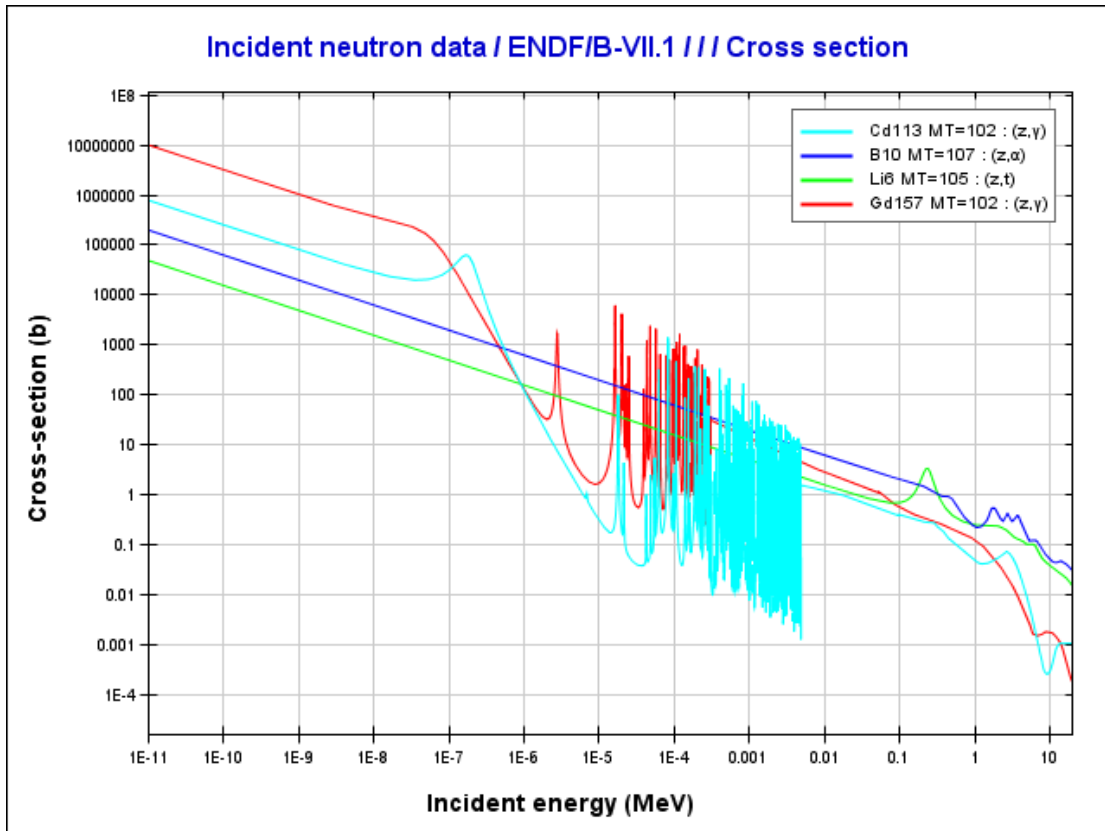


Figure 4. Neutron absorption cross sections for select isotopes [18].

Many competing factors such as cost, cross-section, daughter products, shielding, etc. determine the appropriate neutron absorber for a given application. Many imaging applications require low background gamma production along with a relatively large energy deposition. These requirements make ${}^6\text{Li}$ the isotope of choice. For general neutron shielding applications, boron, in the form of B_4C , is usually the material of choice due to its low cost, ubiquitous use in other industries, and because it is relatively non-toxic.

2.4. Neutron Imaging Methods

Neutron detection was originally performed with single emulsion photographic plates similar to those used in X-ray radiography except that a gadolinium conversion screen converts the neutrons into energetic electrons, which then interact with the photographic emulsion film. State-of-the-art neutron detection techniques utilize digital acquisition methods; thus, they have made great leaps and strides by piggybacking on the digital revolution. The current state-of-the-art neutron image acquisition methods include [19]:

1. Photographic film coupled to a neutron converter screen as described above. This method provides the highest proven resolution; however, it has the disadvantage of having to be processed using antiquated film developing.
2. Electronic camera using a charge coupled device (CCD) or complementary metal-oxide semiconductor (CMOS) sensor that captures reflected light from a neutron sensitive scintillation screen. These systems are limited in resolution due to the scintillation light diffusing through the plate (and the distance of the energetic particles that excite the phosphors). This technique has a hard limit of approximately 10 μm , which is the range of a triton in plastic media. These methods have the advantage of being simple and cost effective.
3. Digital imaging plates for X-rays that have been made neutron sensitive by coating the surface with a neutron absorptive material that emits

detectable radiation. This technique is limited in resolution by the image-forming pixel size, but has the advantage of quick acquisition times.

4. Amorphous silicon flat panel detectors that are currently under development for medical x-ray imaging can also be made sensitive to neutrons. These detectors have the advantages of high resolution and large image area, but are very expensive.
5. Track-etch foil imaging is a technique that uses a foil in close contact with a converter screen which is then etched to enlarge the holes made by charged particles. A digital camera then digitizes these tracks. The main drawback of this method is that it does take a considerable amount of time to process the image, but it has high gamma background discrimination [19].

Through the use of digital acquisition methods (namely the use of CCD cameras and personal computers), it became possible to perform 3D reconstructions in a practical manner, and the advances in computer science have made neutron tomography a state-of-the-art NDT method. The unique interactions of the neutron make it possible to probe an object to form a visible image that allows the inspection of fully assembled internals during operation. 3D models are necessary to explore flow patterns through porous media [19].

2.4.1. Limitations

The two key disadvantages of neutron imaging are the complexity and expense of neutron sources of adequate neutron flux levels, and the low resolution of neutron images relative to current X-ray methods. Neutron imaging is best used in tandem with either gamma or X-ray imaging to obtain a more inclusive picture of the object being interrogated [3]. Low atomic number materials are generally strong neutron scattering materials, and this fact limits the use of neutrons in objects that have a large number of low atomic number nuclei [2].

2.4.2. Recent Advances in Neutron Imaging

Recent advances in neutron imaging (within the past 20 years) have paved the way for digital processing techniques that offer a faster turnaround time [20]. Starting in the mid-1990's, there was renewed interest in neutron imaging that was sparked by advances in computer science (namely computer processors, memory storage and imaging sensors). These advancements in computer science made old ideas such as tomography possible for the first time in its history. It is interesting to note that the advances in computer science were never intentionally designed to improve neutron imaging. Nonetheless, the digital revolution led to the implementation of new digital neutron imaging methods and reduction in the total time from image acquisition to image viewing. Even with these advances, digital neutron imaging (using a 50 μm LiF:ZnS scintillation screen is 72 μm) is only now beginning to approach the resolution limit of analog radiography film resolution (10-30 μm) [14], [19], [21]. 50 μm is the

lower resolution limit of the lithium scintillator layers [21]. The highest resolution images available today are still produced with photographic films [19].

A relatively new neutron imaging method that takes advantage of the energy dependent nature of neutron cross-sections is called monochromatic neutron imaging. This goes beyond the normal 3D attenuation techniques in that images can now be taken that are able to discern between more materials [22].

Phase-contrast imaging uses the slight change in neutron refraction index between boundaries to enhance the boundaries of weakly attenuating materials. Phase contrast imaging takes advantage of a small difference in the neutron refractive index at material boundaries to enhance edges and discontinuities in an object with weakly attenuating material. The effect of a small difference in the index of refraction produces a very small deflection in the path of the neutron beam. The slight deflection in the neutron beam requires the neutron detection screen (NDS) to be placed a large distance (typically 1-2 m) behind the object so that the small angle can be exaggerated on the NDS. The main disadvantages of these setups are the extra required space, reduced neutron flux, and long acquisition time [22].

Related to phase contrast imaging is dark-field imaging; this method uses a pair of absorption gratings to apply interferometry techniques in order to increase resolution to the meso/microscale range [22].

Polarized neutron imaging is able to probe materials using the magnetic spin of the neutron as an interrogation method that is able to extract magnetic data from the

sample. This neutron imaging method requires large magnets to provide the necessary field to polarize the weak magnetic moment of neutrons [22].

2.5. Neutron Imaging Applications

The applications of neutron imaging are far and wide; a full review of these applications is provided. The following is a brief overview of some of the applications of neutron imaging. Neutron imaging is unique in the field of reactor fuel degradation studies in that it allows simultaneous probing of the coolant flow patterns and fuel structure during specially designed experiments [23]. There are many aspects of Biology that can be investigated with neutron imaging, such as moisture distribution in soil and plants, root growth, and the detection of pollutants and poisons to name a few [1]. Phase contrast neutron imaging is able to detect tiny cracks in weakly absorbing samples due to a shift in the neutron wave refractive index. These tiny material imperfections would be almost unobservable without applying the phase contrast technique [24].

Neutron imaging of irradiated nuclear fuel reveals the internal structure and provides comprehensive information about the structure and condition of the irradiated fuel. The differences in attenuation between X-rays and neutrons make these two imaging techniques complementary to one another. The high gamma doses that are encountered with irradiated nuclear fuel make indirect observation techniques the only technique available to evaluate the irradiated nuclear fuel [25].

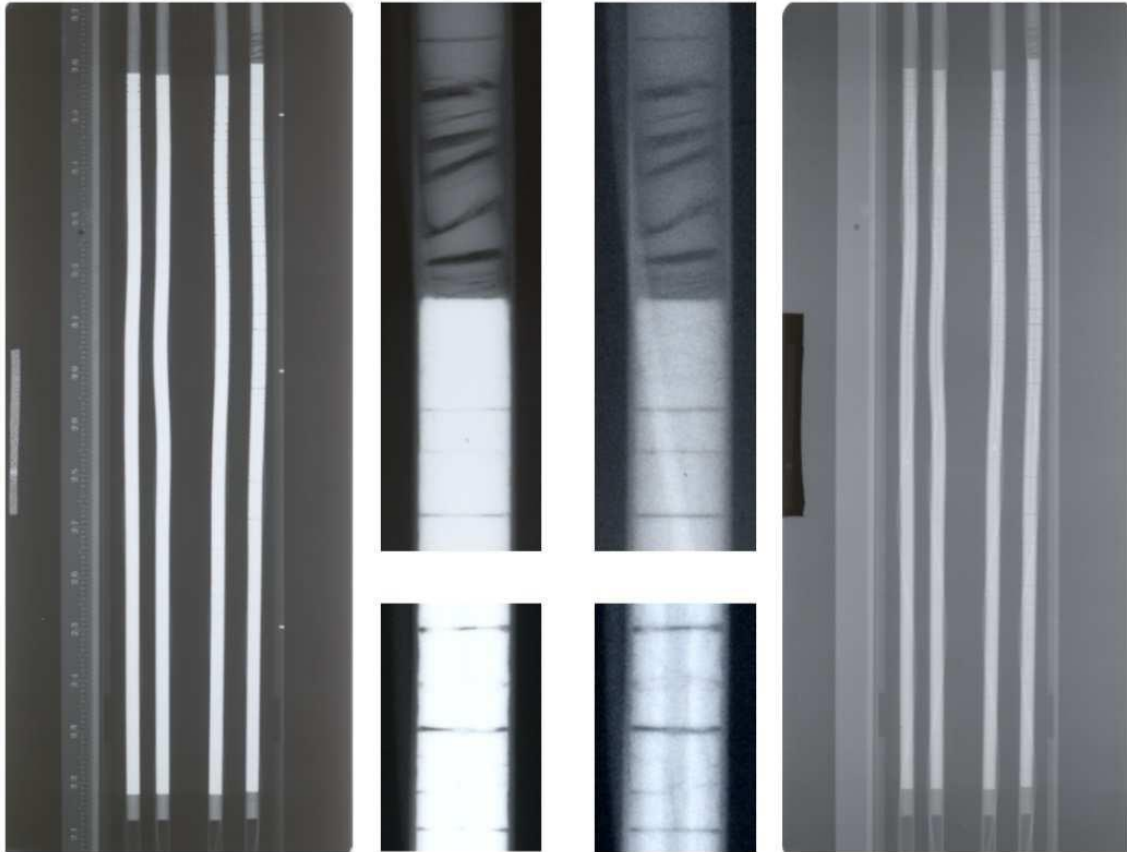


Figure 5. Neutron images of irradiated nuclear fuel produced at the Neutron Radiography reactor (NRAD) using dysprosium (left) and indium (right) conversion foils [25].

Materials science and engineering requires a broad range of imaging techniques. Neutron imaging is well suited for detecting light atoms (for example, Hydrogen, Lithium and Boron) buried among heavy atoms (such as metals), which makes it a unique tool for non-destructive studies for materials science and engineering applications. Examples include investigations of adhesive joints, soldering, metal casting, proton exchange membrane (PEM) fuel cells, texture and stress imaging, two-phase flow through porous media, etc. [22].

Zircaloy-4 is a common nuclear fuel cladding for water cooled reactors, but it is susceptible to hydride formation. Neutron imaging provides yet another unique opportunity to observe and visualize hydrogen content within materials. Hydrogen concentration can be correlated using the transmitted neutron intensity from the images, and the hydrogen content can be determined precisely within a $55\ \mu\text{m} \times 55\ \mu\text{m}$ area of the hydrided tube [26].

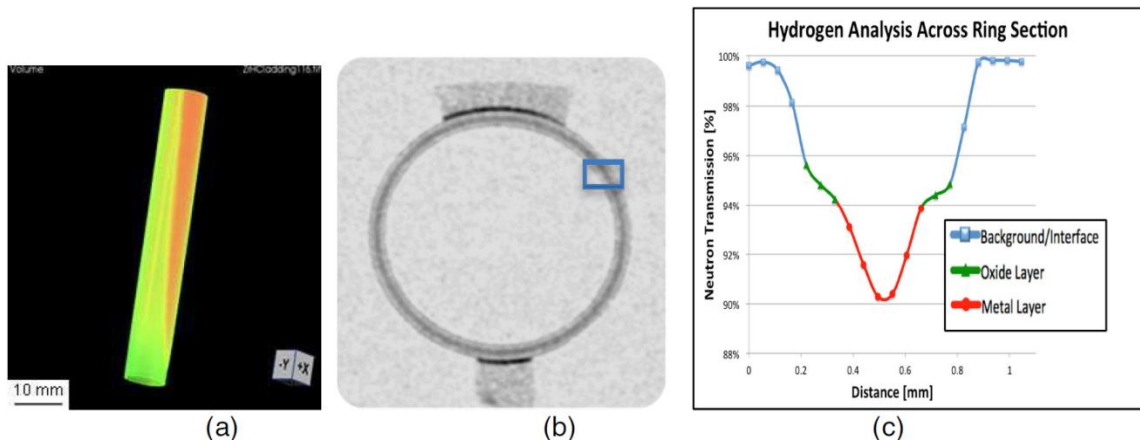


Figure 6. (a) 3D uneven hydrogen (colored in red) distribution in a hydrided Zircaloy-4 cladding sample, (b) top-view neutron image of oxidized Zircaloy-4 ring sample showing high hydrogen concentrations in the middle, (c) plot of the ring sample's neutron intensity vs. hydrogen content [26].

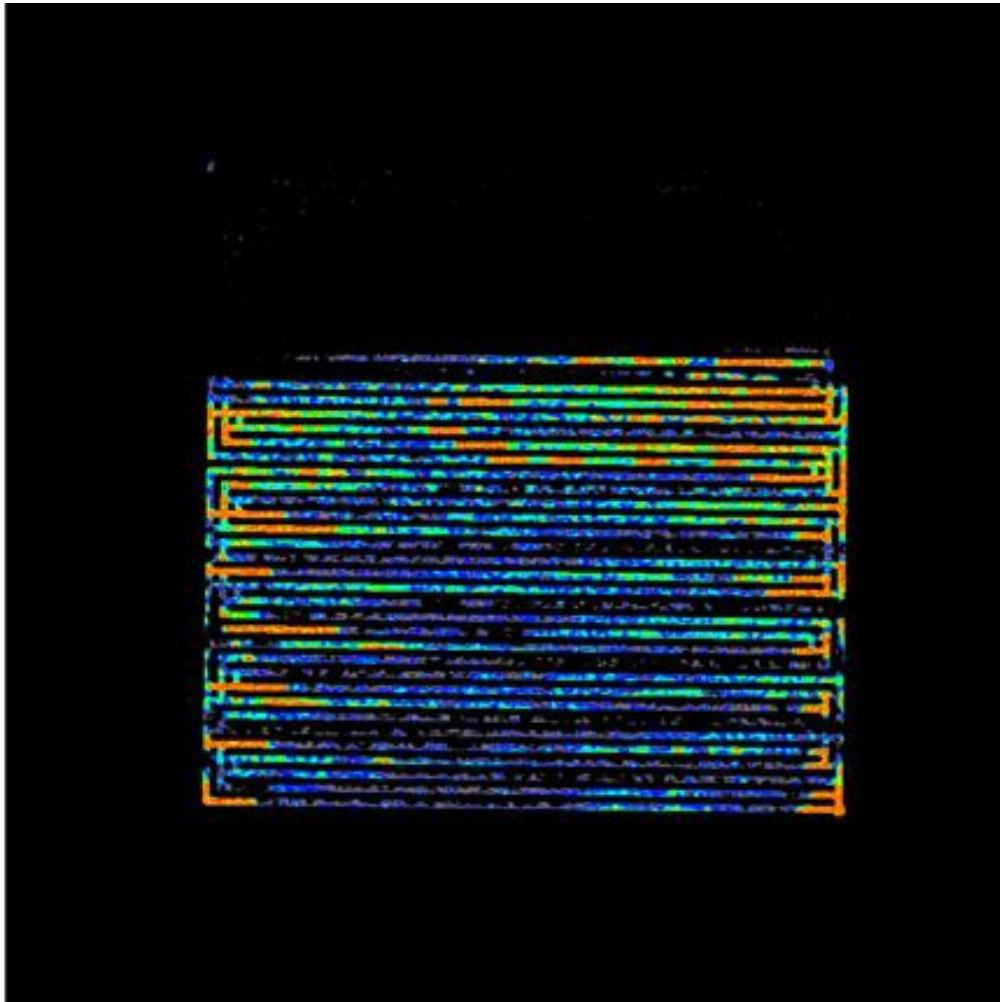


Figure 7. PEM fuel cell flow channel water blockage [27].

In the case of PEM fuel cells, neutron imaging is better suited than X-ray and NMRI methods to interrogate the internal water distribution of an operating fuel cell. Transparent fuel cells have also been constructed for the purpose of visual inspection, but the materials and physics are different. Neutrons are better able to penetrate the metal housing while being extremely sensitive to the presence of water [22]. Figure 7 is a normalized and false color image of an operational fuel cell; the color range is black to orange with high water content represented by the color orange [27].

Heat pipes are important heat transfer devices that have found extensive use in many consumer electronics such as central processing units (CPUs), high power light emitting diodes (LEDs), and space nuclear reactor designs, [28]. Heat pipe visualization is complex due to the subtle interaction of fluid surface tension with various materials. These interactions are specific to the fluid, material, and surface finish [17]. Figure 8 is a time series of images of a heat pipe under different applied thermal powers. 50 V, 100 V, 150 V, and 200 V, correspond to 9 W, 40 W, 96 W, and 162 W, respectively [28].

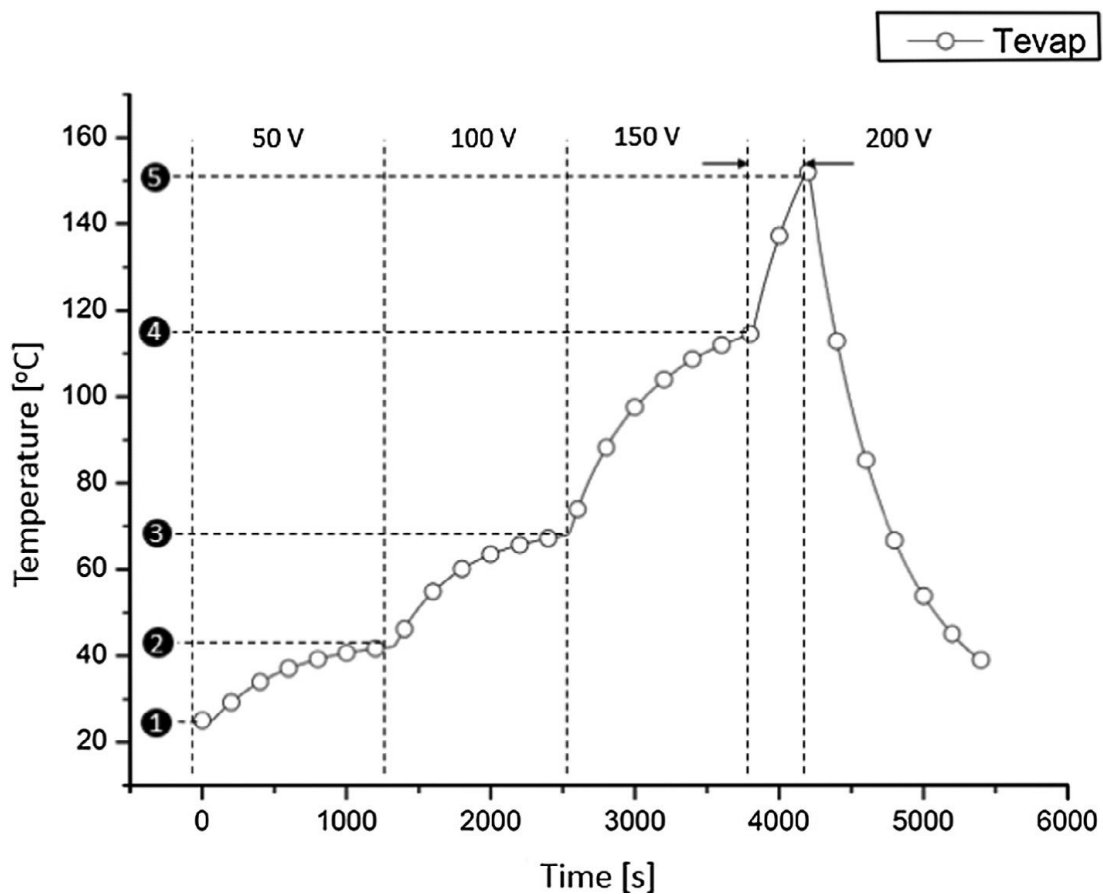
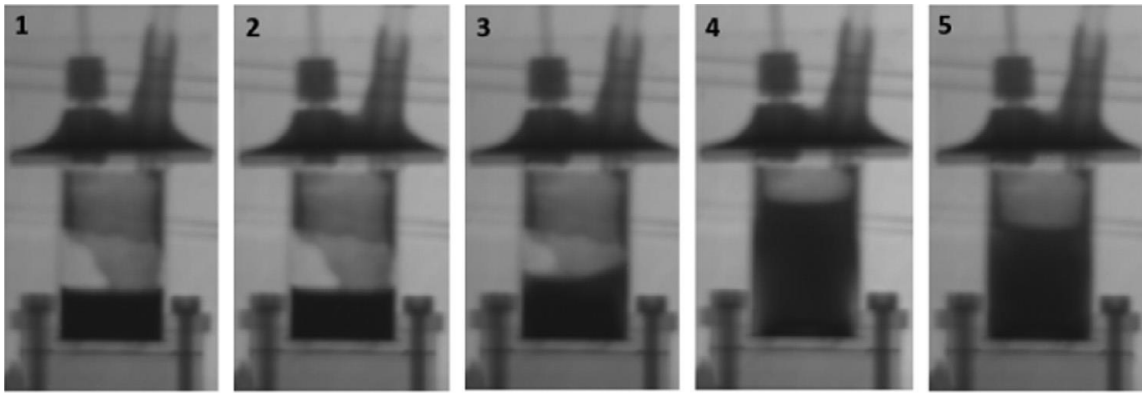


Figure 8. Series of neutron images depicting the startup and operation of a heat pipe over several power ranges [28].

Time-resolved neutron imaging was used to observe the temporal evolution of different types of polypropylene foams in Figure 9. Neutron imaging was able to provide

benefits over X-ray imaging because of the ability to visualize the internal structure of polymeric foams inside metallic molds during foam production.

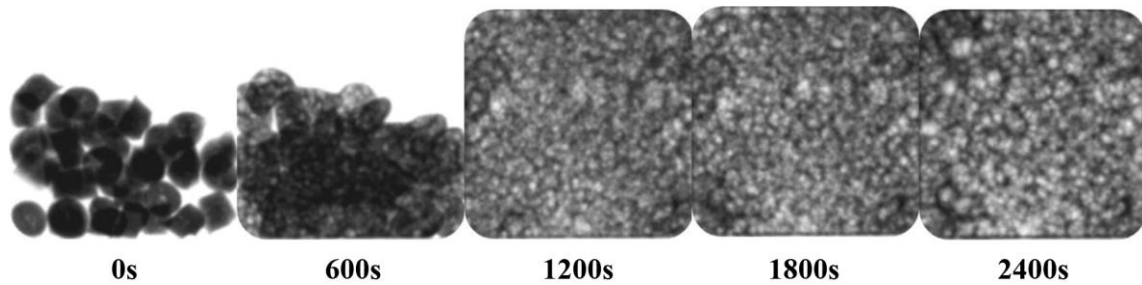


Figure 9. Neutron imaging sequence during foam expansion and ageing [29].

Neutron imaging is a unique diagnostic tool for investigating hydrogen storage media under charging and discharging conditions. The *in situ* hydrogen concentration can be characterized in real-time in a practical hydrogen storage system. Figure 10 shows a prototypical, $\text{LaNi}_{4.78}\text{Sn}_{0.22}$ -based hydrogen storage bed during and after several desorption and absorption cycles. The use of D_2 in these experimental runs allowed the imaging of thicker hydrogen storage beds [30]; D_2 has a lower neutron scattering cross section [18].

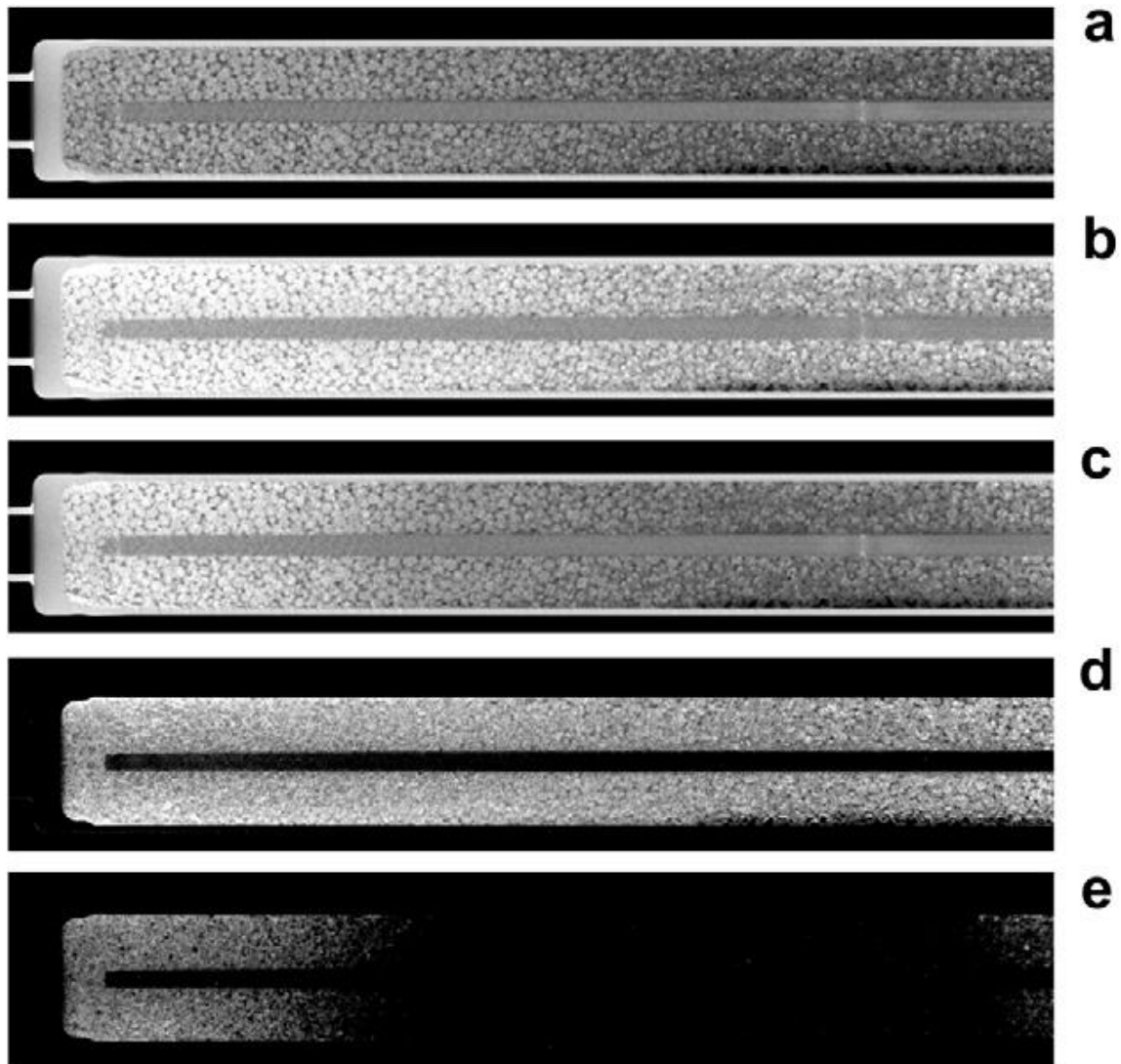


Figure 10. Sagittal slices through the tomographic reconstructions. (a) The total attenuation coefficients of (a) the empty bed, (b) the bed filled with 94.5 L of D_2 , and (c) the bed after desorbing approximately 60 L of D_2 . Black and white correspond to attenuation coefficients of 0 cm^{-1} and 1.0 cm^{-1} , respectively. Subtracting the empty bed attenuation coefficient yields the D content of the bed: (d) after the absorption of approximately 100 L and (e) after desorption of approximately 60 L of D_2 [30].

Diesel engines are experiencing significant growth in the passenger vehicle market due to their 20-30% energy efficiency advantage over gasoline direct injection

engines. Newer engines increasingly rely on advanced injection systems to enable low-emission, high-efficiency combustion. Understanding the mechanisms behind fuel sprays and combustion inside the engine, as well as the mechanisms for soot loading and oxidation within after-treatment devices, is critical to predicting the system behavior and the optimal strategies for maximum energy efficiency of the combined engine and after-treatment system [31]. Figure 11 shows three images that were produced as a result of diesel combustion research at ORNL.

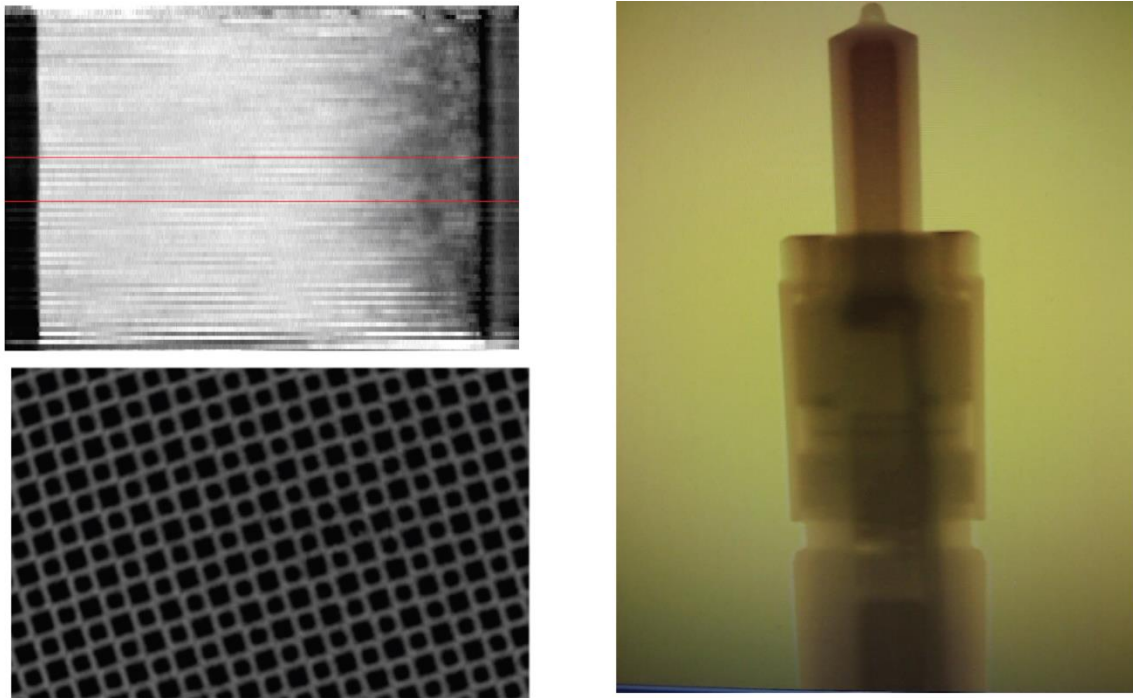


Figure 11. X-ray image of a diesel particulate filter (top left) [32], neutron tomograph (bottom left) with a 40 μm resolution [33], and a diesel injector (right) taken at ORNL in April 2012 with 75 μm resolution.

Spray imaging research is of great importance in understanding the dynamics associated with spray-jet atomization, evaporation, and combustion. Currently, there is a

solid understanding of the far-field spray physics; however, the region termed “the lift-off length” is poorly understood. This region is critical because the conditions necessary for fuel mixing and combustion are formed here [34]. The lift-off length has a high optical density that precludes the observation of this area of the spray field with optical techniques, and the limited interaction cross-section of X-rays contributes to the low SNR of computed tomography (CT) scans for hydrocarbon distribution imaging [35]. In an attempt to overcome this physical limitation, cerium was added to the fuel, but the absorption was still too weak [36]. Thus, neutron imaging is the only adequate imaging technique available for probing this interesting phenomenon.

Diesel particulate filters (DPFs) mechanically filter soot out of the exhaust stream of a diesel engine, thus reducing problematic soot pollution from these engines. Managing soot build-up in these DPFs is a major challenge, and the continuous collection of soot in these filters increases backpressure and, in turn, decreases engine efficiency. In order to maintain acceptable performance, the filter must be regenerated via oxidation of the trapped soot. Acquiring a greater understanding of soot loading and oxidation is crucial to the long term performance of these DPFs. X-ray imaging, once again, produces fuzzy images of the soot-bearing DPFs (due to interference of the cordierite material used for the filter construction). Figure 11 demonstrates the inherent higher resolution neutron tomography of DPFs vs. the X-ray CT imaging [33]. The proposed high resolution instrument proposed herein will allow further investigation of this area of research.

Neutron radiography has been used in the quantitative assessment of hydrogen in Zircaloy and metal hydrides. This is a problem in nuclear energy generation associated with water-cooled nuclear reactors in which a chemical reaction occurs between the zirconium and water to produce zirconium hydride. Quantitative measurements of hydrogen have been made to determine absorbed hydrogen in getters and neutron radiography offers the detection of hydrogen in zircaloy to a sensitivity of 3 parts per million per cm [6]. These are just a few of the many applications of neutron imaging.

3. RECONSTRUCTION ALGORITHM AND IMAGE PROCESSING

Digital image processing has become commonplace due to the widespread access to digital cameras and personal computers. The process of taking an image is one that necessarily degrades a real, continuous image, and digitizes the image into an array of numbers that represent the image. The digitized image has inherent error associated with the truncation of the continuous image into discrete values otherwise known as pixels. The image sampling process has a great deal of importance to the resulting digital copy of some scene; what, if the sampling parameters are known, one can infer a larger image data set than that is directly recorded into the digital image. This information can be considered intertwined within multiple pixels and can therefore be teased out of the data with suitable algorithms that take into account the image formation process [37].

3.1. Image Sampling

Some knowledge of the image acquisition process is necessary to determine the response of the imaging system. In theory, a scene is an infinite, continuous field from which the imaging system produces tallies of various parameters to form a finite image [1]. In situations that involve a substantial noise component in the image, it is beneficial to consider the process as a two-dimensional random process depicted in Figure 12.

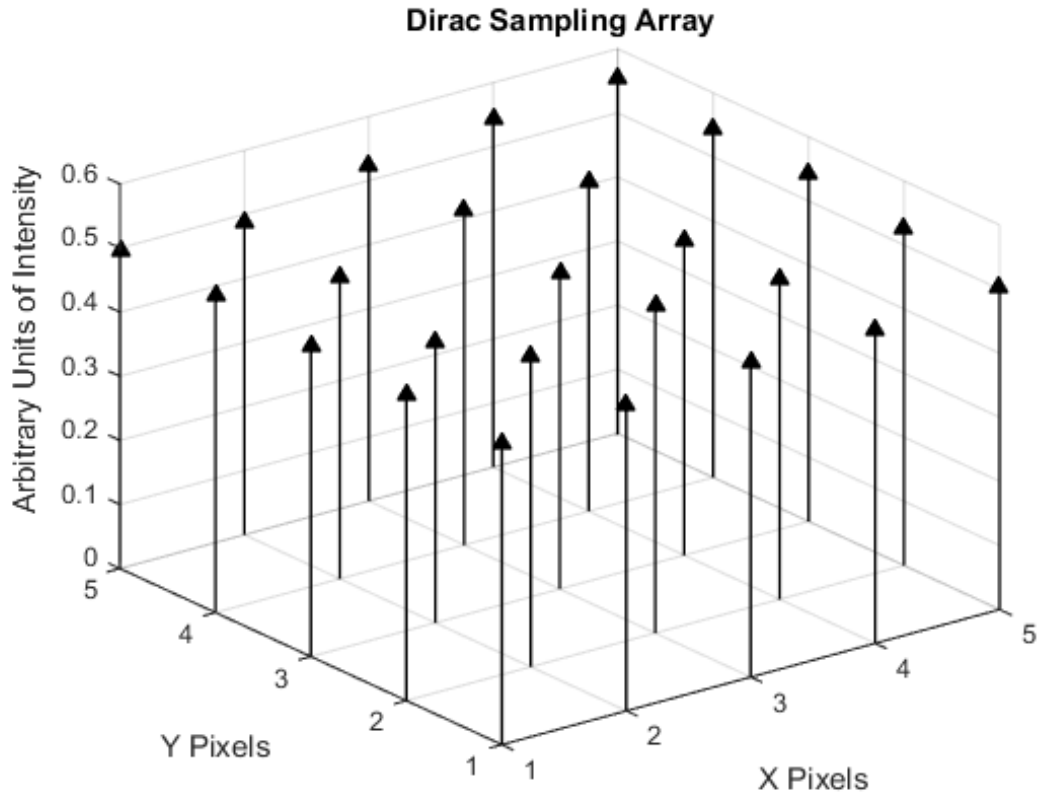


Figure 12. Dirac delta function sampling array.

Consider the deterministic example of the infinite domain image sampling process using a continuous, ideal image field that represents some quantity (i.e. luminance). The sampled image, $f_p(x,y)$, is then obtained by the inner product of the image field $f_1(x,y)$, and the spatial sampling function, $S(x,y)$, given by Eq. (4). The sampling function effectively extracts information from the data field to produce an image.

$$S(x,y) = \sum_{j=-\infty}^{\infty} \sum_{k=-\infty}^{\infty} \delta(x - j\Delta x, y - k\Delta y) \quad (4)$$

$$f_p(x, y) = f_I(x, y)S(x, y) = \sum_{j=-\infty}^{\infty} \sum_{k=-\infty}^{\infty} f_I(j\Delta x, k\Delta y)\delta(x - j\Delta x, y - k\Delta y) \quad (5)$$

Equations (4) and (5) will be used later for the discussion of reconstruction by convolution of another function that represents the degradation of the image by the sampling process. The ideal representation is useful in elucidating the process of image sampling, but in practice, the process is far from ideal. In reality, we must take into account noise, which, depending on the source, is typically random. Hence, a representation of random noise is incorporated in the image. The presence of noise has the effect of degrading the signal, as illustrated in Figure 13.

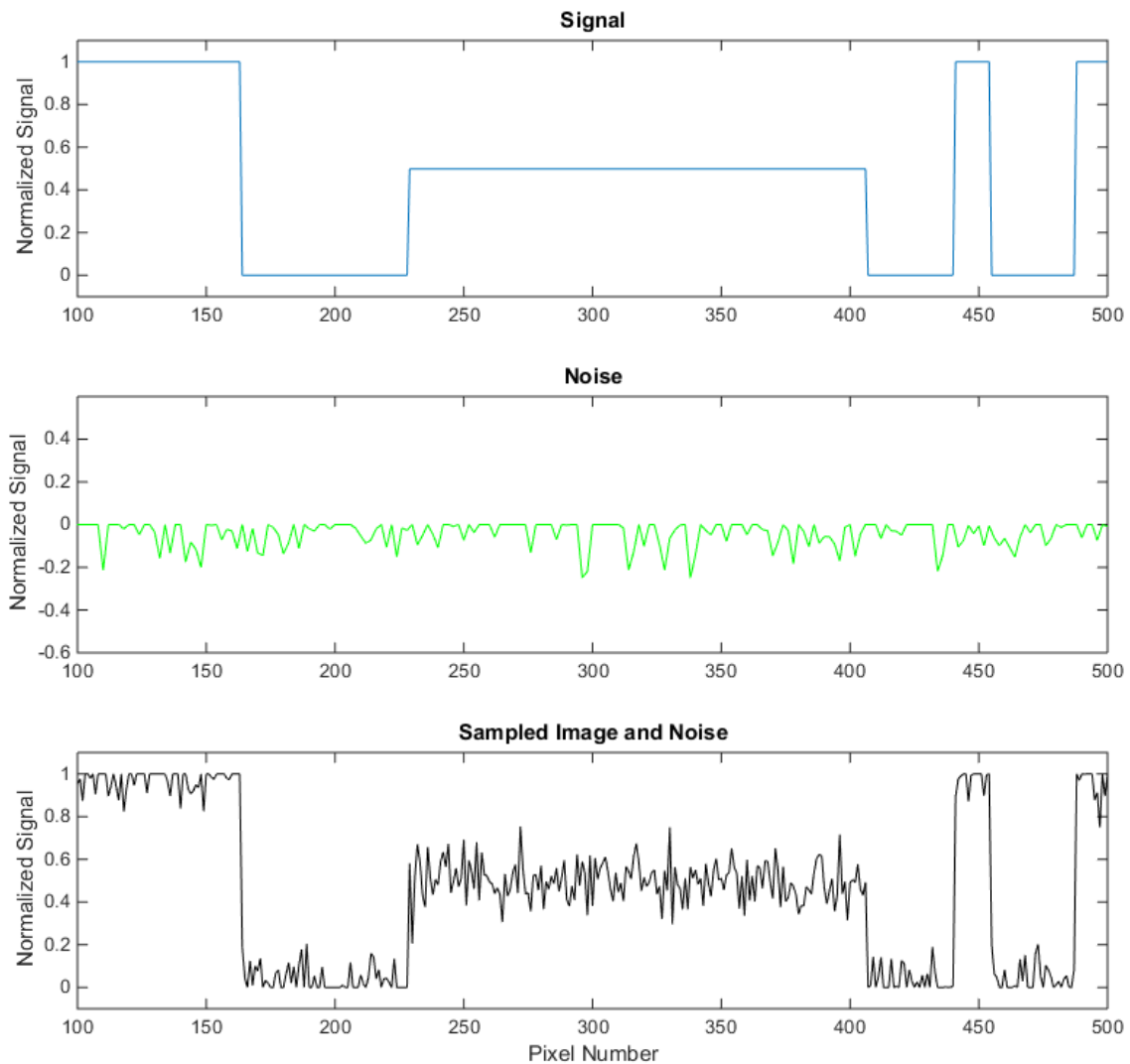


Figure 13. Signal and noise impacts on measurements.

It follows that the spectrum of noise may be wider than the image spectrum and the tails of the noise overlap onto the passband of the filter, resulting in additional noise artifacts in the reconstructed image. The common solution to this problem is to use one or more of the many noise filtering algorithms that are designed to reduce the effects of specific types of noise. Filtering options are discussed in the ensuing sections.

3.2. Digital Image Filters

Digital image processing uses algorithms that operate on digital images. With the advent of digital cameras and the advancement of personal computers, image-processing techniques have made leaps and bounds in capability. Digital image processing is important for improving the quality of information contained in the image and extracting useful information and features such as edges, color variation, and filtering noise. Digital image processing is able to utilize complex computer algorithms, offering higher performance in the implementation of these algorithms that would be impossible to accomplish via analog routes [38]. Digital filters are used to preprocess image data to remove unwanted artifacts and noise from the image data. These filters range in complexity and the type of image artifacts they filter out. Various noise-filtering techniques are available from pre-existing kernels that are compiled into code packages, one of which is MatLab Image Processing Toolbox [38]. These filters are used to remove artifacts from the image that occur due to the high radiation background of the radiography hall [19]. Filters can be broadly classified into two types: linear and non-linear.

3.2.1. *Edge Detection and Enhancement*

Edge detection and enhancement is a technique that is used to enhance the contrast of boundaries between objects in an image. This technique edge detection technique can then be used to determine features in an image that can be applied to image registration. The success or failure of edge detection depends on the definition of

the goals for edge point computation. In addition, the goals must be sufficiently precise to delimit the behavior, yet general enough so that assumptions about the edges can be kept to a minimum. A simple, yet robust edge detection and enhancement technique is performed using the Laplacian operator. On the continuum, the Laplacian of an image field, l , is the same as any other Laplacian as given in Equation (6).

$$l(x, y) = \nabla^2 f(x, y) \quad (6)$$

The Laplacian is then scaled by some constant, c , and added to the original image as indicated by Equation (7).

$$f_{enhanced}(x, y) = f(x, y) + c * l(x, y) \quad (7)$$

The main side effect of this algorithm is that it enhances the noise in addition to the image edges. The Laplacian used for image filtration is often approximated by a 3 by 3 matrix, as shown below.

$$\begin{matrix} 1 & 1 & 1 \\ 1 & -8 & 1 \\ 1 & 1 & 1 \end{matrix}$$

An improvement to the Laplacian filter is the Laplacian-of-a-Gaussian (LoG) filter, which is less sensitive to noise [39]. The two-dimensional Gaussian, G , is represented by Equation (8).

$$G(x, y) = \frac{1}{2\pi\sigma^2} e^{-\frac{(x^2+y^2)}{2\sigma^2}} \quad (8)$$

A more compact form for this demonstration is available by performing a change of variables where $r^2 = x^2 + y^2$. The Laplacian of a Gaussian (LoG) is then given in Equation (9). The filter kernel is shown in Figure 14 for a 9 by 9 pixel area, but more points have been included in the calculation for clarity.

$$LoG(r) = \frac{1}{\pi\sigma^4} \left(1 - \frac{r^2}{2\sigma^2}\right) e^{-\frac{r^2}{2\sigma^2}} \quad (9)$$

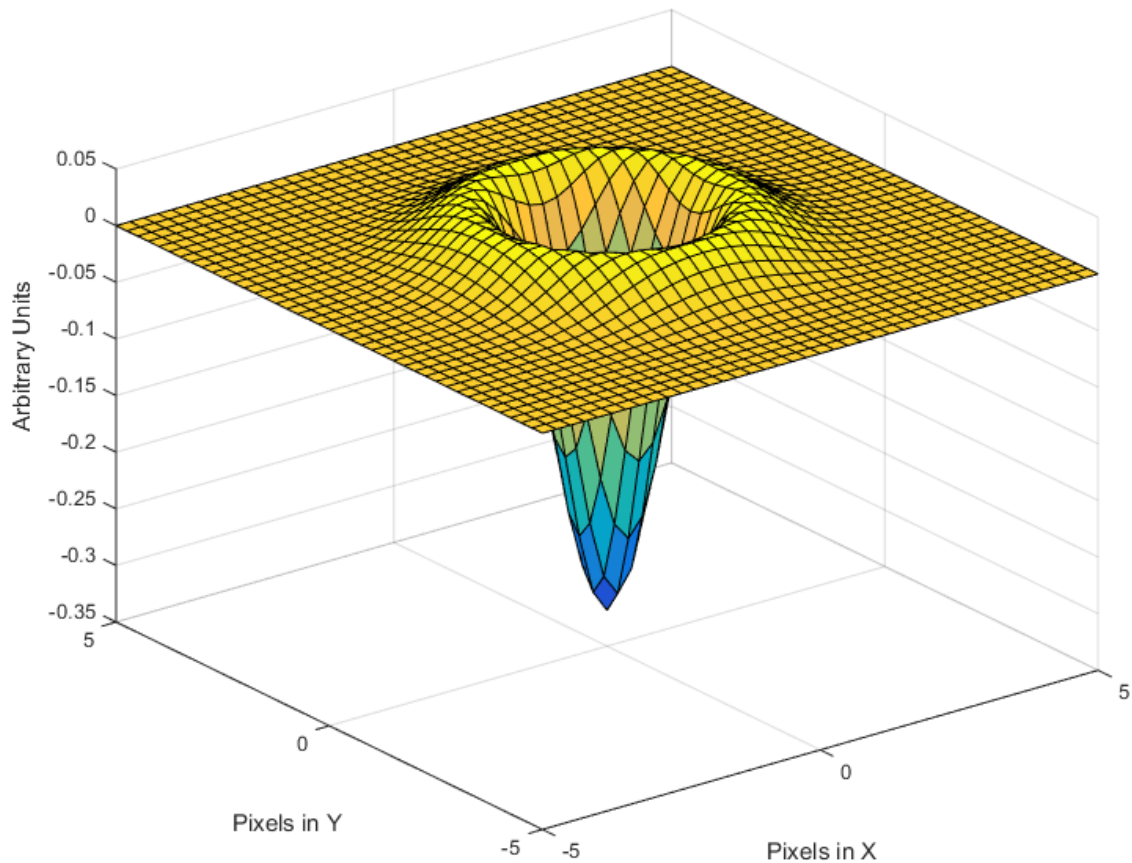


Figure 14. LoG filter with a standard deviation of 1

3.2.2. *Gamma Radiation-Induced Noise Filtration*

Gamma rays scatter off charged particles causing the charged particle to recoil, and if the charged particle is an electron, then the process is called Thompson scattering. The tracks that Thompson scattered electrons make through a CCD have a very distinct structure, such that it is possible to detect these features within an image and selectively remove the artifacts to reduce image noise [40]. Unfortunately, the noise clusters are different when comparing different camera sensors. Each camera must be individually characterized to determine the best settings for this cluster-noise filtering scheme [41].

Edge detection techniques are used to find closed regions with large variations in the absolute intensity, and the first and second spatial derivatives. A filter (median, mean, minimum, etc.) is chosen to operate over those isolated areas to remove the background radiation artifacts from the image while preserving the fine detail in the rest of the image [41]. This method works best in darker areas of an image because the lower signal-to-noise-ratio (SNR) makes the background noise stand out. The filter used in this research is an adaptive form of the Wiener filter designed for images and included in the Image Processing Toolbox™ in MatLab.

$$\mu = \frac{1}{XY} \sum_{x,y \in XY} f(x,y) \quad (10)$$

$$\sigma^2 = \frac{1}{XY} \sum_{x,y \in XY} f^2(x,y) - \mu^2 \quad (11)$$

$$f_{filtered}(x,y) = \mu + \frac{\sigma^2 + v^2}{\sigma^2} (f(x,y) - \mu) \quad (12)$$

The filter estimates the local mean and variance in the neighborhood, XY , of each pixel. The filter uses the values estimated in the X by Y neighborhood to calculate a pixel-wise Wiener filter given by Equation (12) [42].

3.2.3. *Optical Transfer Function*

Performance of digital imaging detectors can be described using a number of different parameters. Sharpness and noise are the two major characteristics that describe the intrinsic image quality of the detector [43]. The optical transfer function (OTF) describes the mapping of a known object to the response of the imaging system. This information can be used during the reconstruction process to alter the intensity gradients of the image. Several quantities are related to the OTF: the point-spread function (PSF), the line-spread function (LSF), and the modulation transfer function (MTF). The MTF is defined as the ratio of the output modulation to the input modulation. The MTF is mathematically the absolute value of the OTF taken with the phase shift and expressed as a function of frequency [44].

3.2.4. *PSF*

The point-spread function is the response of a detector to a delta-function input like that of Section 2.1, and approximates the transfer characteristics of an infinitely-thin pinhole camera. It describes the light diffusion across the sensor from a single point and is rotationally symmetric if the imaging system is isotropic [43] [44]. This simplifies the transfer characteristics. With predetermined knowledge of the PSF, the imaging system can correct for the expected deterioration of the acquired image by convoluting the image with the PSF kernel [44]. However, rotational symmetry is hardly ever the case. Specifically within the context of anisotropic reconstruction, the PSF is not applicable due to the broken symmetry. The practical measurement of the PSF is quite difficult due

to alignment issues of the source with the optical axis, the size of the pinhole that must be small compared to the PSF, and the limited flux from the pinhole aperture [44].

3.2.5. *LSF*

The anisotropic resolution of the neutron imaging system discussed in this dissertation is more suited to the analysis of the LSF. It represents a unit line source's radiation intensity distribution on the image plane. The ideal distribution would resemble a line delta function of unit height on the image recorder, but practical systems smear this line into a diffuse, linear mound. The LSF provides a measure of blur and a suitable radiation pattern can be produced from an absorber knife-edge [44]. Measuring the LSF is akin to scanning the PSF across the imaging detector and only yields information in the direction of the scan. The experimental system is purposely designed to be anisotropic. This requires the measurement of the LSF in many directions across the image sensor to get orientation specific information.

3.2.6. *MTF*

The MTF is a measure of an imaging system's ability to reproduce image contrast at various spatial frequencies. Figure 15 graphically demonstrates the principle of the MTF as it relates to changing the spectral input data during the transfer process [43].

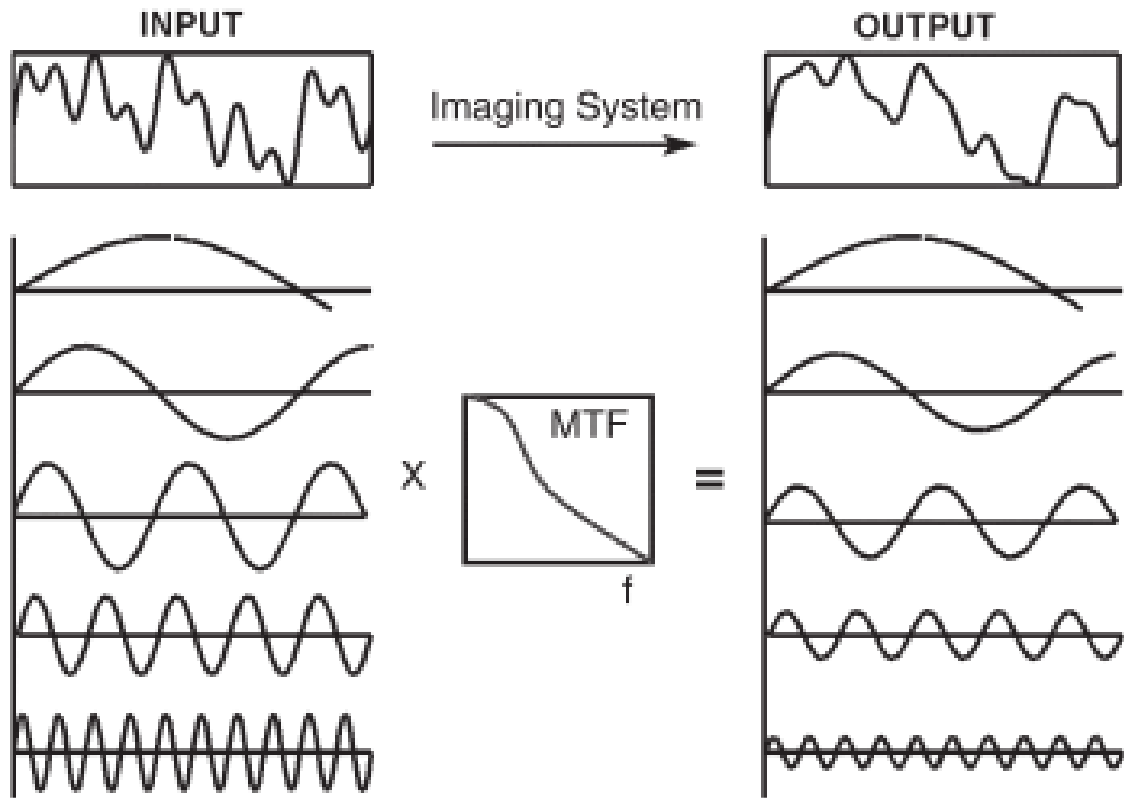


Figure 15. One-dimensional representation of the MTF illustrating the ability of an imaging system to reproduce the input according to the spatial frequency spectrum [43].

The MTF is a function of the ratio of the output-to-input modulations according to the spectral content. It is advantageous to use the MTF to describe the spectral character of the imaging system, and the expected sharpness. Two advantages of this approach are that sharpness can be characterized over many levels of detail, and, under proper conditions, the MTF of the whole system is the product of the individual components. This is represented by Eq. (13).

$$MTF_{Sys} = MTF_{Col} \times MTF_{Scin} \times MTF_{Lens} \times MTF_{CCD}, \quad (13)$$

MTF_{Sys} is the MTF for the system, MTF_{Col} is the MTF for the collimator, MTF_{Scin} is the MTF for the scintillator screen, MTF_{Lens} is the MTF of the camera lens, and MTF_{CCD} is the MTF for the camera CCD. From a mathematical standpoint, the MTF is the amplitude of the Fourier transform of the PSF. Once the LSF has been measured, it is a relatively straight-forward process to calculate the PSF by the method outlined in [45]. The MTF can then be calculated by Fourier transformation from the PSF. Using the aforementioned techniques is advantageous for the neutron imaging system because it provides an objective measurement of the optical system performance and determination of the degradation of image detail [44].

3.2.7. *Image Registration and Alignment*

Image registration is a fundamentally required operation for combining two or more images. This process involves choosing a proper form of registration, choosing a sufficient feature or set of features to track, and calculating the scale, rotation, and displacement relative to a reference image [46]. Image registration is required for the proper positioning of successive images in super resolution reconstruction. In general, Fourier transform (frequency domain) methods of image registration are computationally light when compared to spatial feature-based methods. Regardless of the method used, a majority of the image registration methods follow four basic steps with some small variations:

1. Feature Detection

2. Feature Matching
3. Transform Model Estimation
4. Image Resampling and Transformation

Each step in the registration process has implementation problems that are typical for the respective step considering that the errors compound as the process proceeds. The feature detection step involves deciding what features are appropriate for tracking. These features must be distinctive, spread out over the image, and easily detectable [46]. During the feature matching step, the feature sets must have enough common elements from the reference image and the successive images so that overcoming occlusions and other unexpected changes such as beam luminosity changes that result from power level changes in the neutron source, do not interfere excessively with the registration process. Feature matching problems arise from incorrect feature detection or by degradation of successive images. The mapping functions are chosen according to the *a priori* knowledge of the acquisition process. The resampling step maps the transformed image onto a compatible grid with the reference image. There is always a trade-off between the accuracy of the interpolation and the computational efficiency of the algorithm [46]. Due to the relatively simple nature of the image acquisition process in this dissertation, a simple fast Fourier transform (FFT) based method was chosen as the image registration technique.

3.3. FFT

In [47], the authors outline a method to use FFTs to provide translation, rotation, and scale-invariant image registration. Fortunately, the current environment for the experimental setup negates the requirement for scale-invariance, simplifying the implementation. The method for translated and rotated image registration will be outlined here for the sake of completeness. The technique is based on the translation property of the Fourier transform, which is called the Fourier Shift Theorem. It starts with two images f_1 and f_2 that differ by a displacement (x_0, y_0) . Thus,

$$f_2(x, y) = f_1(x - x_0, y - y_0), \quad (14)$$

with the corresponding Fourier transforms F_1 and F_2 related by

$$F_2(\xi, \eta) = e^{-j2\pi(\xi x_0 + \eta y_0)} * F_1(\xi, \eta), \quad (15)$$

where ξ and η are the transformed x and y variables. The cross-power spectrum of the two images is defined as

$$\frac{F_2(\xi, \eta)F_1^*(\xi, \eta)}{|F_2(\xi, \eta)F_1(\xi, \eta)|} = e^{j2\pi(\xi x_0 + \eta y_0)}, \quad (16)$$

where F_1^* is the complex conjugate of F_1 . The shift theorem guarantees the phase of the cross-power spectrum is equivalent to the phase difference between the two images. Taking the inverse Fourier transform of the cross-power spectrum will yield an impulse function that is approximately zero everywhere except at the displacement required to register the two images. Therefore, if $f_2(x, y)$ is a rotated and translated sample of $f_1(x, y)$, rotated by θ_0 and translated (x_0, y_0) , then

$$f_2(x, y) = f_1(x \cos \theta_0 + y \sin \theta_0 - x_0, -x \sin \theta_0 + y \cos \theta_0 - y_0). \quad (17)$$

Applying the Fourier translation and rotation properties, the transforms of f_1 and f_2 are correlated by

$$F_2(\xi, \eta) = e^{-j2\pi(\xi x_0 + \eta y_0)} * F_1(\xi \cos \theta_0 + \eta \sin \theta_0, -\xi \sin \theta_0 + \eta \cos \theta_0), \quad (18)$$

where ξ and η are the transformed variables. If M_1 and M_2 are the magnitudes of F_1 and F_2 , then

$$M_2(\xi, \eta) = M_1(\xi \cos \theta_0 + \eta \sin \theta_0, -\xi \sin \theta_0 + \eta \cos \theta_0). \quad (19)$$

Again, the physical constraints of the experimental system should negate the necessity of rotation tracking within the image sequence, but it is important to mention it here because some features of the open beam rotate and should be tracked for proper

background subtraction. The main advantage of the FFT-based method is that the computed matching parameters require a fixed amount of time for a fixed image size regardless of how much translation or rotation has occurred [47]. Thus, the FFT-based image registration and matching technique is insensitive to noise and matching should be exact. The use of the phase correlation technique ensures the invariance in translation and rotation [47].

3.4. Discrete Wavelet Transform (DWT)

The DWT is a method of signal decomposition that retains temporal (or spatial) information that is otherwise removed during a FFT. The DWT has its origins in the Window Fourier Transform (WFT). In the WFT the Fourier Transform is applied over a relatively small interval of time or space and is normally defined in integral form, as shown in Eq. (20).

$$W_{\phi}f(\omega, t) = \int_{-\infty}^{\infty} f(\tau)\overline{\phi(\tau - t)}e^{-i\omega t} d\tau \quad (20)$$

$\phi(\tau - t)$ is the rectangular window in the vicinity of t , and $f(\tau)$ is the signal that is being analyzed. DWT uses a wavelet (one of many) that, depending on the wavelet chosen, has characteristics that will act on the signal to extract frequency or spatial information [48]. The form of a translated and scaled wavelet in a two parameter function is given by Eq. (21).

$$\psi_{a,b}(t) = \frac{1}{\sqrt{a}} \psi\left(\frac{t-b}{a}\right) \quad (21)$$

The scaling parameter is a , and the translation parameter is b , and the shape of the wavelet remains invariant under translation and scaling. Thus, the continuous wavelet transform (CWT) is defined by Equation (22).

$$CWT_{\psi}x(a, b) = \int_{-\infty}^{\infty} x(t) \overline{\psi_{a,b}(a, b)} dt = \frac{1}{\sqrt{a}} \int_{-\infty}^{\infty} x(t) \overline{\psi\left(\frac{t-b}{a}\right)} dt \quad (22)$$

It is immediately evident that the CWT and WFT are related and interchangeable.

$$\phi(t-b)e^{-i\omega t} \leftrightarrow \psi_{a,b}(t) \quad (23)$$

The difference between CWT and WFT lies in the fact that the basis function $\phi(\tau-t)e^{-i\omega t}$ is the single frequency sinusoid convolved with the window function $\phi(t)$, in which the window width is fixed by the choice of ϕ and independent of ω and b . This is in contrast to the fact that the window widths for $\psi_{a,b}(t)$ depend on scale and the window area in the $t-\omega$ plane is constant. For a large value of a (low frequency) the time window is large and the spectral width is small; thus, by varying the scale parameter, fine detail can be separated from the coarse background. In addition, the

original signal can be completely recovered through integration of the CWT and its transform using Eq. (24).

$$x(t) = \frac{1}{C_\psi} \int_{-\infty}^{\infty} \int_{-\infty}^{\infty} CWT_\psi(x)(a, b) \psi_{a,b}(t) \frac{dbda}{a^2} \quad (24)$$

The constant, C_ψ , is finite and defined by Eq. (25).

$$C_\psi = \int_{-\infty}^{\infty} \frac{|\hat{\psi}(\omega)|^2}{|\omega|} d\omega \quad (25)$$

The DWT is able to calculate the CWT at discrete sets of scales for a discrete signal. It follows that multiresolution analysis can be investigated to further understand wavelet transforms. In short, signals have varying degrees of detail at different scales - much like viewing a scene through a telephoto lens. It is important to note that there are potential decomposition scales that follow a different scaling pattern. In this derivation, we follow a geometric series of scales that reduce the resolution by half with each iteration of the algorithm. For a different signal, it may make more sense to follow a logarithmic scaling pattern. The choice of scaling parameter is important; if we choose $a = 2^{-j}, j \in \mathbb{Z}$, the algorithm is equivalent to decomposing the signal into successive octaves [48]. Therefore, the approximation subspaces form a nested sequence of subspaces with each successive subspace representing a lower octave.

$$\{0\} \leftarrow \dots \subset V_{-2} \subset V_{-1} \subset V_0 \subset V_1 \subset V_2 \subset \dots \rightarrow L^2 \quad (26)$$

It follows that the subspaces, V_n , are formed from higher subspaces and mutually orthogonal wavelet subspaces. The orthogonal sum is denoted by the symbol \oplus .

$$V_n = \bigoplus_{j=-\infty}^{n-1} W_j \quad (27)$$

$$V_{n+1} = \bigoplus_{j=-\infty}^n W_j = \bigoplus_{j=-\infty}^{n-1} W_j \oplus W_n = V_n \oplus W_n \quad (28)$$

From Eq. (27) and (28), we observe that the subspaces $\{V_j\}$ are nested and $\{W_j\}$ are mutually orthogonal. The bases of subspaces $\{W_n\}$ are outcomes of operations from the wavelet function $\psi(t)$, in a similar manner as $\{V_n\}$ are generated by $\phi(t)$. Therefore, any function $f_j(t) \in V_j$, and another function $g_j(t) \in W_j$, are written as Equations (29) and (30), respectively.

$$f_j(t) = \sum_{k=-\infty}^{\infty} c_{j,k} \phi(2^j t - k) = \sum_{k=-\infty}^{\infty} c_{j,k} \phi_{j,k} \quad (29)$$

$$g_j(t) = \sum_{k=-\infty}^{\infty} d_{j,k} \psi(2^j t - k) = \sum_{k=-\infty}^{\infty} d_{j,k} \psi_{j,k} \quad (30)$$

The indices (j, k) indicate the level of resolution and translation, respectively. A finite, real signal, $f(t)$, can now be expressed as a wavelet decomposition using $g_j(t)$, where $f_N(t)$ is the approximation of $f(t)$ in the subspace V_N . This constrains the resolution to $1 \leq j \leq N'$. The approximation is then given by Equation (31).

$$f_N(t) = \sum_{n=1}^{N'} g_{N-n}(t) + f_{N-N'}(t) \quad (31)$$

The two-scale relations for an arbitrary j are given by Equations (32) and (33).

$$\phi(2^j t) = \sum_k p_k \phi(2^j t - k) \quad (32)$$

$$\psi(2^j t) = \sum_k q_k \psi(2^j t - k) \quad (33)$$

The relationship between successive levels of decomposition separates the signal at high resolution (HR) into two signals at low resolution (LR), and the subspace relationship is given by Equation (34).

$$V_{j+1} = V_j \oplus W_j \quad (34)$$

The orthogonal sum of the subspaces forms the HR signal from the LR signals. This can be generalized to an arbitrary resolution, j , for $l \in Z$.

$$\begin{aligned}
\phi_{j+1,l} &= \phi(2^{j+1}t - l) \\
&= \sum_k \{a_{2k-l}\phi(2^j t - k) + b_{2k-l}\psi(2^j t - k)\} \\
&= \sum_k \{a_{2k-l}\phi_{j,k} + b_{2k-l}\psi_{j,k}\}
\end{aligned} \tag{35}$$

DWT algorithms are based on subspace relationships and use divide-and-conquer to segregate a signal into constituent components at different levels. These can then be separately processed using optimized algorithms for the appropriate scale. The decomposition process, as developed thus far, consists of two discrete wavelet convolutions with a subsampling reduction by 2, as expressed by Equations (36) and (37).

$$c_{j,k} = \sum_l a_{2k-l}c_{j+1,l} \tag{36}$$

$$d_{j,k} = \sum_l b_{2k-l}c_{j+1,l} \tag{37}$$

Equation (36) determines the scaling function and Equation (37) determines the wavelet at resolution j . For each iteration, the high frequency information is extracted from the signal, leaving the lower frequency information for the next iteration of the algorithm [48]. The reconstruction of the original signal requires an upsampling operation before convolution, as given in Equation (38).

$$c_{j+1,l} = \sum_k [p_{l-2k}c_{j,k} + q_{l-2k}d_{j,k}] \quad (38)$$

There are many wavelets that can be used in DWTs. This method can be extended to N-dimensions so long as the wavelets are orthogonal in N-dimensional space. An example of the Daubechies 4, one-dimensional decomposition and reconstruction DWT filters is given in Figure 16 [49].

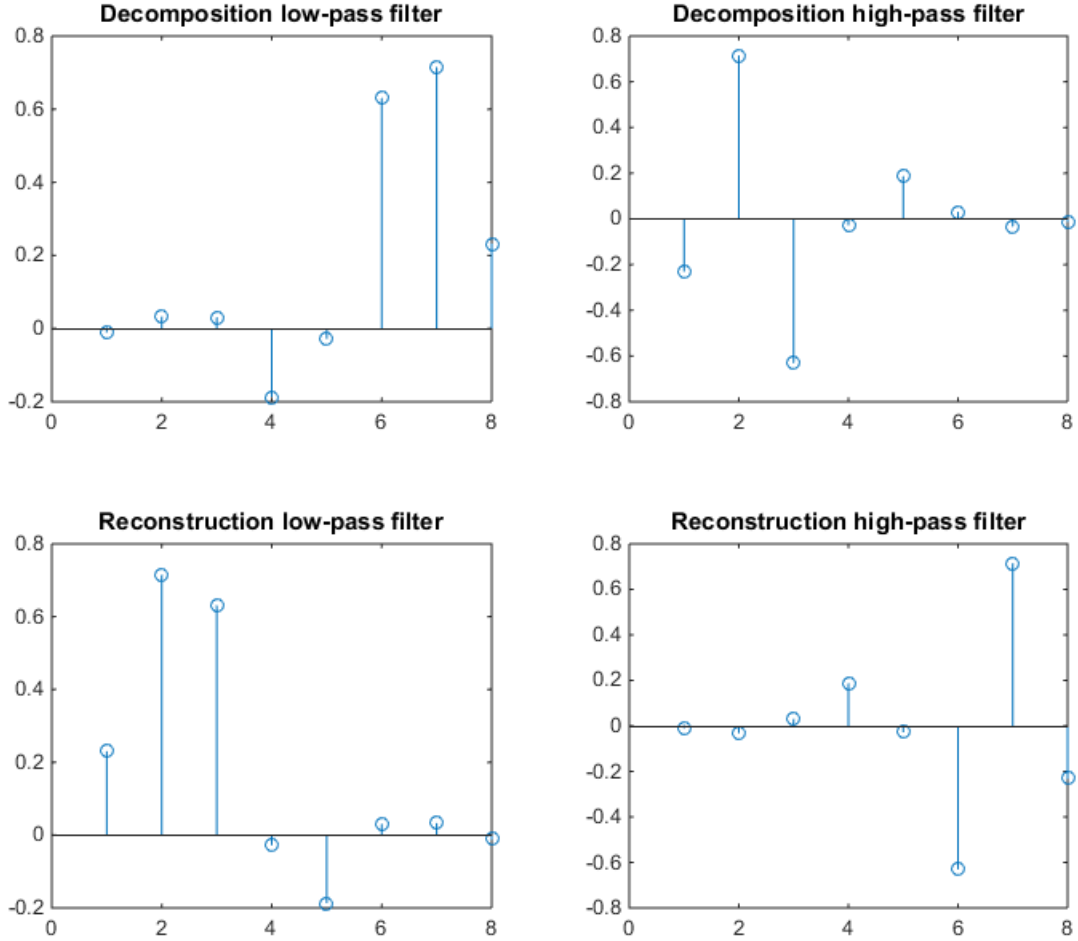


Figure 16. Daubechies 4 wavelet decomposition and reconstruction filters.

3.5. Anisotropic Resolution Neutron Image Reconstruction

The basis for anisotropic resolution reconstruction stems from the field of medical imaging in the use of Magnetic Resonance Imaging systems. The acquisition time is inversely proportional to the voxel size. For example, doubling the resolution from 2mm x 2mm x 2mm to 1mm x 1mm x 1mm takes the acquisition time from 5 minutes to 5 hours [50]. This issue led to the development of ARRT so that a volume of interest could be sampled using high resolution in two directions at once while sampling

at a lower resolution in the other direction [50]. The challenge of this method is rapidly acquiring the image data and performing the requisite reconstructions. The figure below shows, in principle, what the two orthogonal images would look like.

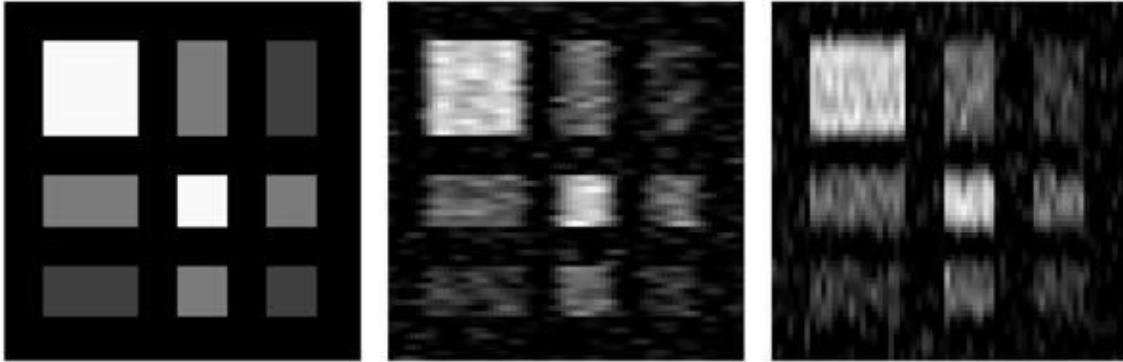


Figure 17. Data associated with 2 anisotropic NMRI scans and the reference image from which the two images were formed [50].

The image acquisition process of nuclear magnetic resonance imaging (NMRI) images is very different from the image acquisition process involved with neutron imaging. Therefore, a different approach is required to model the image distortion and to perform the higher resolution reconstructions. Fortunately, the methods required for neutron image reconstruction are, in principle, simpler than the NMRI processing techniques for two reasons: the NMRI is inherently three dimensional whereas neutron imaging is two dimensional, and image formation is described by wave-phase relationships and relaxation times for NMRI whereas neutron imaging can be described by simple geometrical relations.

The algorithm begins with the basic additive properties of the Fourier Transform and how it relates to the spatial domain of an image. Due to the fact that NMRI images

are constructed using phase information from the received signal, the FFT process is properly suited to the task. For neutron images, this information is not available, thus the DWT method is more appropriate to this solution. The *a priori* knowledge of the structure of the neutron beam allows a separation of x and y variables such that they can be treated independently in each image. This fact allows correlation between two images with orthogonal neutron illumination structures. An observation of the similarity of geometric blur and spatial frequencies yielded the method of cut-off frequencies. This method was applied for spatial characteristics that were either not in focus or to enhance the lower resolution features such as the general shape of an object without the fine detail.

3.6. Development of the Combined DWT and ARRT

ARRT has not previously been envisioned for a neutron radiography system [7], [24]. The combination of DWT and ARRT, in conjunction with the high admittance, high aspect ratio collimator, has the potential to reduce the acquisition times of high-resolution neutron images. More specifically, this work addresses creation of an algorithm that combines these two methods of image reconstruction as applied to neutron imaging with a highly anisotropic beam profile. The DWT separates the image into orthogonal and diagonal detail components and the ARRT recombines the appropriate details for image reconstruction.

3.6.1. One Level 2-D DWT MatLab Method

The easiest wavelet transform method performs the transformation on a single level and replaces the horizontal and vertical components with their corresponding HR (for edge enhancement) or LR (for noise and artifact rejection) details. The diagonal details and approximations of the images are averaged due to the absence of diagonal detail information. The diagonal detail could, in principle, be acquired by positioning the neutron collimator at an angle bisecting the two orthogonal sets. The isotropic image is reconstructed using the inverse discrete wavelet transform (IDWT).

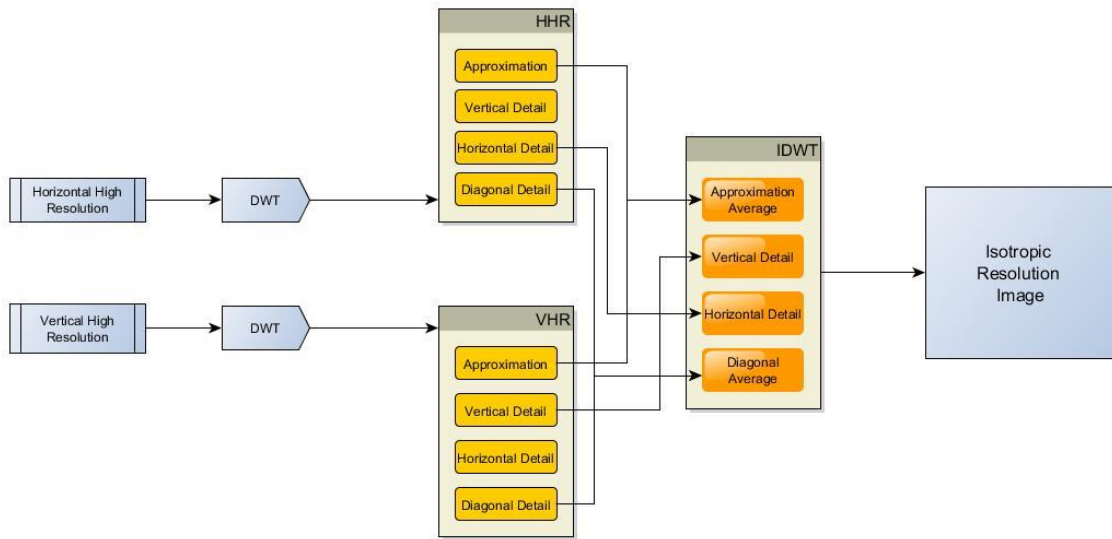


Figure 18. One-Level, 2D-DWT reconstruction process.

As will be seen in the results, this method only uses the first octave of detail and much of the underlying information persists, such that the image is approximately an average of the two data sets.

3.6.2. Bayesian Inference DWT Method

In an effort to be creative, it was decided to attempt a Bayesian statistical approach to the combination of first octave information. The Bayesian Inference method makes use of the fact that the likelihood of a certain pixel value will be close to the values represented in the high resolution image. The values in the high resolution direction are more likely to be correct versus the low resolution direction. In addition, if the pixels vary greatly from each other, then it can be assumed that this variation is due to noise and these values can be suppressed using either a Gaussian or median filter.

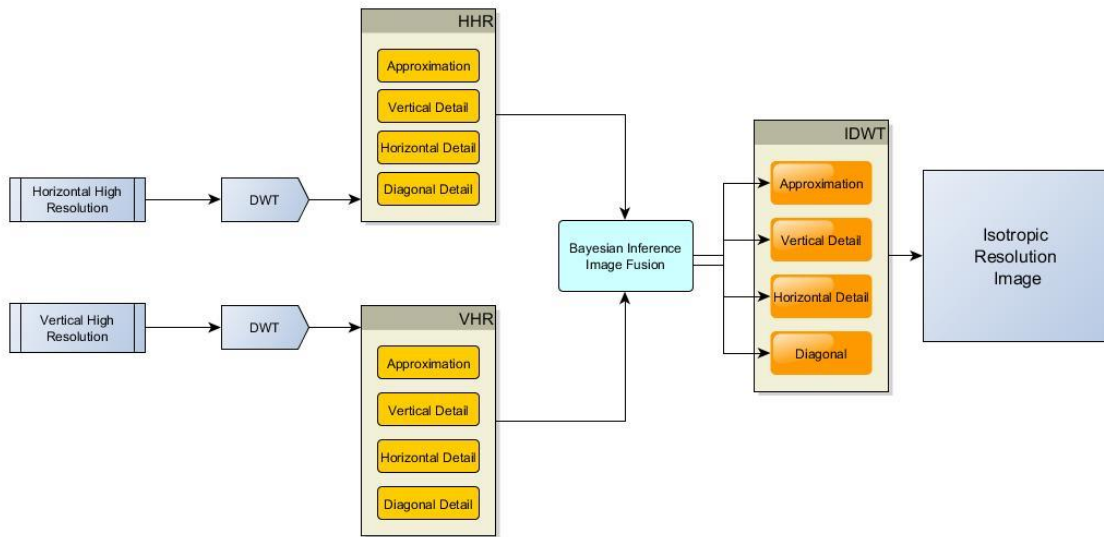


Figure 19. One level Bayesian inference DWT method.

The Bayesian inference method produced interesting results. The Bayesian estimator chosen was the Cauchy distribution due to its use in estimating the position of a radiation source. Bayes' rule is given in Equation (39), and the Cauchy function in equation (40).

$$p(I(x, y)|f(x, y)) = \frac{p(f(x, y)|I(x, y))p(I(x, y))}{p(f(x, y))} \quad (39)$$

The prior probability distribution function (PDF) is given by equation (40), and is derived graphically from Figure 20. The distance, Z , of the source from the x -axis is representative of the uncertainty in the intensity, I , and measurement, f_i , by the pixel.

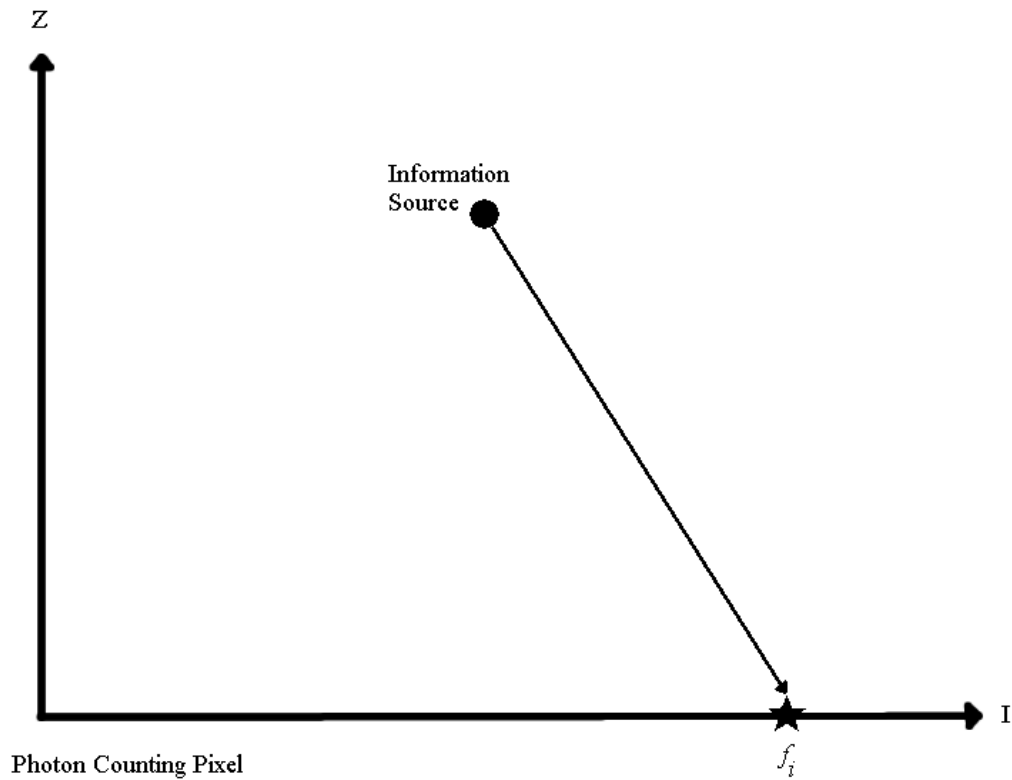


Figure 20. Cauchy distribution derivation concept.

Each x_i represents the pixel intensity value measured at data set i , and the random variations (thermal noise plus electronic readout noise) in the pixel give rise to the random sampling of the intensity distribution. Furthermore, the distribution is assumed to be uniform. This gives the sampling distribution in equation (40), which is valid for $-\pi < \theta < 0$.

$$\tan \theta = \frac{-z}{(f_i(x, y) - I(x, y))} \quad (40)$$

The prior PDF is transformed by the transformation of density functions, as given in equation (41).

$$p(f_i(x, y)|I(x, y), z) = \frac{z}{\pi [z^2 + (f_i(x, y) - I(x, y))^2]} \quad (41)$$

Applying Bayes' law yields equation (42).

$$p(I(x, y)|\{f_i(x, y)\}, z) \propto p(\{f_i(x, y)\}|, z)p(I(x, y)) \quad (42)$$

The posterior PDF is given by equation (43), which is the product of the prior PDFs and has multiple maxima as a consequence of the two data sets from which the composite is compiled. The widths of these maxima are dependent upon the relative “closeness” of the information source to the intensity line. Figure 21 was produced using a random pixel from the set of neutron images and a “closeness” value of $z = 0.015$. It is assumed that there is no prior information about the pixel intensity; therefore, the prior, $p(I)$, is constant.

$$p(I(x, y) | \{f_i(x, y)\}, z) \propto \prod_i p(\{f_i(x, y)\} | z) \propto \prod_i \left(\frac{z}{z^2 + (I - f_i)^2} \right) \quad (43)$$

The shape of the curve changes with the assumptions of “closeness” and the amount and spread in the data.

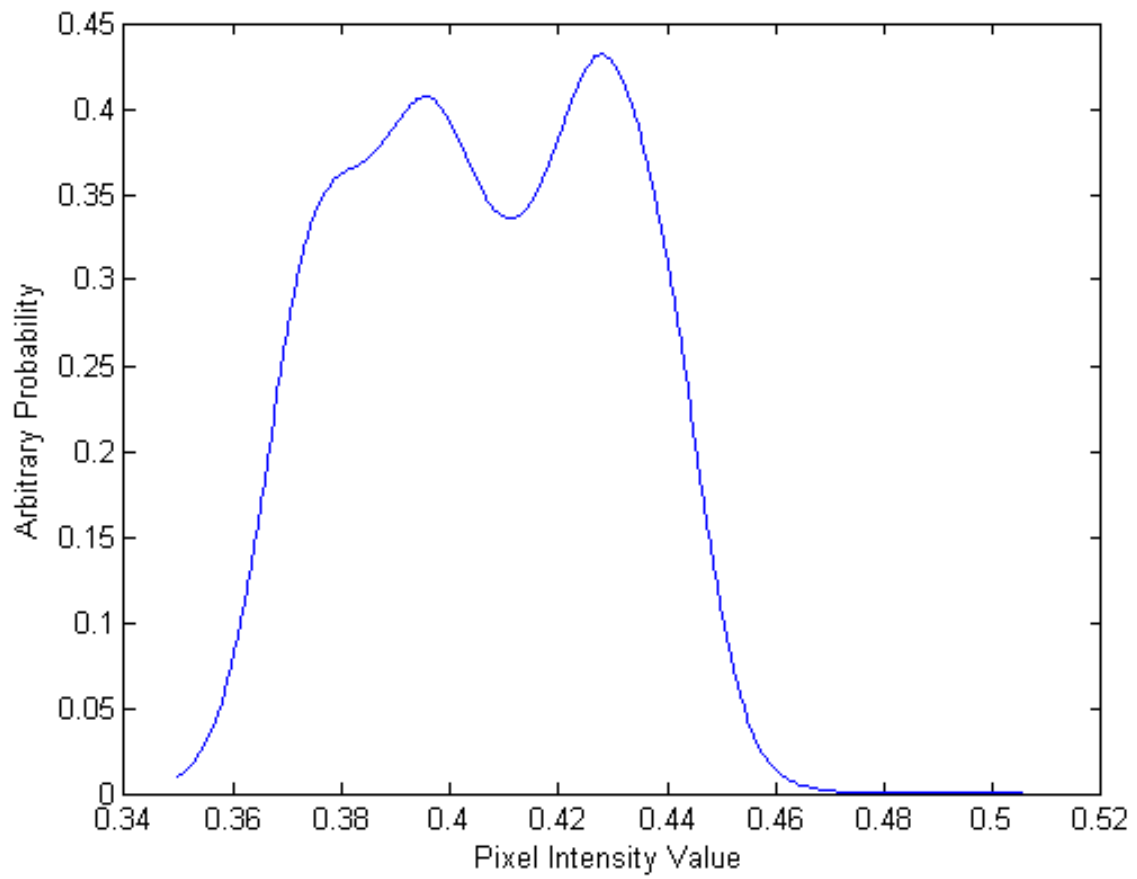


Figure 21. Cauchy distribution of intensity values.

As can be seen from Figure 21, the maximums are not of equal height, and from equation (44) the best value for the interpretation is chosen to be the maximum of the argument.

$$\hat{x} = \operatorname{argmax} \left(p(I(x, y) | f(x, y)) \right) \quad (44)$$

It is important to note that improvement in root-mean-square (RMS) error requires that there are more than two data points [51].

3.7. Multilevel DWT Edge Enhancement

Edge enhancement using the DWT is conceptually very simple: (1) decompose the image into several layers/levels; (2) average the approximations; (3) replace the vertical, horizontal, and diagonal details with their respective high resolution components. In practice, it is complicated by the fact that all of the components need to be properly tracked and the data set managed. Figure 22 explains the process of a three level decomposition and reconstruction diagrammatically.

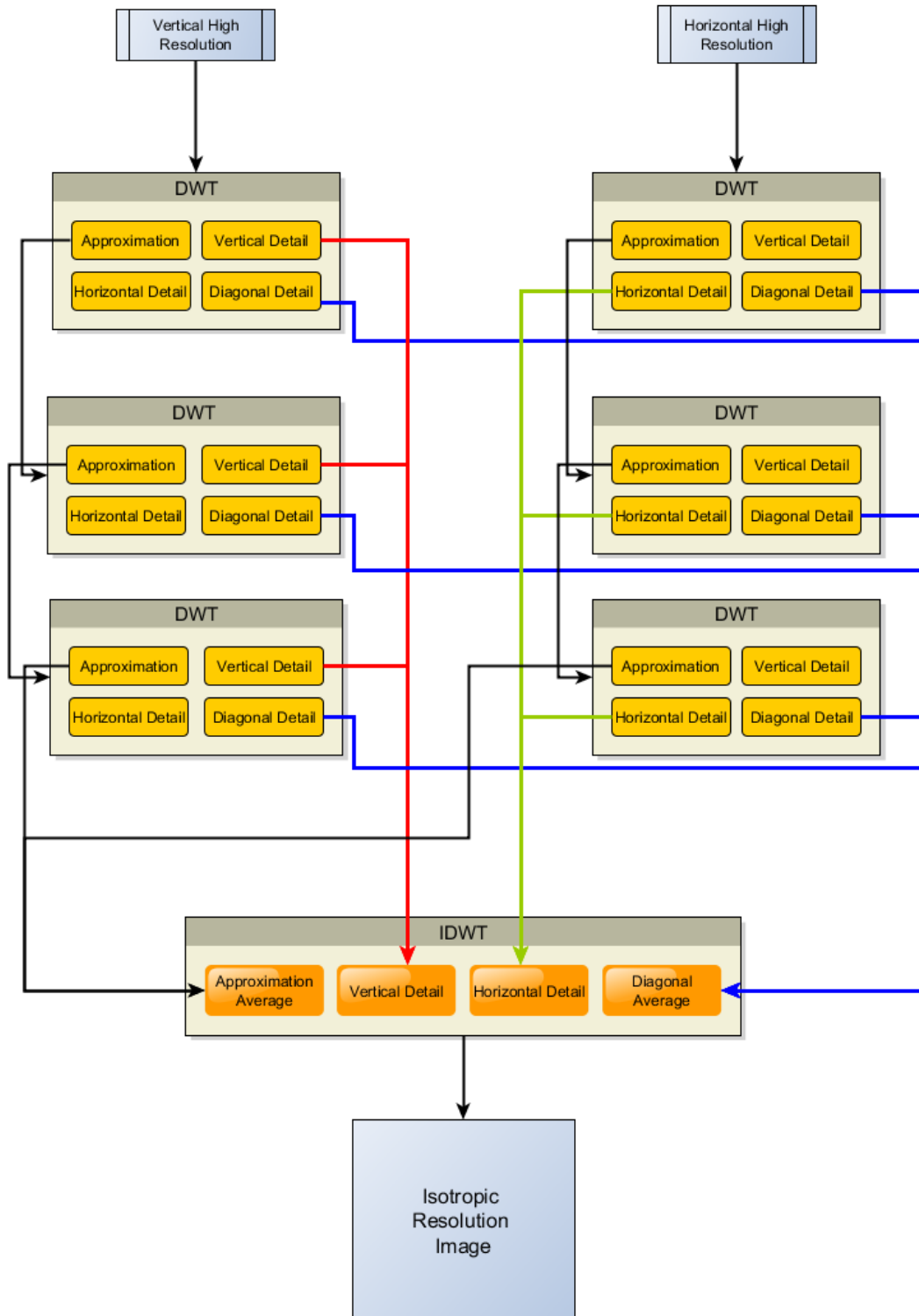


Figure 22. Edge enhancement DWT decomposition and reconstruction process.

3.8. Multilevel DWT Artifact Rejection

The reconstruction process for the artifact rejection DWT method is similar to the edge enhancement method except that the details of the vertical, horizontal, and diagonal directions are replaced by their lower resolution (low-pass) counterparts. The three-level reconstruction is depicted in Figure 23. It is beyond the scope of this dissertation to optimize the levels in which the high resolution parts are replaced with the low resolution components; this refinement is left for future work. It is quite possible that only the upper most decomposition needs to be replaced with the LR components to achieve sufficient artifact rejection.

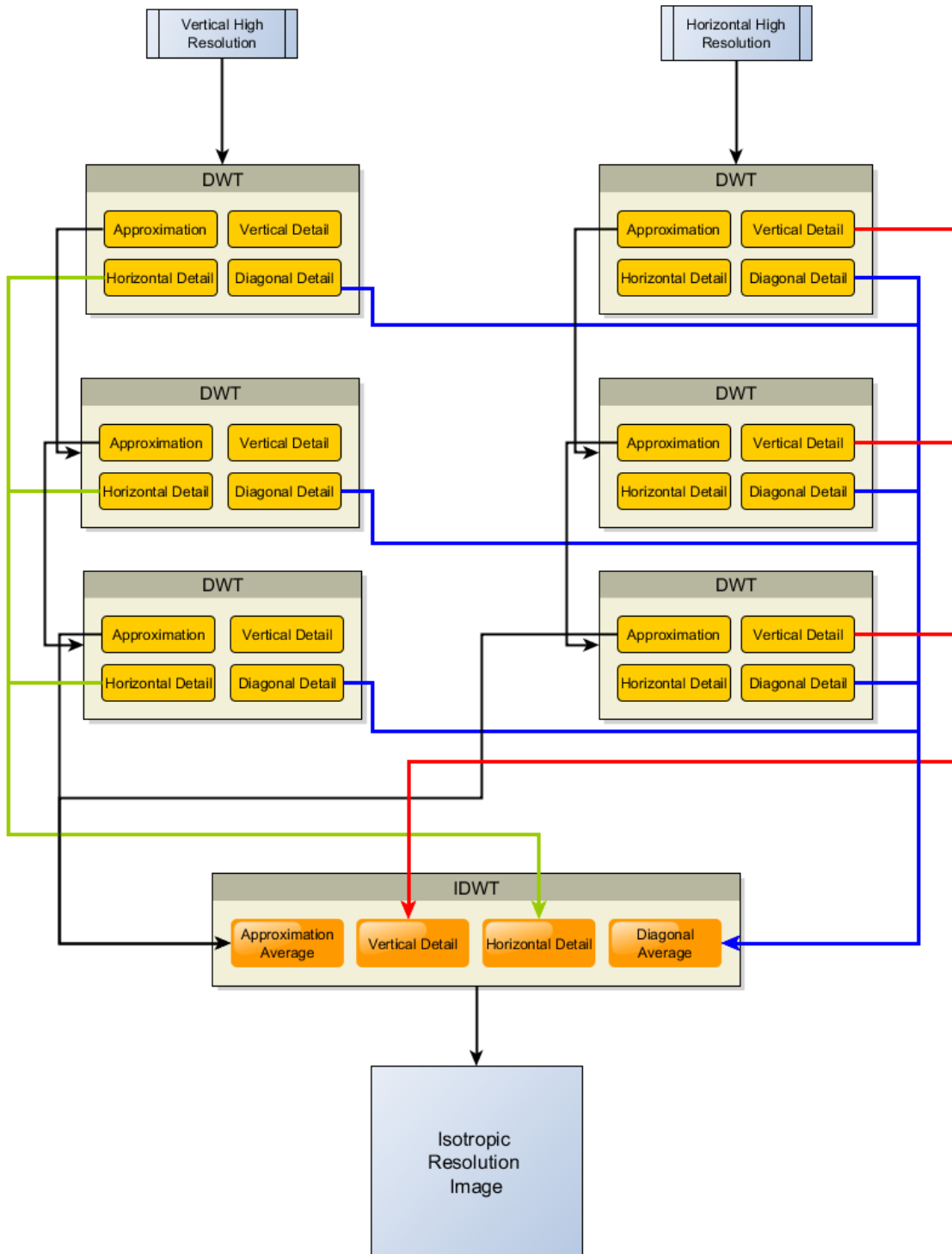


Figure 23. Artifact rejection DWT decomposition and reconstruction process.

3.9. Image Reconstruction Test Image

In order to gauge the algorithm's ability to properly reconstruct a high-resolution, low SNR image, there must exist some ground truth image in which these quantities are at their theoretical maximum (in this example the maximum would be infinite due to the absence of noise). The intensity values in these images are on the range of zero to one with black being zero and white being one.

3.9.1. Test Image Objects

A set of geometric objects were chosen to identify the reconstruction algorithm's strengths and weaknesses. These shapes had curves and straight edges at different orientations and intensity magnitudes. Figure 24 is the ground truth image before degradation and Figure 25 is a close up of the region of interest (ROI) to elucidate edge detail. The ROI was chosen to investigate the behavior of the algorithm for orthogonal edges. The edges at other orientations provide the basis for the analysis of off-normal behavior.

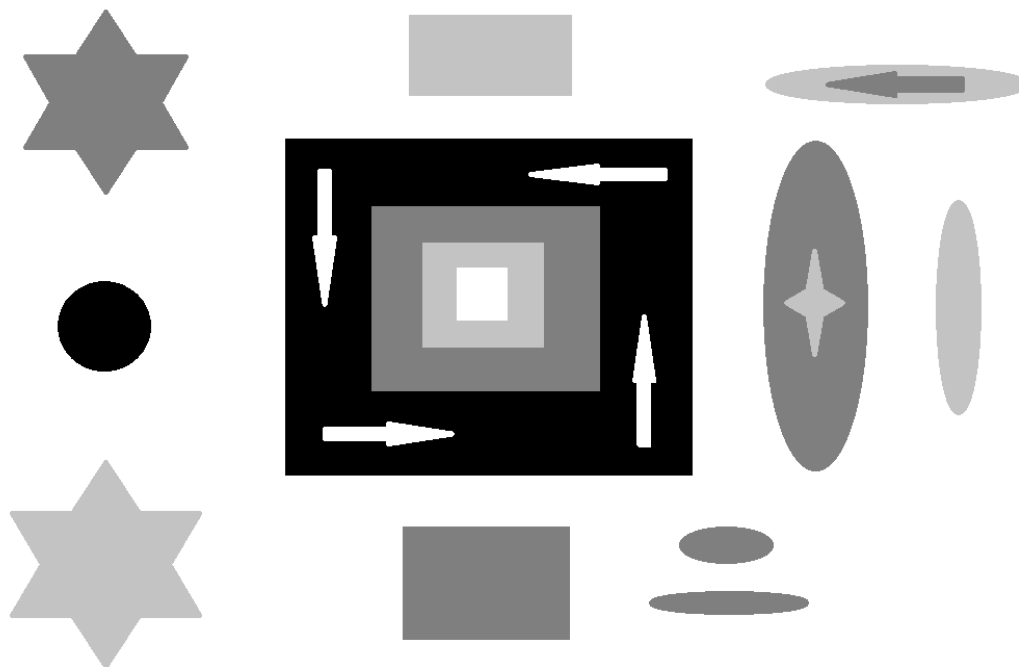


Figure 24. Ground truth image before degradation.



Figure 25. ROI for the initial image before degradation.

The absolute lack of noise in the ground truth image sets the null background that should be (theoretically) achievable in the image reconstruction process. This also sets the maximum signal to noise ratio for the image with signal at maximum and noise at zero. Figure 25 displays the infinite SNR property of the ground truth image.

3.9.2. Simulated Anisotropic Blur and Noise

A method was developed to simulate the anisotropic blur effects of a highly anisotropic neutron beam profile. The known initial image is critical to assessing the performance of the DWT ARR method algorithm. The anisotropic blur was applied to the ground truth image to simulate the blur obtained from the collimator orientations, and the results of this operation are shown in Figure 26.

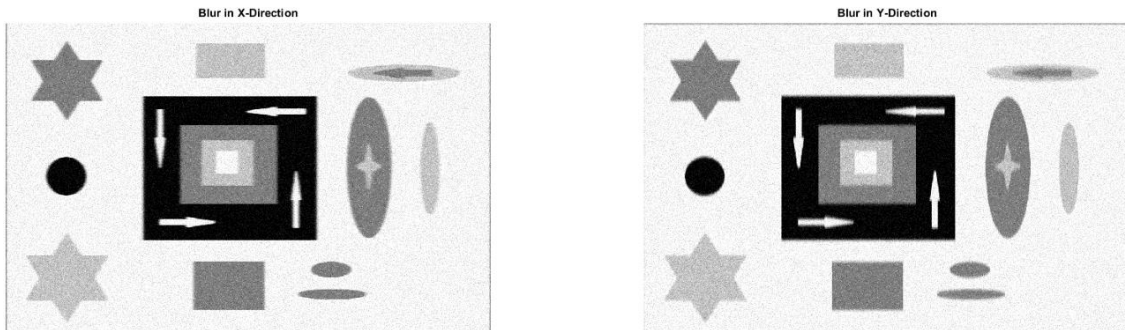


Figure 26. X-direction blur (left); Y-direction blur (right).

The ROI for the anisotropic blur is shown in Figure 27. The blur filter used a 2D Gaussian profile with the asymmetric blur parameters given in Table 2.

Table 2 Degradation Parameters

Parameter	Value	Unit
Deviation Low	0.5	Sigma
Deviation High	3	Sigma
Width Low	3	Pixels
Width High	31	Pixels

This filter was rotated 90 degrees to yield the orthogonal blur required to test the image reconstruction techniques. The results of this filter are given in Figure 27.

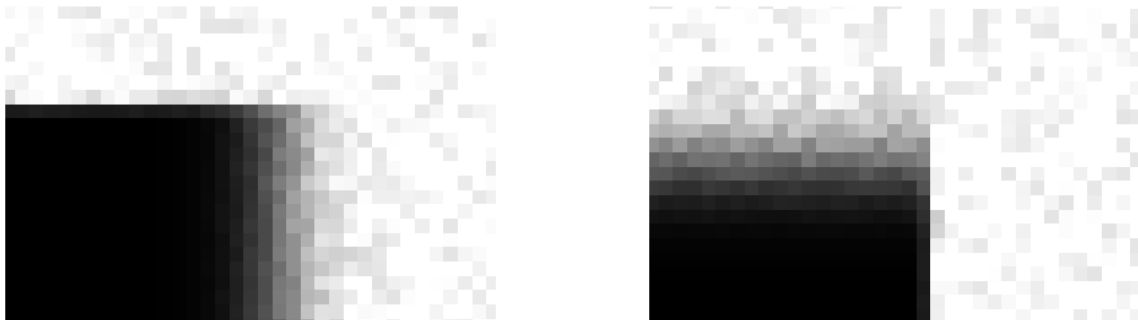


Figure 27. ROI for test images.

3.9.3. DWT Reconstruction Method Results

The developed DWT ARR method is well suited to isolate the known high fidelity components of image signals and the capacity to recombine this information in such a way as to maximize human interpretation.

3.9.3.1. One-Level, 2-D DWT MatLab Method

The one-level, 2-D DWT is the simplest method for DWT reconstructions for anisotropic resolution images. The method decomposes the image using the DWT method once, the details for the horizontal and vertical image sets are taken, and the image approximations and diagonal details are averaged together. This synthesized set of data is used in the image reconstruction process. The result of the one-level method is shown in Figure 28. The first wavelet discovered was the Haar wavelet. The first wavelet series discovered was the Daubechies series, of which the Haar wavelet was determined to be a specific case [49].

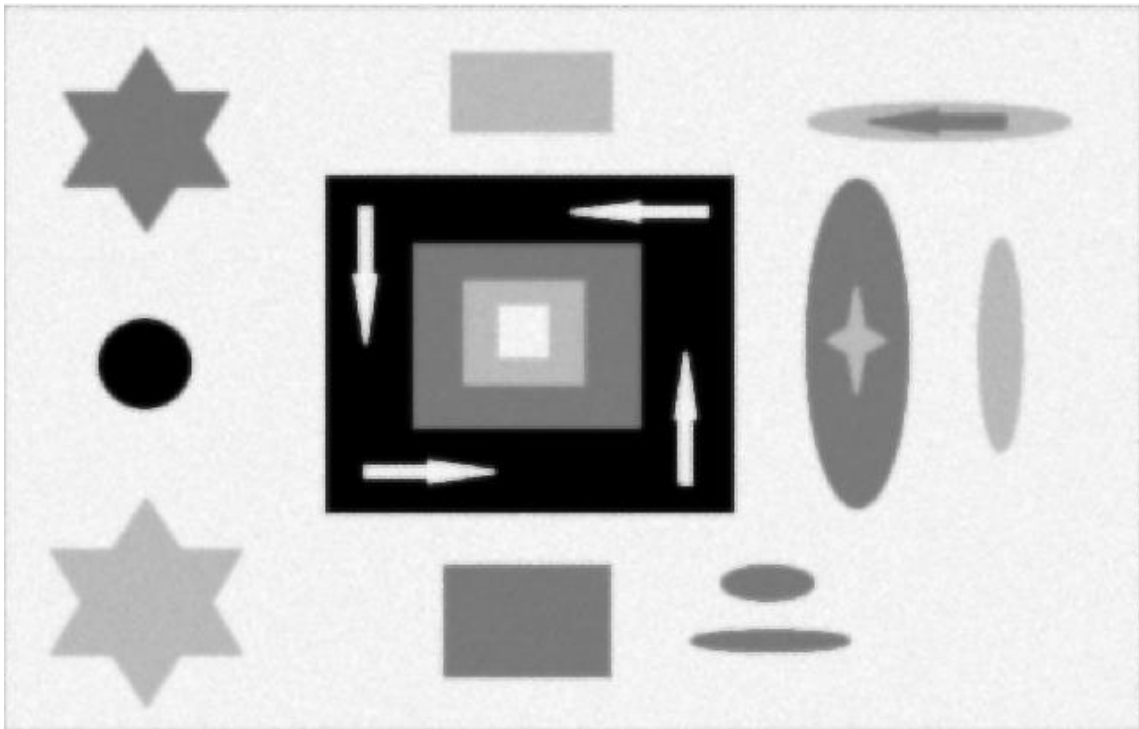


Figure 28. Image reconstruction using the simple two-dimensional DWT method using the built-in MatLab functions.

The ROI for the one-level method, shown in Figure 29, makes apparent that it is not detectably better than the average of the two images; thus, the method must be expanded to the multilevel DWT method. This reconstruction also omitted the Wiener prefiltering step to demonstrate the implications of noise in images.

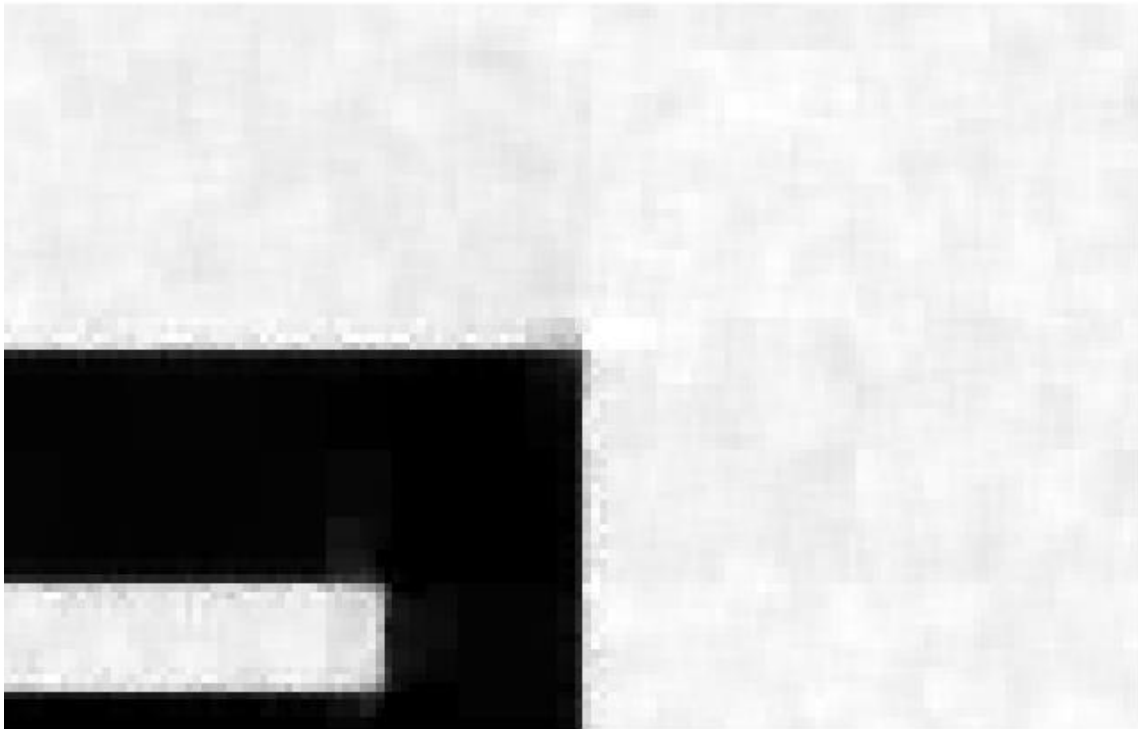


Figure 29. ROI for one-level, 2D-DWT reconstruction method.

The one-level, 2D-DWT reconstruction algorithm takes the high frequency data from both images, which includes the noise, thereby increasing the noise component in the reconstructed image. Therefore, a smarter reconstruction approach is necessary.

3.9.3.2. Multilevel DWT Method

The multilevel DWT method decomposes the image set down to the most fundamental similarity between the anisotropic images before averaging the elements and the reconstructing the image from the ground up using either the LR components for noise and artifact rejection or the HR components for resolution enhancement. For this reconstruction the Haar wavelet was chosen due to its simplicity [49].

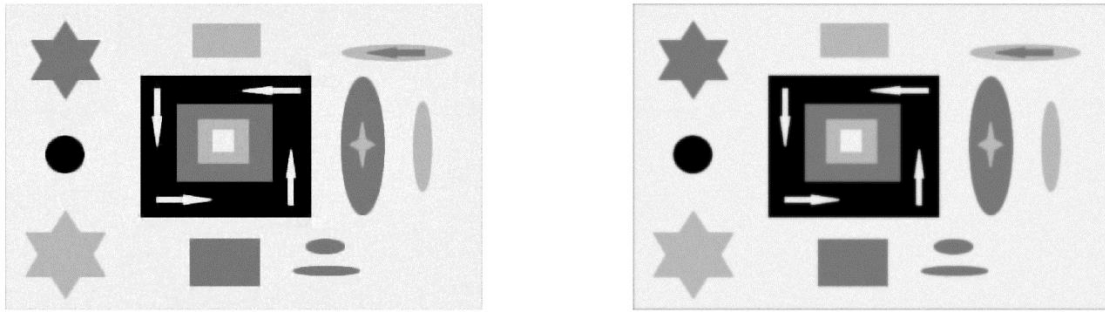


Figure 30. Wavelet reconstruction (left), image average (right).

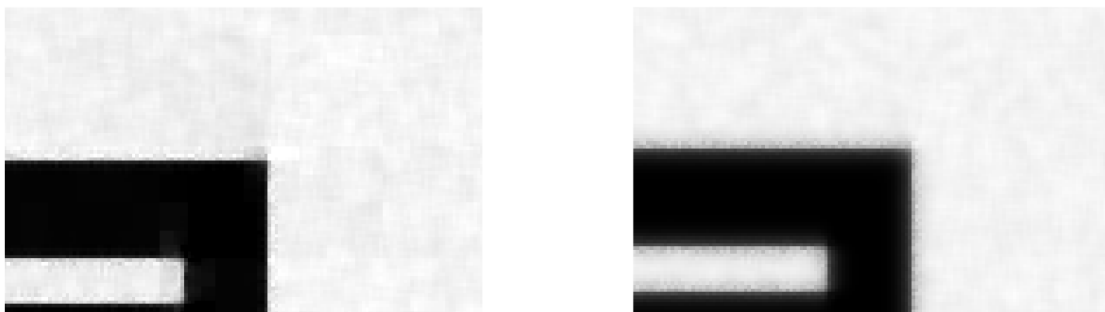


Figure 31. ROIs for Haar wavelet reconstruction (left) and average (right).

Further examination of the ROIs yielded obvious visual differences between an average and the DWT ARR methods. Consequently the DWT ARR methods are superior in this reconstruction regime.

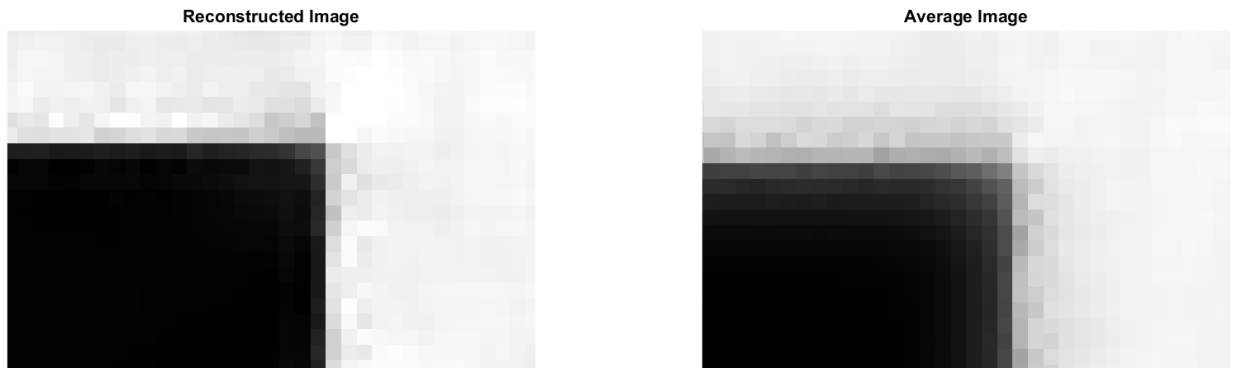


Figure 32. ROI close up comparison of the reconstruction method and average of the two images.

It can be seen by observing the cascade of approximations that the images obtained by blurring in two orthogonal directions would become self-similar at the maximum wavelet decomposition. At this level, the two images would be indistinguishable from one another. Thus, the image can be reconstructed using the known HR detail (for image sharpening) or LR detail (for first level artifact removal) to yield the desired result. The approximation cascade is given in Figure 33.

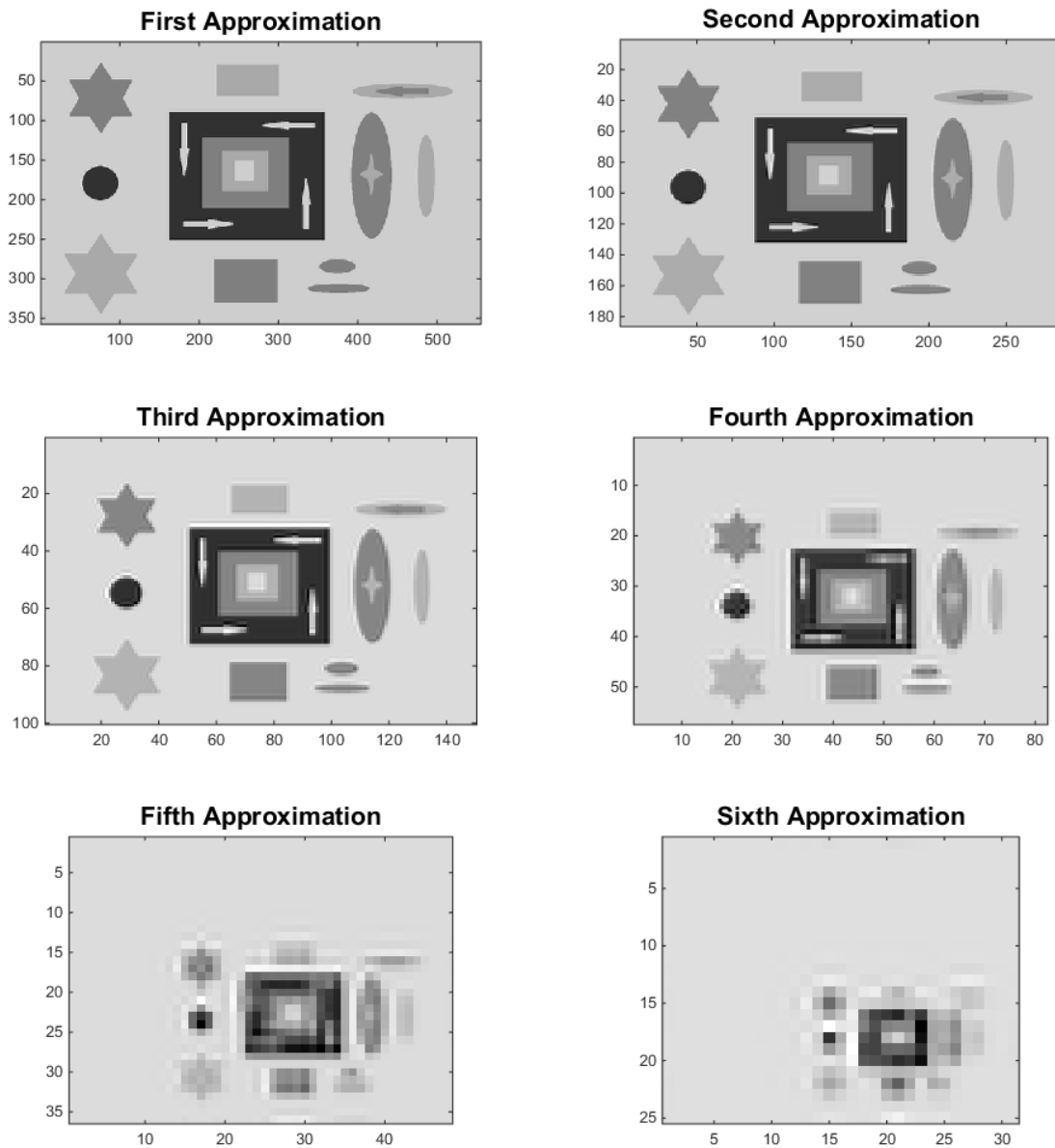


Figure 33. Approximation cascade

3.9.3.2.1. Sensitivity Analysis of Wavelet Complexity and Reconstruction Quality

It was observed that there was an optimization for wavelet complexity and image quality. The more complex the wavelet, the fewer levels of decomposition could be

performed on the image set, and thus a lower level of similarity can be reached before the images are then reconstructed level-by-level, yet the simplest wavelet produces tile-shaped image artifacts. Figure 34 shows the differences in the image reconstruction process depending on the wavelet that was used and the resulting image artifacts.

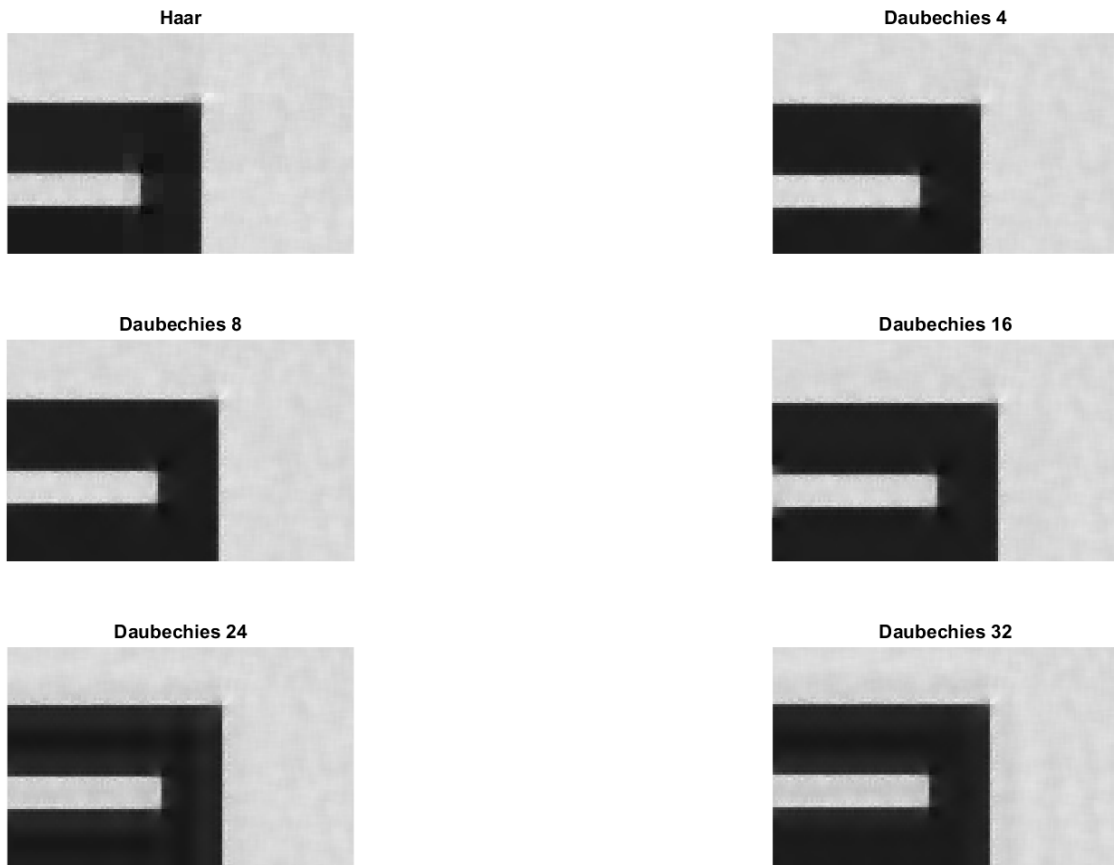


Figure 34. Sensitivity of wavelet complexity.

It is interesting to note that, regardless of the wavelet used for reconstruction, that any edges that do not run parallel to a reconstruction direction are blurred. It is hypothesized that the use of directional wavelets in conjunction with image sets acquired in the off-normal orientations would be able to resolve these edges, but this is beyond

the scope of this dissertation. Figure 35 shows the ROI for edges with off-normal orientations and the lack of the ability of the algorithm to resolve these edges.

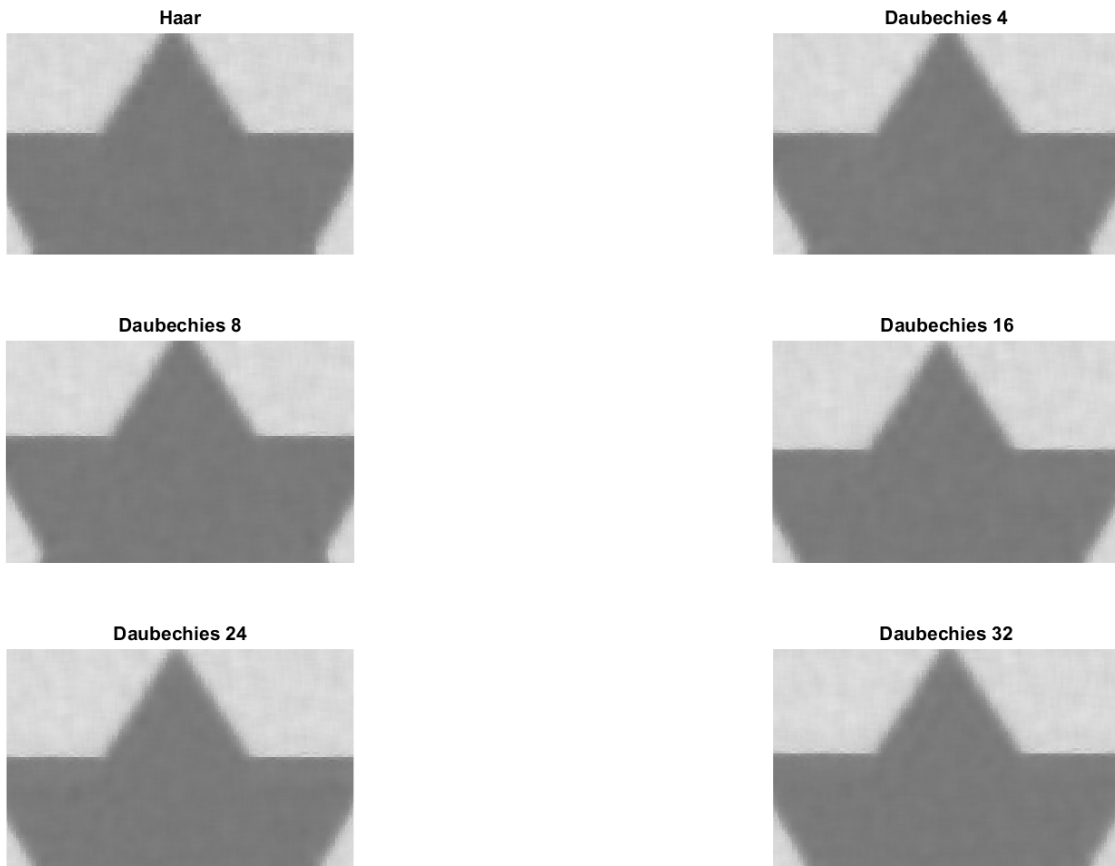


Figure 35. ROI of off angle edges.

3.10. Implementation of the Developed Reconstruction Algorithm

The operational aspects of combining the two approaches are very simple: a series of images is taken in two orthogonal directions and then processed to provide one HR image. One set of images is acquired with the collimator in one orientation. The high

aspect ratio (Söller collimator) of the neutron beam is then rotated 90 degrees, and another set of images is taken. This gives a set of images that will have a high resolution in one direction and a low resolution in the orthogonal direction [27].

The image reconstruction process follows this basic path: image normalization, gamma noise filtration, DWT transformations, image-data manipulations, sorting, averaging, and decomposed image DWT reconstruction. The images had to be normalized so that the average image intensity and standard deviations were scaled properly with another data set. This was necessary due a slow oscillation in reactor power that resulted in a less-than-subtle difference in beam luminosity. Once the images were normalized, a Wiener filter was applied to remove thermal and gamma-induced noise from the images. The cleaned-up images were then ready to be processed using the DWT methods, breaking up each image into its vertical, horizontal, and diagonal details at several length scales. The image detail data was then sorted according to high/low resolution detail and decomposition level. The longest length scale (which corresponds to large area image averages) was used as the starting point for the image reconstruction. The image was reconstructed with the inverse DWT algorithm `waverec2` in the Image Processing MatLab toolbox.

4. EXPERIMENTAL SETUP AND MEASUREMENTS

For every hypothesis, the ultimate test of its merit lies in experiment. Thus, to take this concept beyond the realm of hypothesis and into the fires of theory, we must perform experiments to validate the hypothesis. The experiments were performed at the Texas Engineering Experiment Station (TEES) Nuclear Science Center (NSC) facility near the Easterwood Airport in College Station, TX. The researcher was given full authority and responsibility on the renovation, design, and build of this project. During the entire process, all personnel monitored their radiation dosimeters and wore the proper protective equipment.

4.1. Layout

The neutron source for the neutron radiography system is the TEES NSC 1 MW TRIGA-fuel reactor (it does not have an official “Mark” designation due to the fact that the core design is not General Atomics’ design) [52]. The facility includes two beam lines and a thermal column, which is currently inoperable.

The experiment was setup on beam port 4, which is located at the north end of the lower research level. The Figure 36 is a schematic layout of the relevant features of the lower research level in regards to the experimental system.

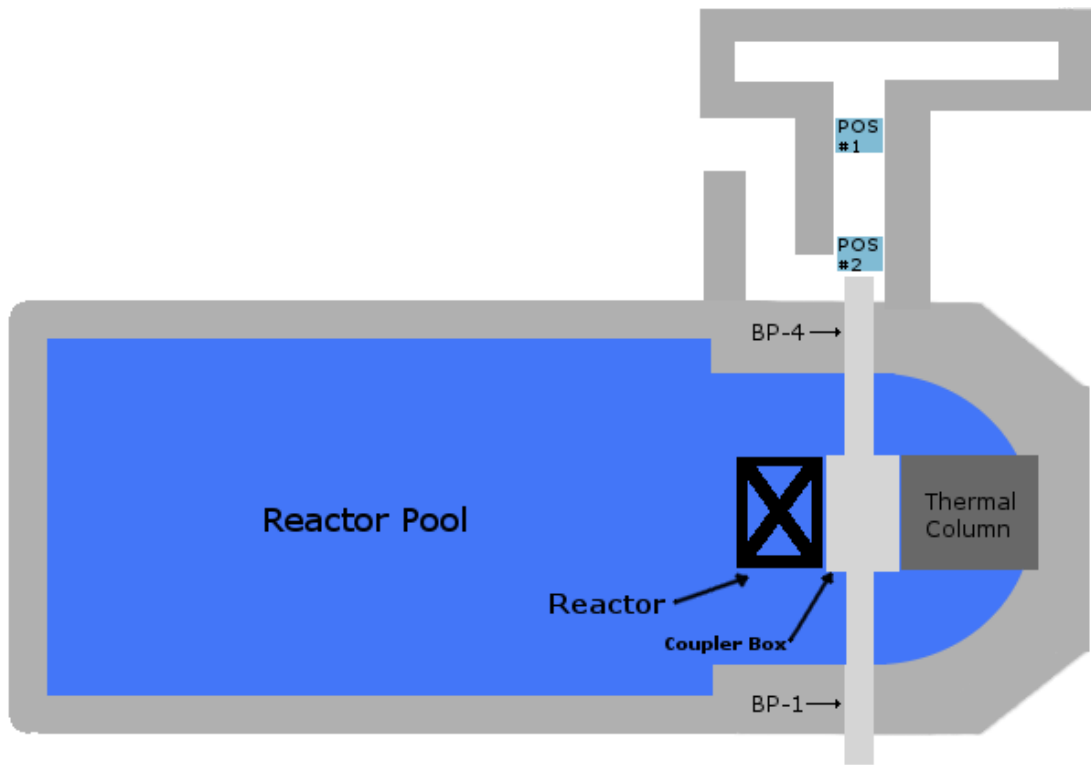


Figure 36. General layout of the neutron radiography facility at the TEES NSC.

The layout in Figure 36 is currently being remodeled and will look different in the future after the lower research level is renovated.

4.2. Beam Port Cave Renovations

The beam port cave was in a state of disrepair when the work building the neutron imaging system began. Work proceeded by first assessing the state of the cave and estimating the type of work and quantity of man-hours needed to complete the objective. Second, the old, film equipment needed to be removed to make room for the new digital imaging equipment. Third, the camera racks and object stages had to be built and installed into their respective locations within the beam port 4 radiography cave to

complete the experimental system setup. Before work could begin on the radiography cave renovations, the area was swept for radioactive contamination.

4.2.1. Cave Assessment

Through investigations of paperwork and film from the previous user, it was determined that the neutron radiography cave and supporting structure had not been used for radiography since 1994. The dimensions of the interior of the cave were measured so that a design for the camera racks could be produced. Figure 37 and Figure 38 show the measurement of the vertical and horizontal clearance of the perpendicular portion of the radiography cave.



Figure 37. Measurement of the width of the perpendicular portion of the radiography cave.

The presence of unlabeled wiring, fixtures, and hydraulics required an assessment of the electrical circuits to determine the safety of the working environment. The circuits were traced to the corresponding power distribution boxes, deactivated, and locked out for personnel safety. The electrical circuits were then rechecked with a noncontact voltage tester to ensure the safety of personnel.



Figure 38. Measurement of the height of the perpendicular portion of the radiography cave.

4.2.2. Film Equipment Removal

Once the radiography cave had been assessed for safety of personnel, and the cave dimensions had been measured, the neutron radiography film equipment could be

removed. The most difficult piece of equipment to remove was the film tray and trolley track rack in Figure 39. This required the removal of a portion of the radiography cave shielding wall.



Figure 39. Neutron radiography film tray and trolley track rack.

The hydraulic lift support blocks in Figure 40 had to be removed after the lift was removed using a dolly. While working in front of the beam port opening, a radiation meter was used to monitor the potential dose. Lead shielding blocks were used to reduce the radiation field that was transmitted through the beam port from the reactor.



Figure 40. Hydraulic vertical lift support blocks.

The concrete support blocks were removed and the floor was swept and mopped. The presence of a large amount of potentially radioactive dust made it necessary to wear a respirator and coveralls. Personnel radiation safety was ensured through periodic swipes and monitoring with the hand and foot radiation monitors. Figure 41 shows the “cleaned” neutron radiography cave.

Part of the radiography cave shielding wall was removed to allow the removal of the neutron radiography film tray and trolley track rack. This was determined preferable over the use of a plasma cutting torch in a confined space. Figure 42 shows the outside of the shielding wall before it was removed and Figure 43 shows the interior of the cave after the shielding wall and the neutron radiography film tray and trolley track rack were removed.



Figure 41. View of the radiography cave as seen from the beam port opening.



Figure 42. Portion of the shielding wall that was removed to allow the removal of the neutron radiography film tray and trolley track rack.



Figure 43. View from inside the perpendicular portion of the cave after the removal of the film tray and trolley track rack.

4.3. Experimental System Setup

The experimental apparatus made use of existing parts and materials whenever possible. The TEES NSC has a wealth of spare parts and extra materials that were used

for construction of this system including many of the servos, cameras, and structural materials.

4.3.1. Neutron Collimator

The neutron collimators are EuroCollimators of the Söller slit type with two different foil spacing distances. These collimators are shown in Figure 44. It was found early in the testing that the collimator (which will now be referred to as Collimator A) with the fine spacing had an unsatisfactory beam luminosity pattern. This collimator will allow higher resolution measurements of smaller objects of approximately 5cm by 5cm. The collimator with the larger spacing had satisfactory beam-luminosity and homogeneity. It is apparent in Figure 44 that the smaller spacing on Collimator A experienced more difficulties in the manufacturing process. The apparent larger size of Collimator B is due to an optical illusion resulting from Collimator B being closer to the camera.

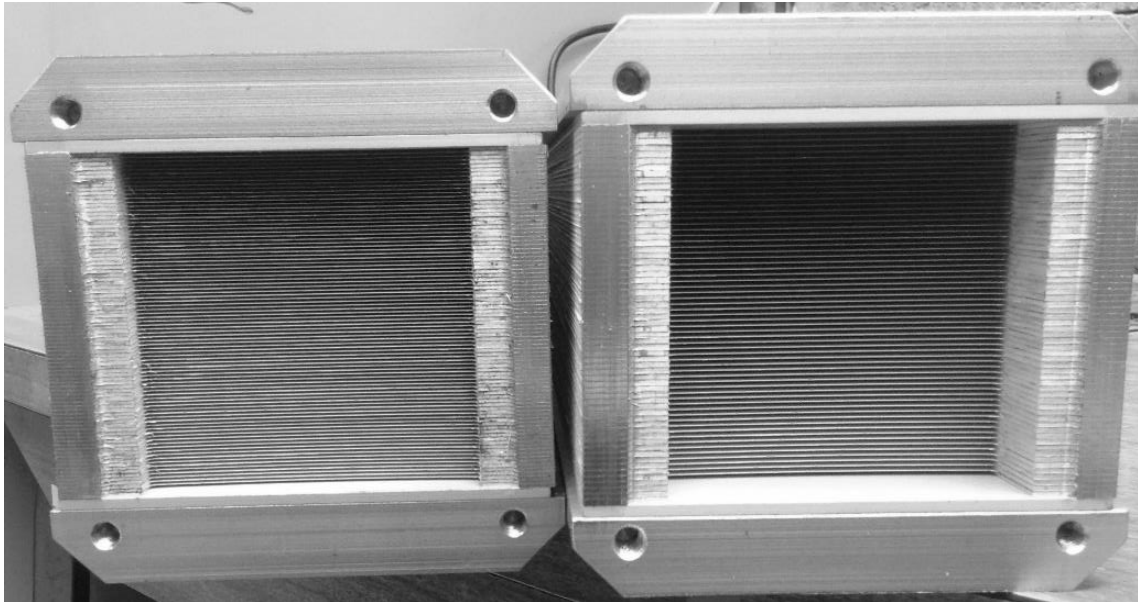


Figure 44. Collimator A (left) and Collimator B (right).

4.3.2. Neutron Imaging System 1

The Neutron Imaging System 1 (NIS1) is a long baseline imaging system that was to yield a higher resolution due to the factors involved with geometrical blur, but it was found that atmospheric neutron scatter almost cancelled the positive benefits of a longer baseline. The requirement for a large range in adjustability led to the use of the long sliding track in Figure 45.



Figure 45. Lower camera rack frame with precision sliding track.

The completed NIS1 is shown in Figure 46; this was shortly before removing the protective plastic film from the front surface mirror and before wrapping the outer rack in opaque, black plastic. The opaque plastic was to reduce the amount of stray light entering the camera, which tends to decrease the SNR. Figure 47 is a close up of the camera sled; the sled required approximately 10 kg of lead to improve the stability of the roller bearings on the track.

The completed and installed NIS1 is shown from the interior of the device in Figure 48. The power cord for the camera power supply was too short to reach from inside the control room. It was cut and spliced to a longer cord and then heat shrink tubing was applied to the splice joints to insulate the electrical cables. A coaxial cable was run to the camera from an Arduino microcontroller as an external trigger to automatically acquire the images during a tomographic reconstruction.



Figure 46. Assembled camera rack with front surface mirror mount and camera sled.



Figure 47. Side-view of the assembled camera rack with mirror mount.



Figure 48. Images of the NIS1 with the scintillator and holder (left) and the camera and sled (right).

4.3.3. Neutron Imaging System 2

The Neutron Imaging System 2 (NIS2) was built on a shoestring budget out of materials on hand and surplus parts. The stepper motors used for the stage articulation are spare control rod drive motors that were repurposed from a previous experiment. The camera base and uprights were repurposed material from the original film imaging system that was removed to make room for the new imaging systems. The object stage positioning x-y slider and mount was repurposed from another unused experiment.

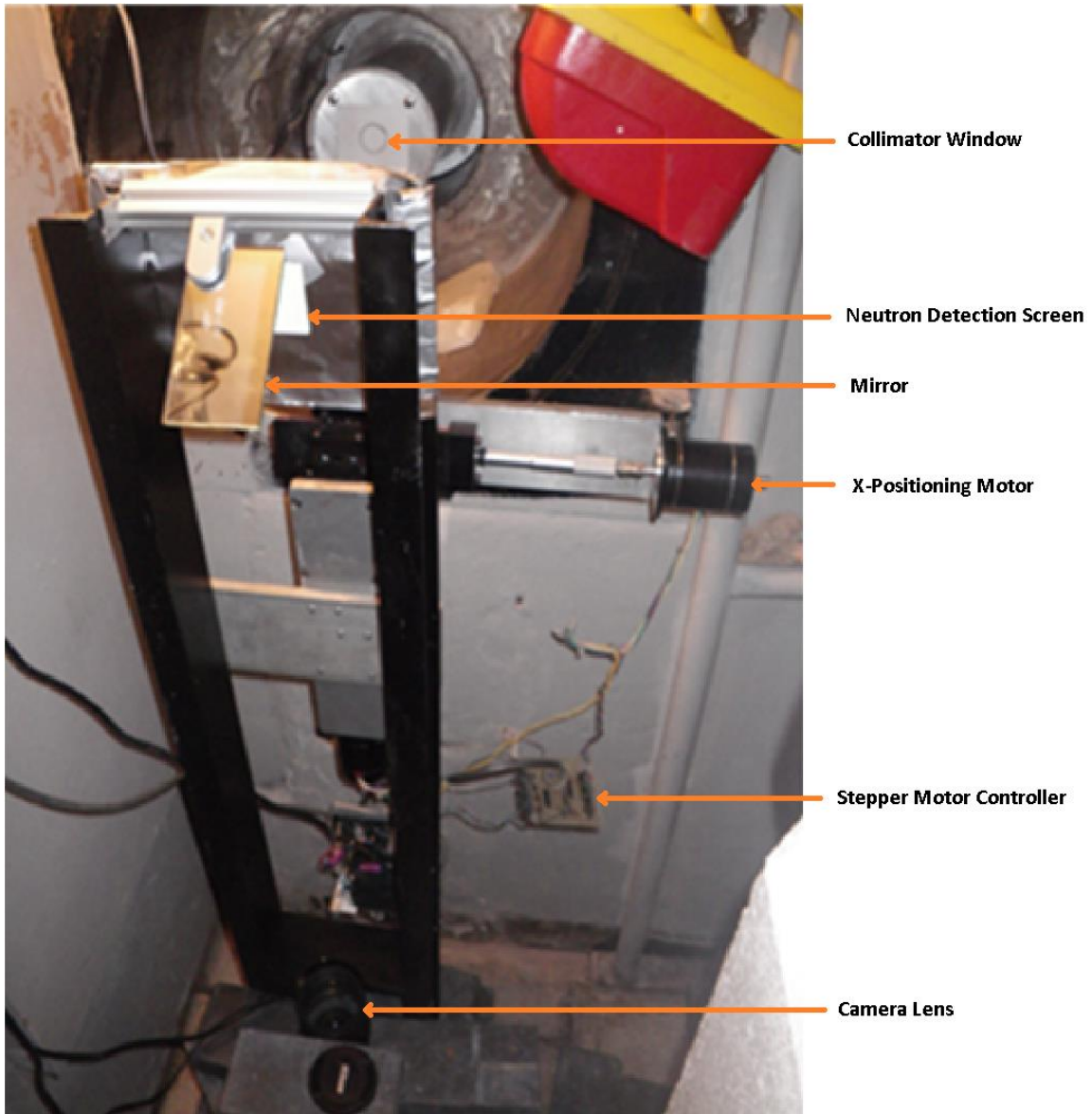


Figure 49. Experimental, high-resolution neutron camera, NIS2.

4.4. Data Acquisition System

As a result of the experiment's custom nature, an auxiliary program specifically designed to handle all of the automation of data acquisition will be produced. The software package will make use of MatLab and its extensive library of image processing, display, and instrument control tools. The use of existing code kernels and packages is of

paramount importance to complete the project on time and on target. The software package will perform the following tasks:

1. Monitor system health
2. Position the sample stage
3. Set and trigger the CCD camera
4. Acquire image data
5. Preprocess image data
6. Perform reconstructions
7. Display image data

All of these functions were satisfied to produce coherent neutron radiography data and was usable to other experimenters. MatLab has a built-in code package for hardware control called the Instrument Control Toolbox™ that contains several protocols for communicating with instruments and peripherals. The toolbox allows the communication of several devices over a USB link, which includes all the servos, neutron shutter, camera settings, and camera shutter; the entire data acquisition process is automated. The basic software and controls layout is given in the Figure 50; the software was compartmentalized to simplify debugging and readability.

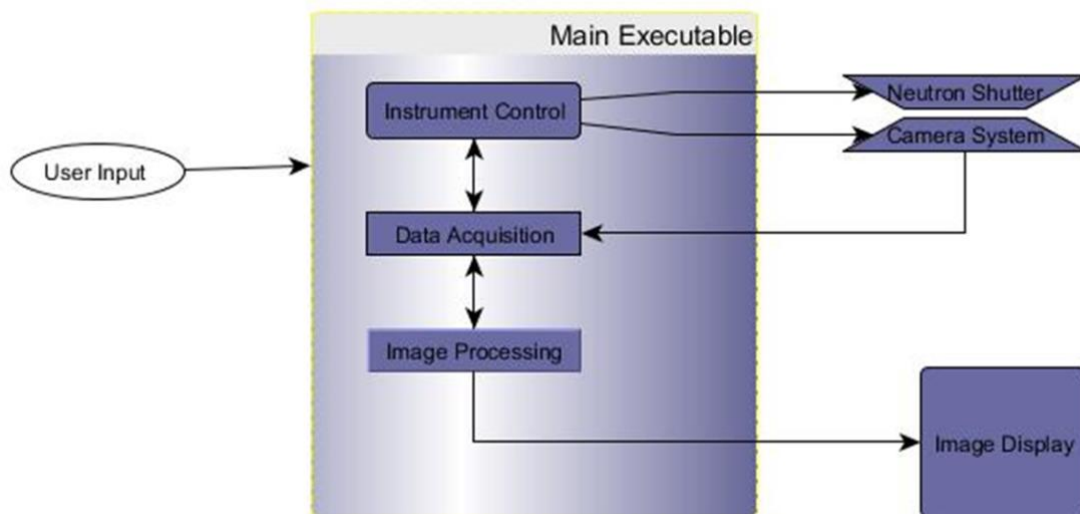


Figure 50. Conceptual representation of the neutron imaging data acquisition and control system.

4.4.1. Computer

The computer used for this setup is a 15 inch, 2010 Macintosh MacBook Pro with 8GB RAM, Intel-core i7, and 250GB SSD running OS 10.9 and Windows 7 on Boot Camp. Several attempts were made to run both software suites on the Mac OS, but these proved to be futile. The MatLab and National Instruments' LabVIEW software were only compatible with each other on the Windows 7 operating system (OS).

4.4.2. Digital Input/Output (DIO) Device

The instrument control is achieved through a National Instruments USB-6501 with 24 digitally configurable input/output channels and one 32-bit counter. It was able to output +5V signals for the control of all the servos, neutron shutter, and external camera shutter. The digital channels were limited to 8.5 mA and the total current output

was limited to 1 A; this limit is the maximum current that could be supplied by the USB cable from the DAQ computer [53].

4.4.3. System Articulation

Articulation of the experimental system is achieved using 3 stepper motors connected to the main computer through the USB-6501 DIO device. The XY positioning stepper motors were connected through a stepper motor driver board that was previously attached to the stepper motors; no model number was available for reference. The rotational step motor was connected through a micro stepper driver that allowed fractional steps for higher precision.

4.4.4. XY Positioning System

The XY stepper driver and stepper motors commandeered from a dismantled experiment. These motors are the same units used for the control rod drives on the reactor). A few problems were encountered in the process of integrating the control system with the driver. One problem manifested itself in the form of errant/erratic stepping of the XY motors. This turned out to be easily solved by adding pull down resistors to the input circuits of the driver board (the NI LabVIEW DIO device did not have sufficient resistance in the digital circuit to bleed the excess charge to the circuit ground after the output was turned off). These pull down resistors can be seen in Figure 51.

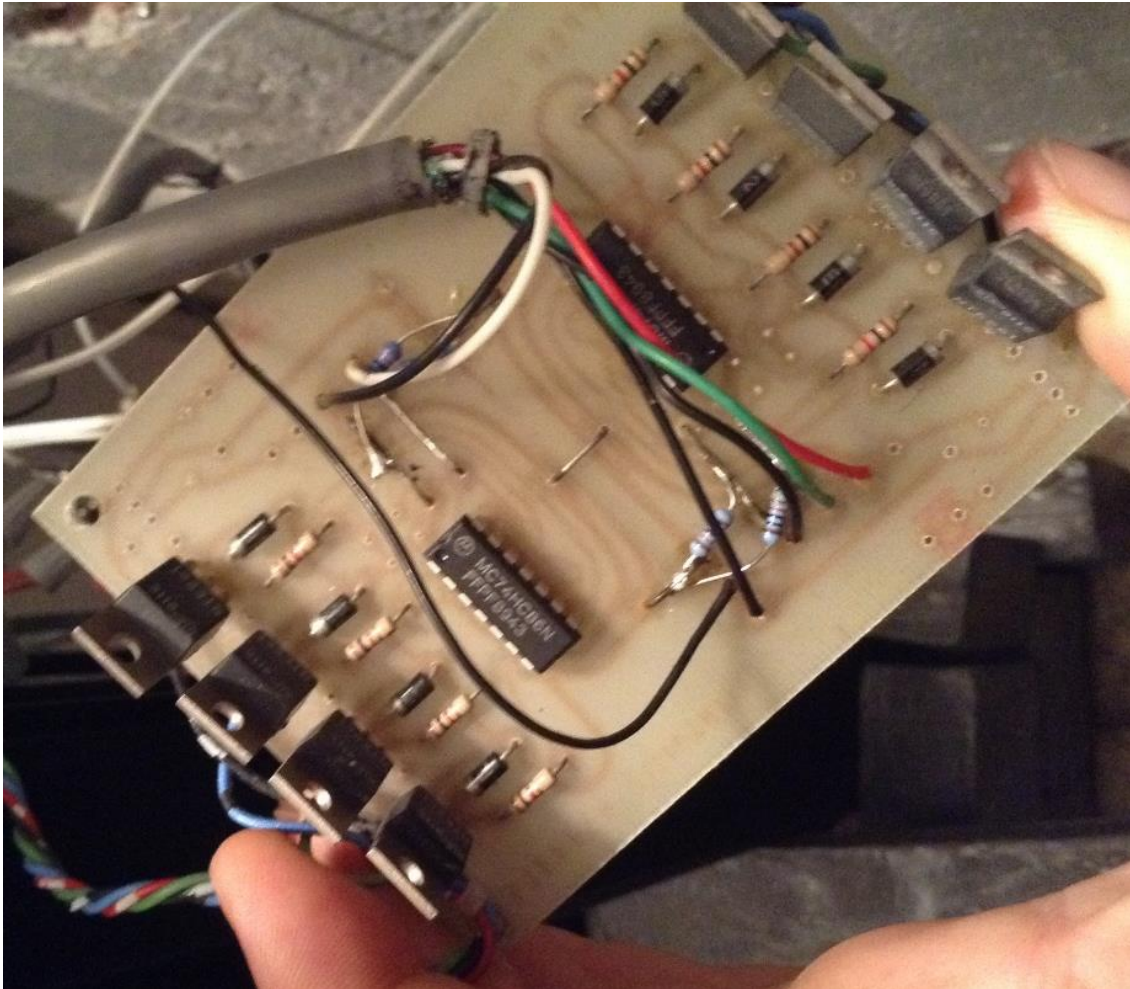


Figure 51. Stepper motor driver board and the added pull down resistors.

4.4.5. Collimator Positioning

Rotational positioning of the collimator is performed using a stepper motor and gear set attached to the outer circumference of the collimator holder. The stepper motor was an Oriental Motor PKP Series motor. The holder is held in place by a bracket with two precision bearings that provide low resistance rotation for the collimator tube. This setup allowed the rotational position of the collimator to be changed without personnel to enter the high radiation area of the radiography cave.

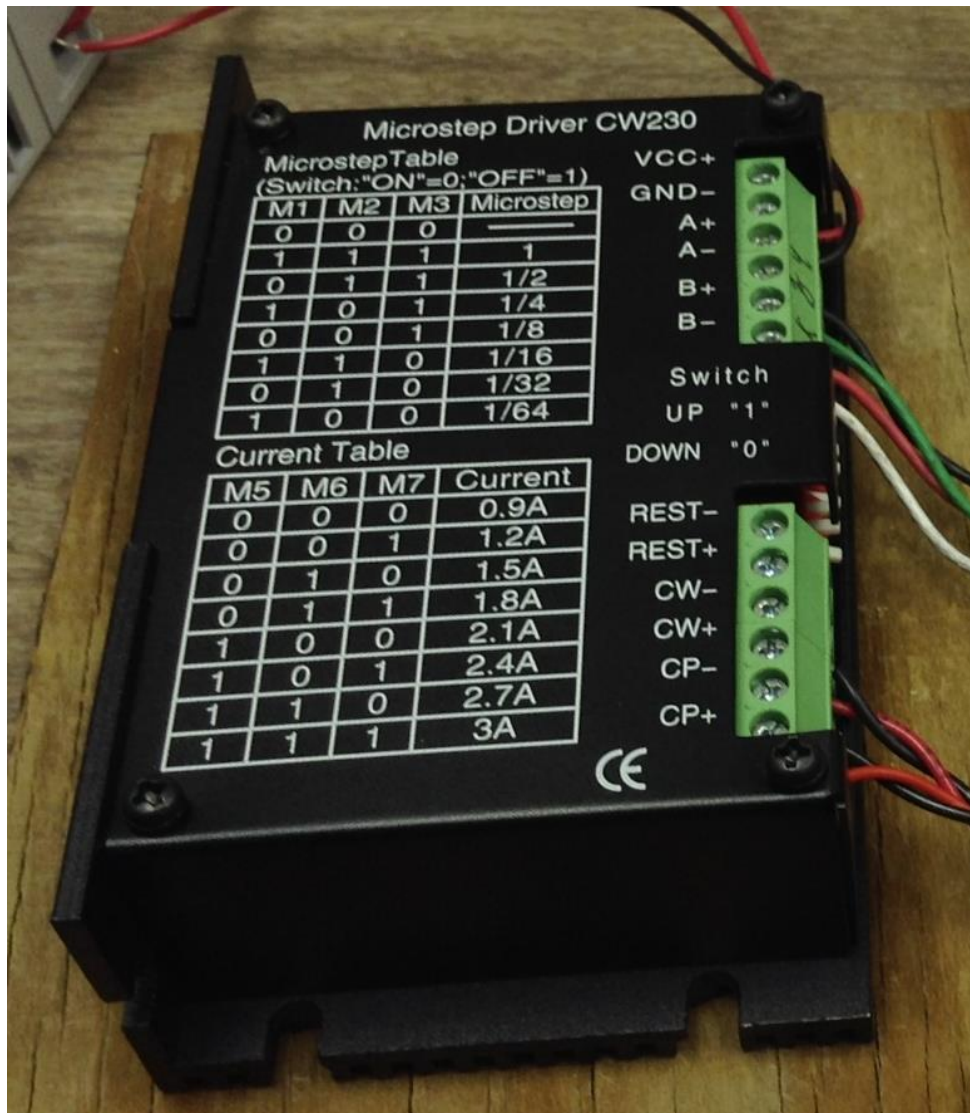


Figure 52. Micro-stepper driver for the collimator rotator. This driver is capable of 1/64th step sizes.

A few problems were encountered while attempting to integrate the collimator rotation system into the control board. It was discovered that the electrical current capabilities of the DIO were not sufficient to drive the input terminals of the stepper

motor driver. This was remedied using an operational amplifier, depicted in Figure 53, to boost the signal strength and allow the stepper motor driver to detect the signal pulses.

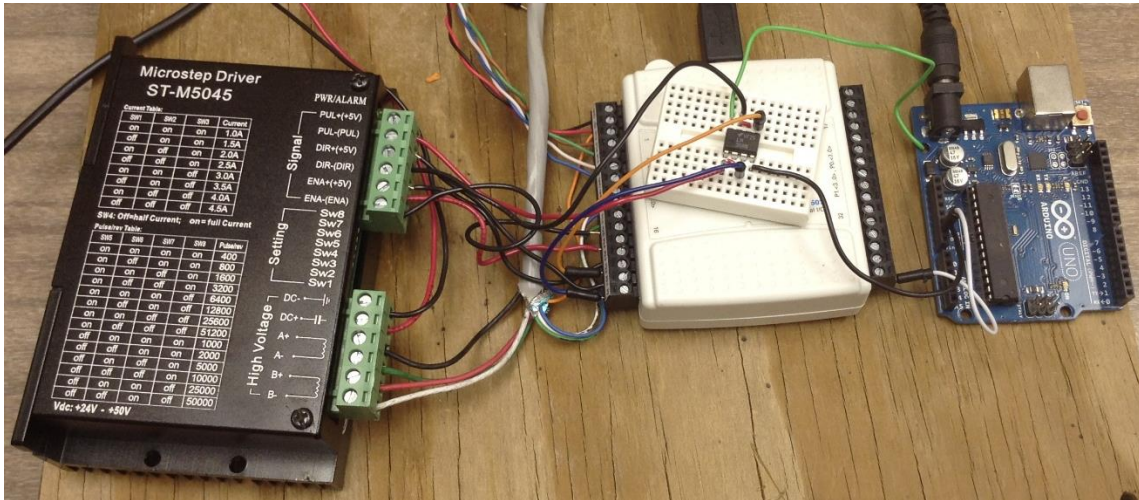


Figure 53. Left to right, the stepper motor driver, the NI USB DIO, and the Arduino board that was used as a power supply for the signal amplifier.

4.4.6. Camera and Lens

The image acquisition device used for the apparatus is a Santa Barbra Instrument Group (SBIG) STF-8300 astronomical camera. The lens is a Nikon AF-S Nikkor 70-200mm f/2.8 ED VR-II lens. A macro lens adapter was added to increase the effective focal length of the Nikon lens and increase the effective fill area of the image of the scintillator on the CCD imaging chip.



Figure 54. Nikon AF-S Nikkor 70-200mm f/2.8 ED VR-II lens.

4.4.7. Neutron Scintillation Screen

The neutron detection screens (NDS) are from Applied Scintillation Technologies. The NIS1 uses the 220 mm by 220 mm by 0.45 mm thickness scintillation screens, whereas the NIS2 uses the 60 mm by 60 mm by 0.25 mm thickness scintillation screens. Also available, but not in use are 460 mm by 460 mm by 0.45 mm thickness NDS that could be used in the future with the thermal column for wide area neutron-based NDT.

4.5. Neutron Beam Flux Measurements

It is important to know the neutron flux (beam brightness) and quality of the resulting beam to determine the approximate length of time required for the image acquisition process. Beam quality is determined by many factors, but it is relatively

simple to measure these defining quantities. The first determining factor is neutron beam luminosity (in the parlance of imaging, and neutron flux in the parlance of computation), second is beam divergence, and third is the Cadmium ratio (which is the ratio of thermal to epithermal neutron flux). The neutron absorption cross section of natural cadmium has the interesting characteristic of having what is effectively a thermal energy cut-off of 0.4eV, which provides a very simple analytical method to determine the Cd_{ratio} for any neutron beam, at any spatial point in its path [18]. The experimental technique that makes the feat possible is neutron activation analysis (NAA), which is a very powerful tool on its own in many different sciences.

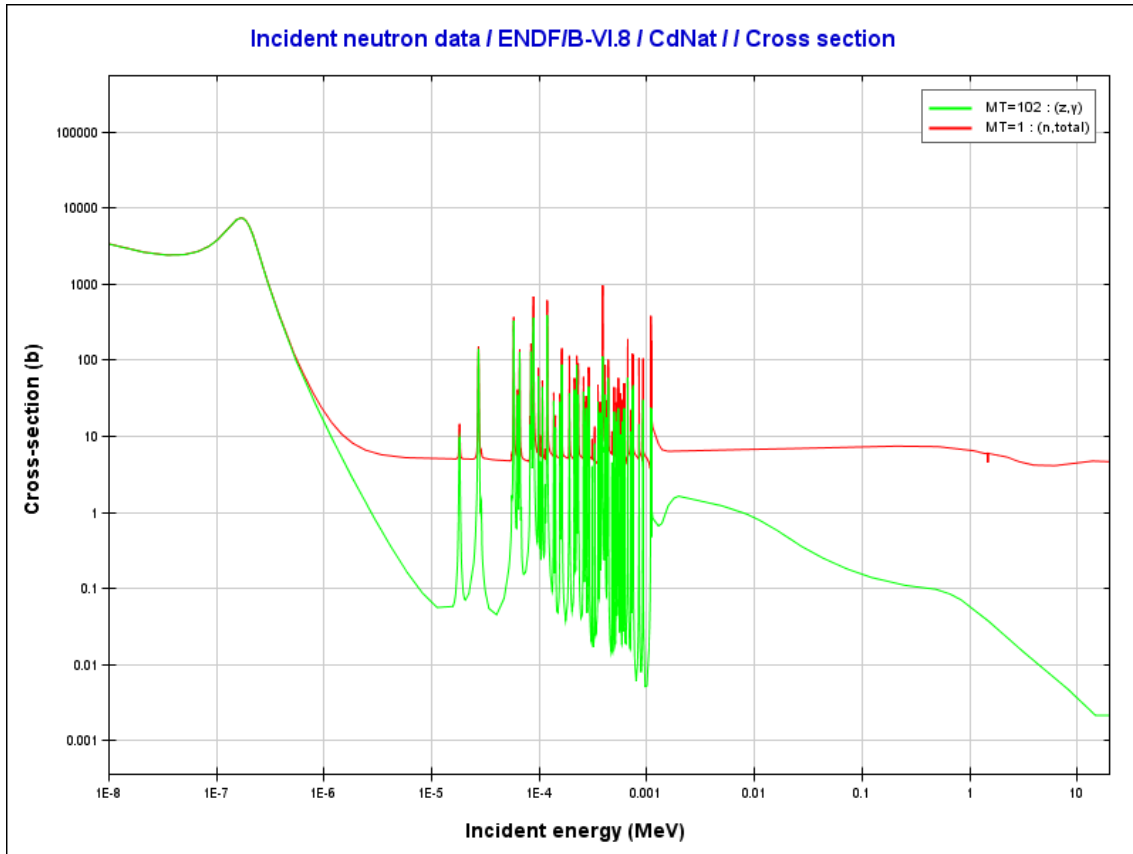


Figure 55. Total interaction cross-section and radiative capture cross-sections for natural cadmium [18].

The neutron flux determination will use neutron activation analysis on Au foils to measure the neutron flux at the opening of the beam port with the collimator installed. This information, along with the thick-beam source kernel, will be used to determine the neutron flux at any location along the beam line [54].

4.5.1. NAA Procedure

The maximum anticipated neutron flux, ϕ , inside the beam port area was estimated to be on the order of 1×10^8 n/cm². This assumption guided the decisions regarding irradiation, cooling, and counting times. Equation (45) relates the induced

activity to known quantities and the unknown quantity to determine the thermal flux using the gold foil activation method. R is the neutron capture reaction rate, V is the sample volume, m is the sample mass, and ρ is the sample density.

$$R = \phi \Sigma_{act} V = \frac{\phi \Sigma_{act} m}{\rho} \quad (45)$$

Equation (46) provides the definition for Σ_{act} for gold, where I_0 is the absorption resonance integral and σ_0 is the thermal absorption cross section.

$$\Sigma_{act} = \begin{cases} I_0, & \text{with Cd cover} \\ \sigma_0 + I_0, & \text{without Cd cover} \end{cases} \quad (46)$$

The spectral content of the measured beam flux is determined by the Cd cover. Analysis of the results with and without the Cd cover allows the two group neutron flux to be determined. The differential equation that describes the mathematical relationship between radioactive decay over time, t , the decay constant, λ , and the number of radioactive atoms, N , left in the sample is given in equation (47).

$$\frac{dN}{dt} = R - \lambda N \quad (47)$$

Solution of equation (47) given the boundary conditions of zero initial activity, A , and a constant neutron flux yields equation (48).

$$A(t) = R(1 - e^{-\lambda t}) \quad (48)$$

The saturation condition refers to the equilibrium between the buildup of radioactive atoms and the decay of these atoms. Saturation implies equation (49).

$$\frac{dN}{dt} = 0 \quad (49)$$

Therefore, the flux can be calculated from the measured activity of the radioactive sample. Irradiation times of three to four half-lives are required to bring the activity level to within 6% to 12% of the saturation activity, A_∞ , level.

$$A_\infty = R = \frac{\phi \Sigma_{act} m}{\rho} \quad (50)$$

This can be impractical if the reactor steady-state power time is short compared to the half-life. Hence, it is necessary to extrapolate to the saturation activity.

$$A_0 = A_\infty(1 - e^{-\lambda t_0}) \quad (51)$$

The high purity germanium (HPGe) gamma-ray spectrometer available at the NSC is calibrated for detector efficiency and background radiation; it then uses internal algorithms and gamma-ray energy discrimination to calculate the total activity of a sample as the output. Since the counting time is very small when compared to the half-life of radioactive gold foil, the measurement can be assumed to be instantaneous. Therefore, it is simple to calculate, retroactively, the activity of the sample at the moment the neutron beam was turned off using equation (52).

$$A_1 = A_0 e^{-\lambda(t_1-t_0)} \quad (52)$$

The saturation activity would therefore be given by equation (53).

$$A_\infty = \frac{A_1}{(1 - e^{-\lambda t_0}) e^{-\lambda(t_1-t_0)}} \quad (53)$$

The saturation activity now gives us the ability to determine the energy-integrated flux in the neutron beam [54]. The neutron flux can then be calculated using equation (54).

$$\phi = \frac{A_1}{(1 - e^{-\lambda t_0}) e^{-\lambda(t_1-t_0)}} \cdot \frac{\rho}{\Sigma_{act} m} \quad (54)$$

The process of buildup and decay of radioisotopes would look similar to Figure 56. This sketch is a representative profile for activation analysis with decay constant of 0.01 s^{-1} and an irradiation time that is on the order of the half-life.

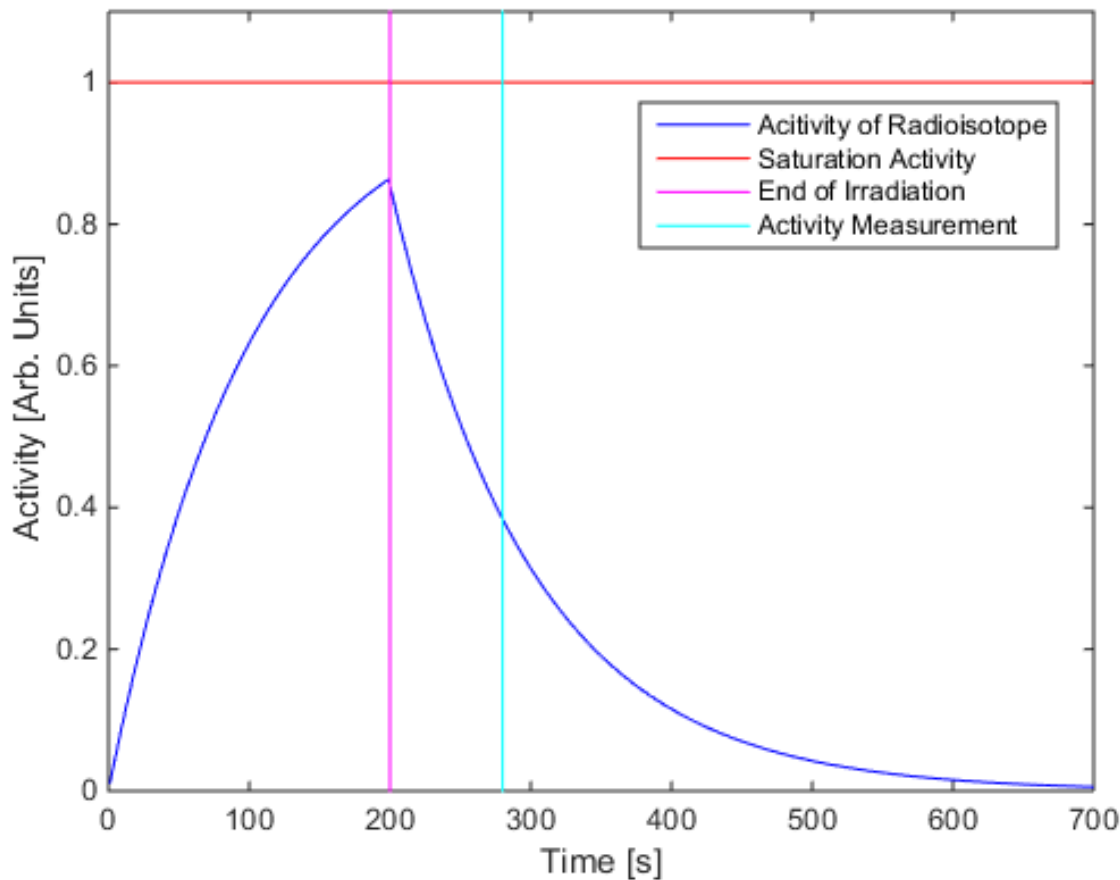


Figure 56. Radioisotope buildup and decay curve.

The activity was determined using the high purity germanium (HPGe) detector in the counting lab at the NSC. The Genie software that comes with the HPGe detectors uses calibrated data sets, sample holders, and object mass to calculate the activity. It has a complete radioisotope data library to apply branching ratios and statistical analysis to

minimize the standard error that would be encountered when performing hand calculations of the activity from a gross counts type of detector. The accepted values of the interaction cross sections are given in Table 3 [55].

Table 3 Gold Neutron Absorption Cross-Section Values

Variable	Cross-section [b]
σ_0	98.65±0.09
I_0	1597±67

4.5.1.1. Foil Placement and Pre-irradiation Mass Measurement

The foil masses were measured with a Mettler AE100 as shown in Figure 57. Gloves were used to prevent potential contamination of the Au foil with salt from finger prints and subsequent unanticipated activation products. A piece of wax paper was used to prevent any material on the scale from transferring to the Au foil and simplify handling. The foil in Figure 57 is the leftover Au foil and was measured for inventory control after the foil was parsed into four roughly equal masses.



Figure 57. Mass measurement scale.

The bare foils were covered in aluminum foil to provide a barrier between the environment and ease handling. These samples were then attached to sample holder using Kapton™ tape. Figure 58 is a detailed section of the lateral placement of the activation foils for both axial positions.

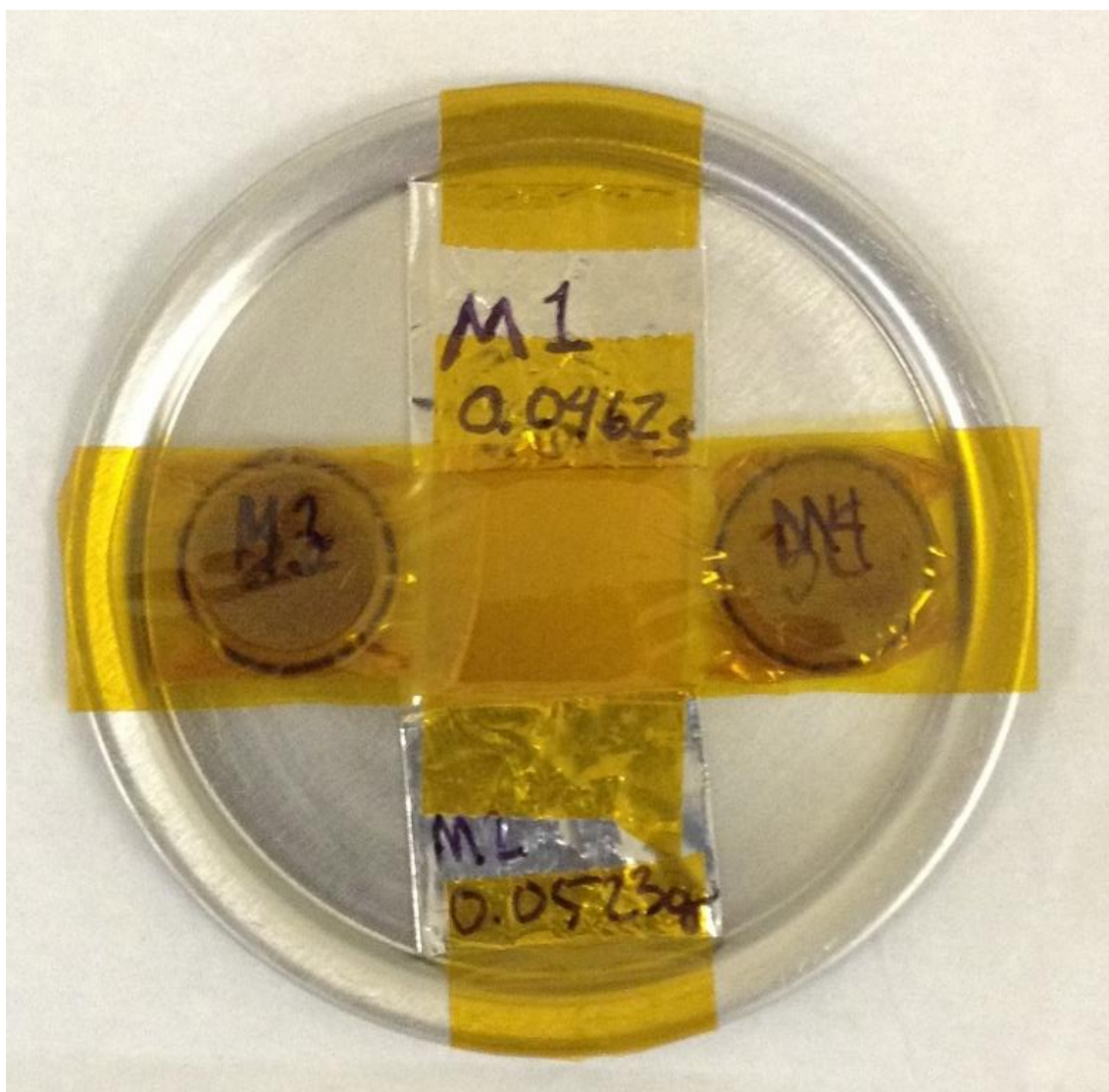


Figure 58. Detail of placement of the activation foils on the sample holder.

The foil holder was placed in the location shown in Figure 59. This location was chosen to be representative of the output flux of the beam line.

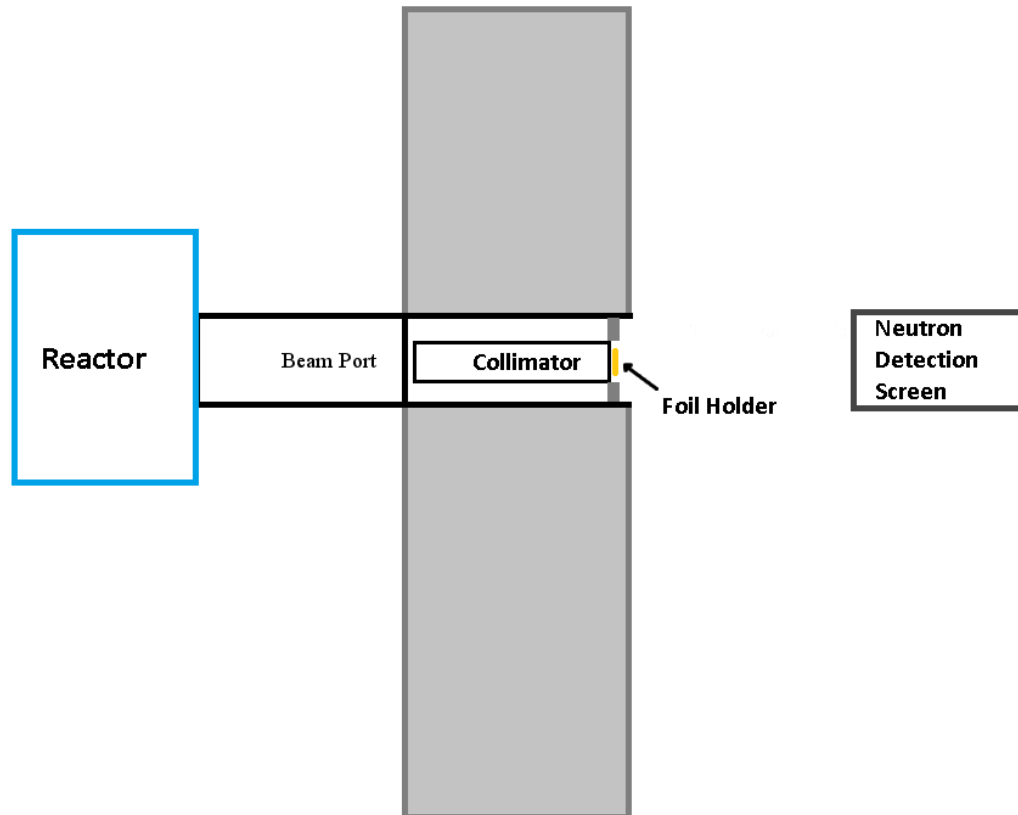


Figure 59. Location of the Au foils in the beam port.

4.5.2. Measurements for Flux Determination

The thermal and epithermal flux values were determined by averaging the calculated flux values for each data point. It was assumed that the fast flux would be negligible. The calculated fluxes and uncertainties are given in Table 5. The Au foil masses and post irradiation activities for each sample are recorded in Table 4. Foils 3 and 4 were placed inside Cd covers to remove the thermal neutron flux component.

Table 4 Measured Values for Neutron Flux Determination

Sample Designation	Gold Foil Mass [g]	Activity [μCi]	Mean Activity Uncertainty [μCi]
M1	0.0462 \pm 0.00005	3.272	0.0888
M2	0.0523 \pm 0.00005	3.328	0.0903
M3+Cd	0.0424 \pm 0.00005	0.542	0.0153
M4+Cd	0.0506 \pm 0.00005	0.589	0.0165

The uncertainty in the neutron flux was determined using the estimated uncertainty in foil sample mass, sample activity, and the uncertainty of the neutron absorption cross section. Uncertainty in the radioactive half-life, density of Au, and measurement times were not used. The general form of uncertainty estimation is given in equation (55) [56].

$$\delta\phi = \sqrt{\left(\frac{\partial\phi}{\partial A}\right)^2 (\delta A)^2 + \left(\frac{\partial\phi}{\partial \Sigma_{act}}\right)^2 (\delta \Sigma_{act})^2 + \left(\frac{\partial\phi}{\partial m}\right)^2 (\delta m)^2} \quad (55)$$

Table 5 Neutron Flux Values

Total Flux [n/cm^2]	Epithermal Flux [n/cm^2]	Thermal Flux [n/cm^2]
6.24 x 10 ⁵ \pm 2.46 x 10 ⁴	1.20 x 10 ⁵ \pm 5.02 x 10 ³	5.04 x 10 ⁵ \pm 1.48 x 10 ⁴

4.5.3. Cadmium Ratio

The Cd_{ratio} is a simple measurement of the neutron beam quality. It is simply the ratio of the measured flux for the uncovered Au foil to the measured flux of the Cd

covered foil. With the previous measurements of these quantities, it is a straitforward calculation to determine the Cd_{ratio} given in equation (56).

$$Cd_{ratio} = \frac{A_{bare}}{A_{Cd}} = 5.8 \quad (56)$$

The Cd_{ratio} for the NSC beam port 4 neutron beam line with Collimator B is 5.8. This represents a very low ratio for thermal neutron imaging applications and might be better classified as an epithermal beam. The historical Cd_{ratio} for beam port 4, which used a typical aperture-style collimator, was 100 [4](citation confirmation needed).

4.6. Neutron Image Data

The neutron images were acquired using the NIS2 described previously in section 4.3.3 and the brightness-adjusted raw images are given in Figure 60 and Figure 61. Samples of these images are given in Figure 60 and Figure 61; notice the relatively large amount of noise still present in the image before the images were filtered using the adaptive Weiner filter.

Image 1

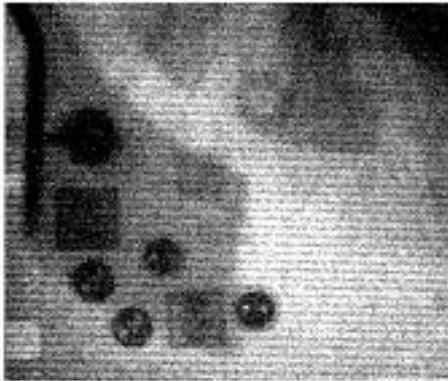


Image 2

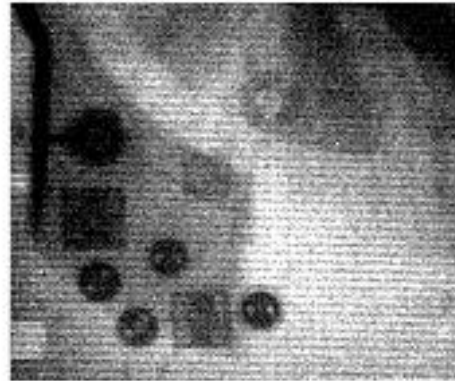


Image 3

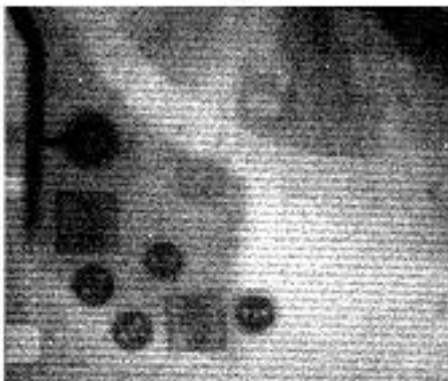


Image 4

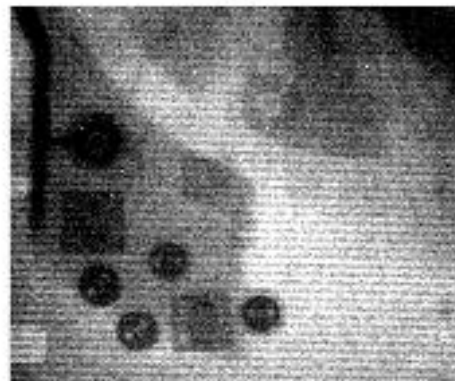


Figure 60. Unfiltered images with the collimator in the horizontal orientation.

Image 5

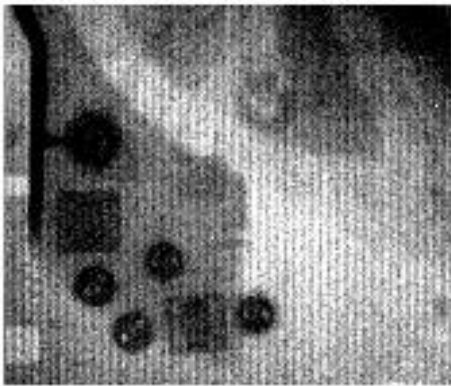


Image 6

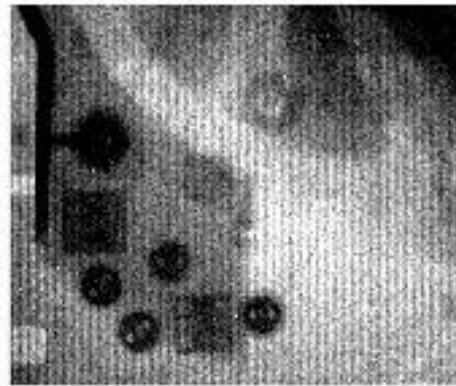


Image 7



Image 8

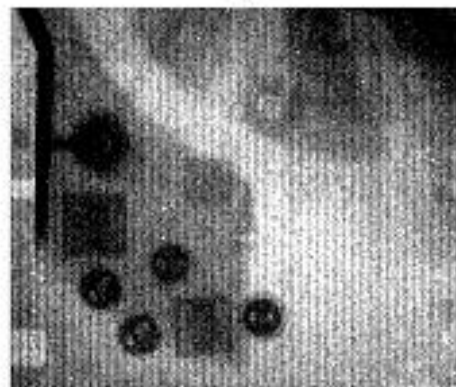


Figure 61. Unfiltered images with the collimator in the vertical orientation.

5. RESULTS AND DISCUSSION

A total of eight images were acquired; four images were taken with the neutron collimator in the horizontal orientation and four in the vertical orientation. These images were then digitally processed to remove radiation induced and thermal noise.

5.1. Preprocessing

The raw images displayed the typical characteristics of images taken within a radiation field; namely, the images had large amounts of radiation induced noise from gamma-rays and neutrons, which gave the images a “snowy” appearance. This noise was removed in ImageJ by using the “Remove Noise Outliers” feature with the settings given in Table 6.

Table 6 Outlier Filter Values

Property	Value
Filter Radius	4 pixels
Threshold	100
Pixel Feature	Bright spots

The images were then adjusted for proper brightness and contrast such that the images would be visible. The histogram was then renormalized and equalized for each image due to the fact that the data range was for 16 bit format images (0 to 65535), but the brightest parts of the image never exceeded 3000. The range was renormalized to the median of the image data sets with a standard deviation of ± 10 sigma.

The random CCD noise was filtered using a 5 by 5 filter that used the adaptive Weiner technique. The results of this filtering technique are shown in Figure 62 and Figure 63.

Issues were encountered during the image normalization process in that the images with the collimator oriented in the horizontal direction displayed more variance and needed more attention for proper normalization. The original method relied on MatLab's native scaling feature built into the function `mat2gray`. To display the issue in a concise manner, one row and one column of pixels were chosen and plotted on the same figure. The resulting four figures were then compared in a composite figure.

Image 1

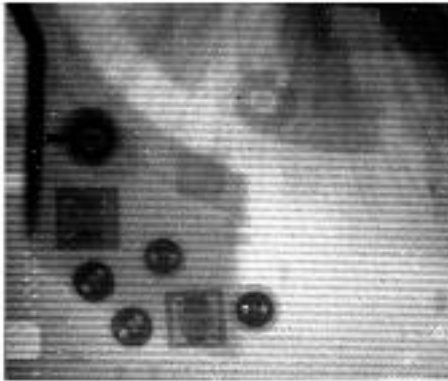


Image 2

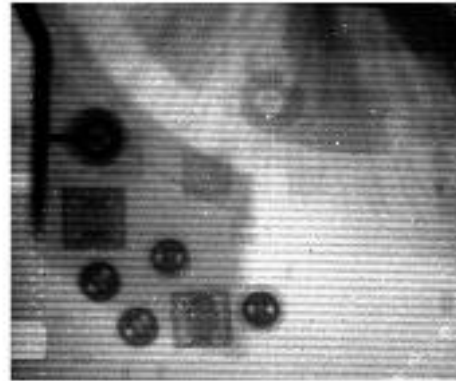


Image 3

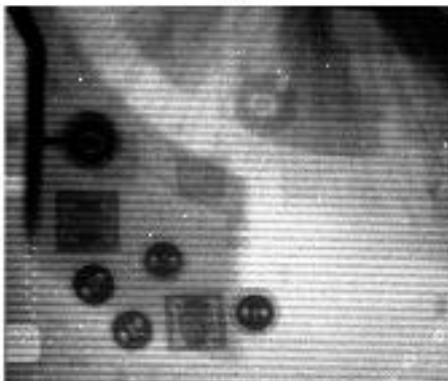


Image 4

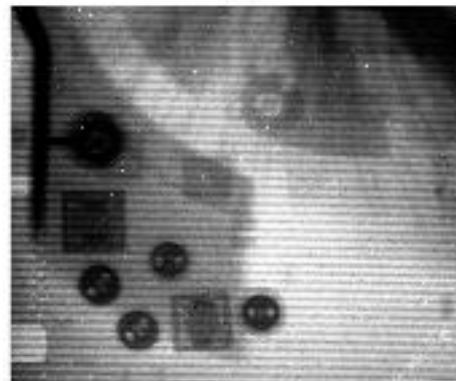


Figure 62. Filtered images with the collimator in the horizontal orientation.

Image 5

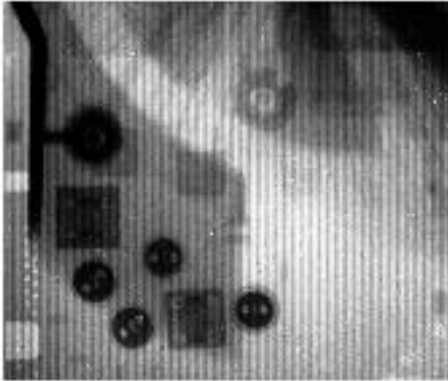


Image 6

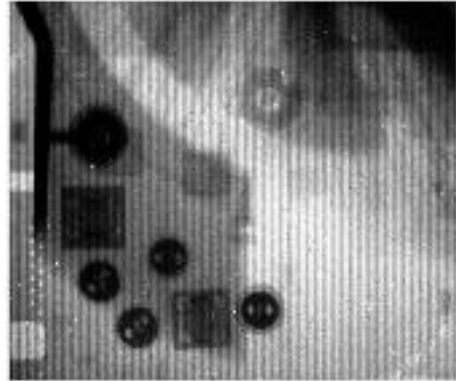


Image 7

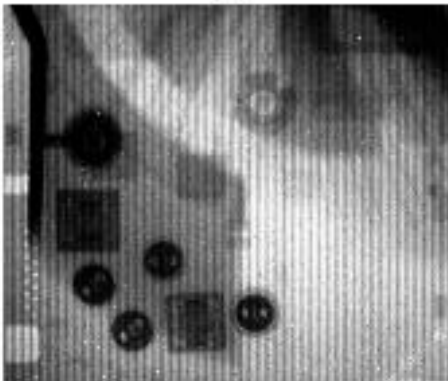


Image 8

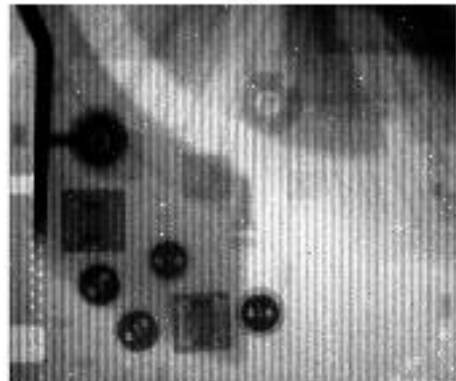


Figure 63. Filtered images with the collimator in the vertical orientation.

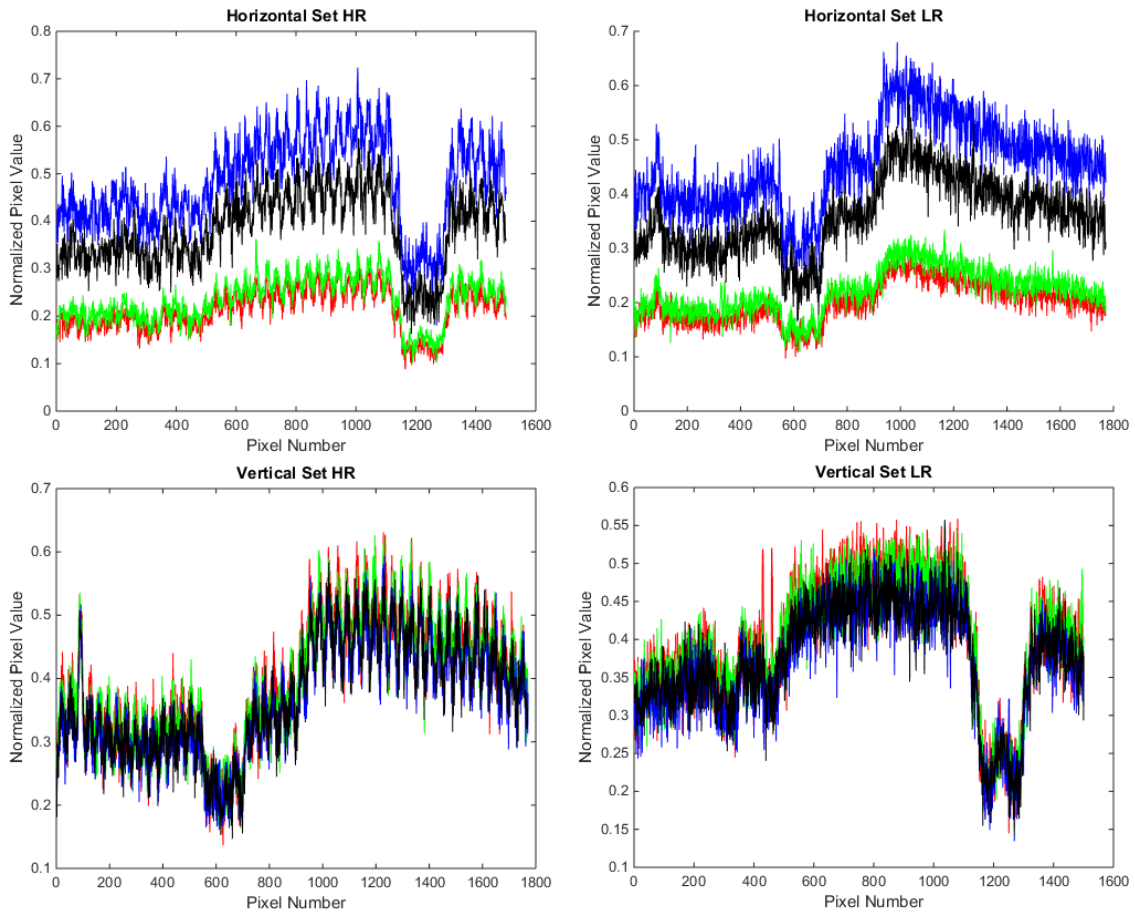


Figure 64. Unfiltered and unnormalized signals.

A more rigorous normalization method was used to scale the data using the mean and standard deviation of each piece of data. The data were scaled to the range of $[0, 1]$, with the minimum being 15 standard deviations less than the mean and the maximum being 15 more than the mean. In addition to the scaling, the thermal noise was reduced using the adaptive filter function “wiener2” with a 5 by 5 filter size. This resulted in a cleaner data set; an example of a single line of pixels from the image data set is given in Figure 65.

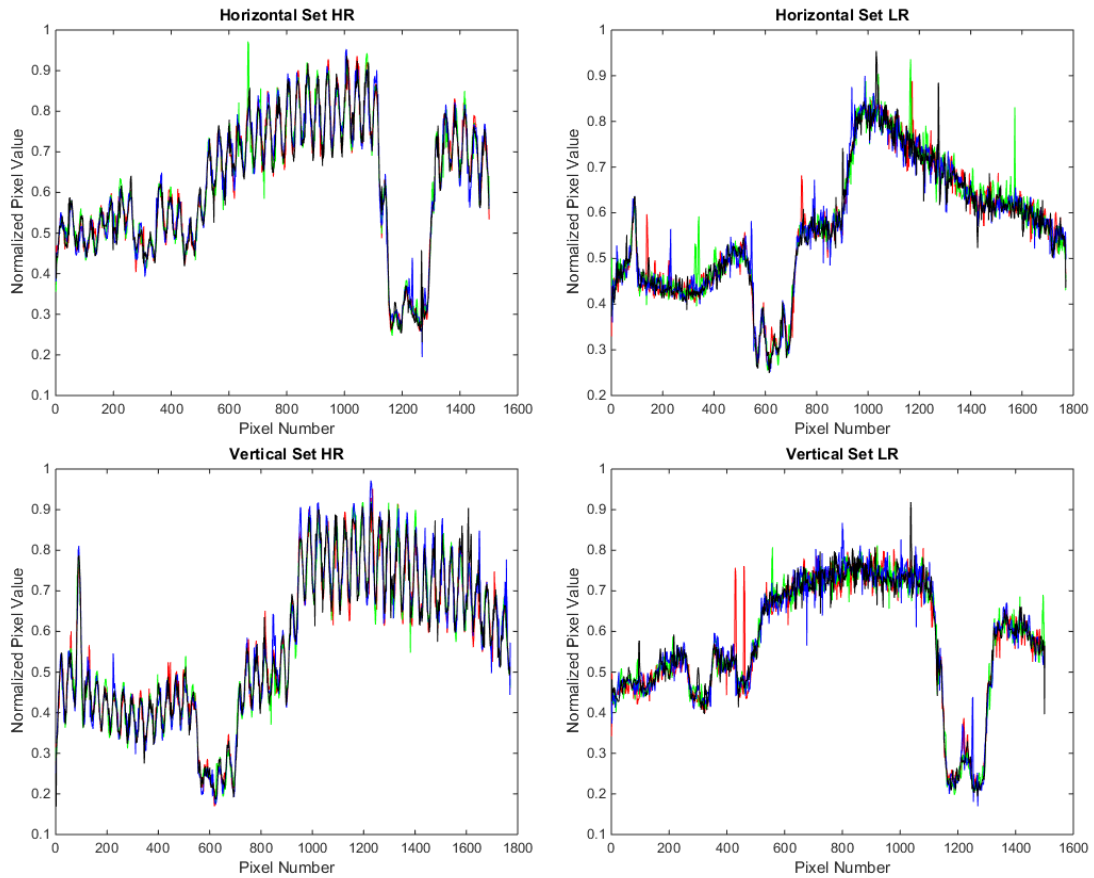


Figure 65. Filtered and normalized signals.

5.2. Simple Linear Combination

As one can see from Figure 66, the simple linear combination of horizontal and vertical images is not sufficient to render the higher precision that is afforded by the high aspect ratio neutron collimator. This linear approximation was used as the baseline from which to judge the improvement in human readability.

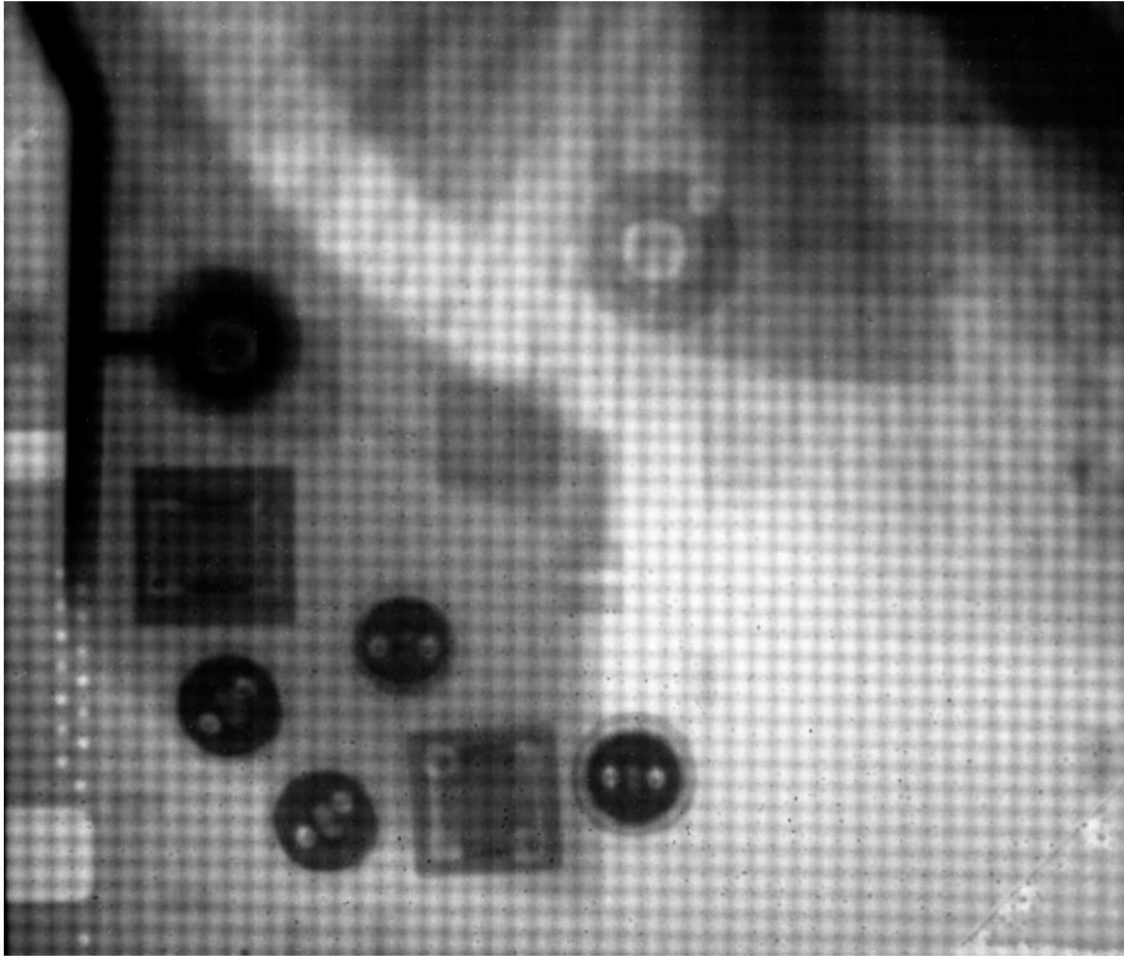


Figure 66. Simple linear average of neutron images.

5.3. Discrete Wavelet Transformation

The discrete wavelet transform has the capability to either enhance the fine detail or remove image artifacts. The difference between the simple linear combination and the 2D-DWT method is the utilization of the high frequency detail in conjunction with the low frequency approximation.

5.3.1. One-level DWT

The image in Figure 67 uses the Daubechies 20 wavelet with the image decomposed one level. The Daubechies 20 wavelet was chosen as the example for this reconstruction because it produced the sharpest edges. This results in a coarse image reconstruction and is not adequate for image enhancement that improves human readability.

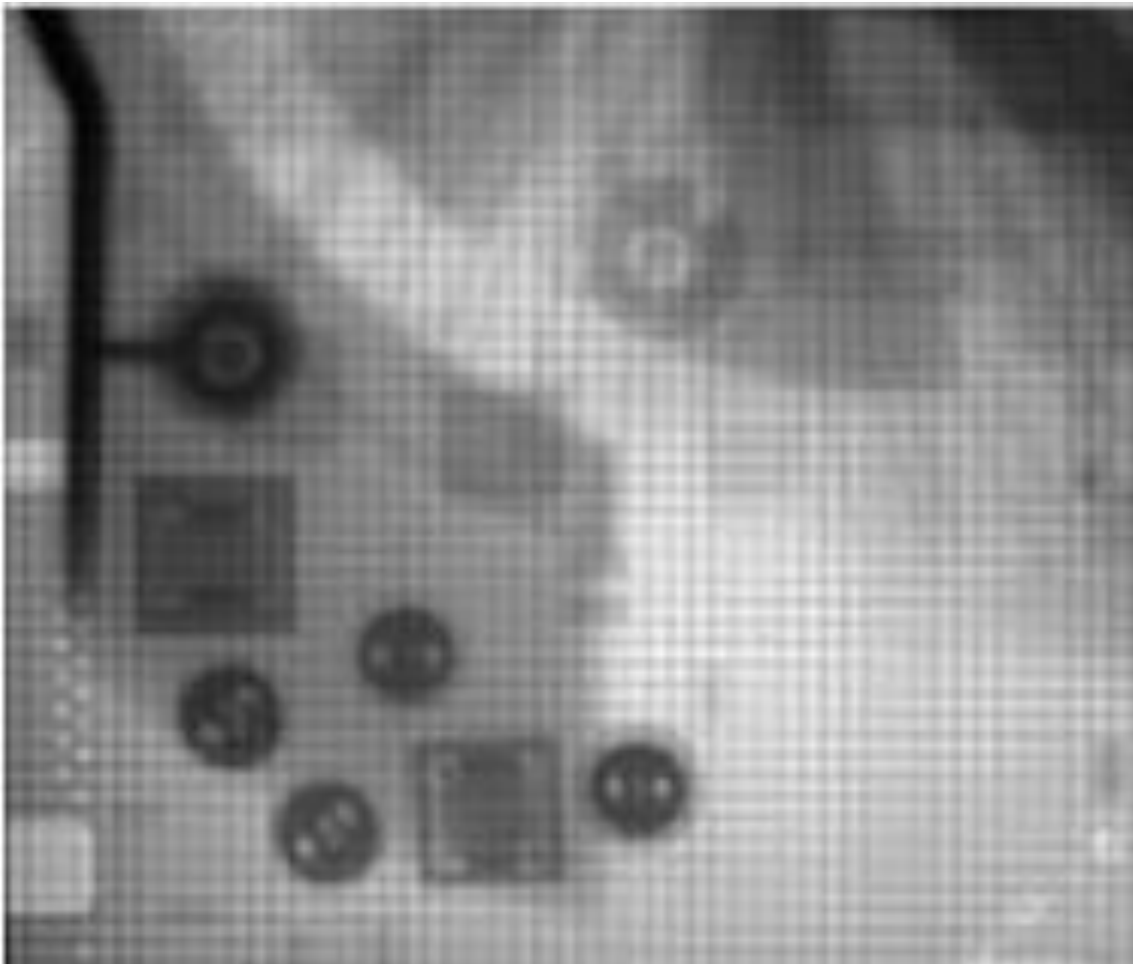


Figure 67. Daubechies 20, one-level wavelet decomposition.

5.3.2. *Cauchy Distribution and One-level DWT*

The Cauchy distribution was used to estimate the most likely image approximation. The argument maximum was then determined using the previous derived method; the argument maximum was then used as the reconstruction approximation value.

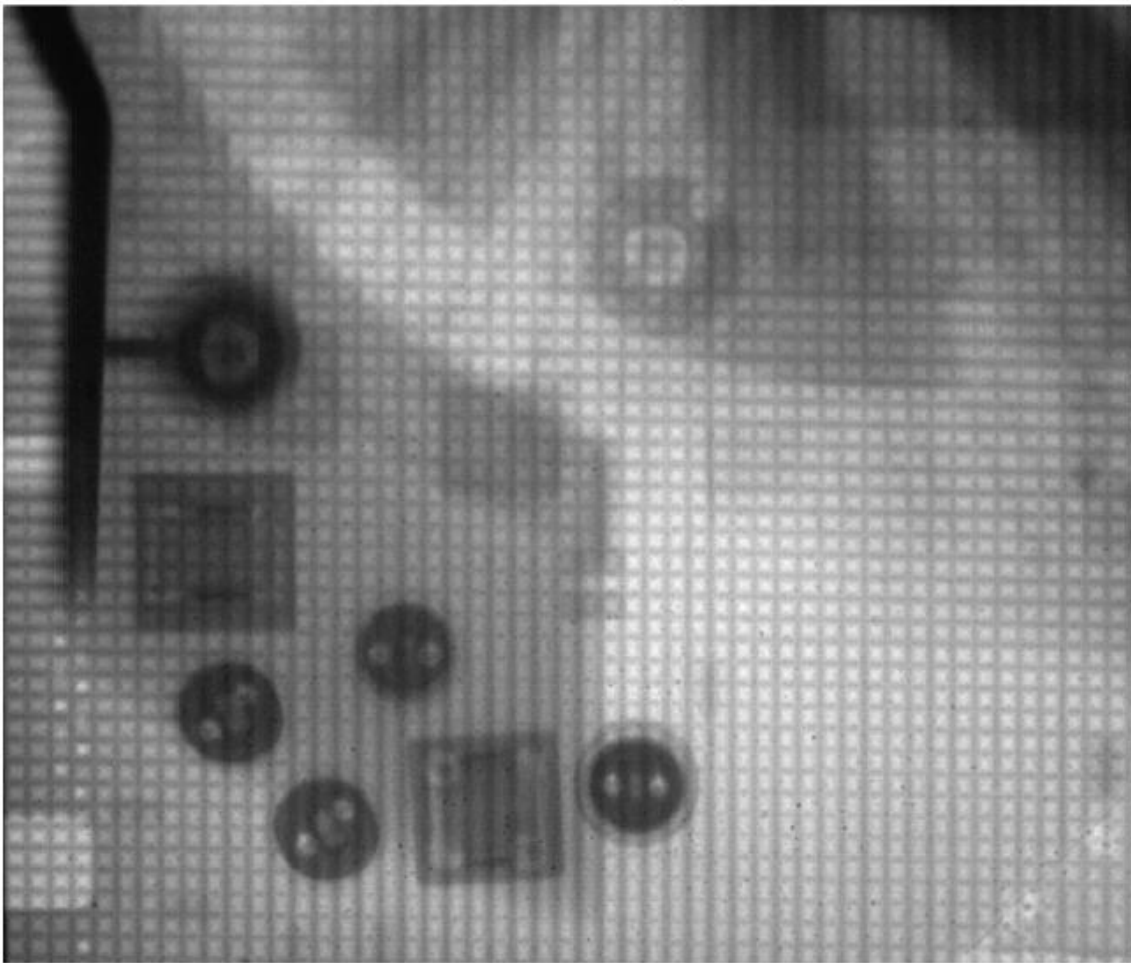


Figure 68. Cauchy distribution Bayesian method.

5.3.3. *Multilevel DWT Artifact Rejection*

The multilevel artifact rejection method begins by reducing the image set down to the maximum decomposition level, which corresponds to the maximum similarity between images. The LR approximations are then used in the reconstruction process in lieu of the HR details.

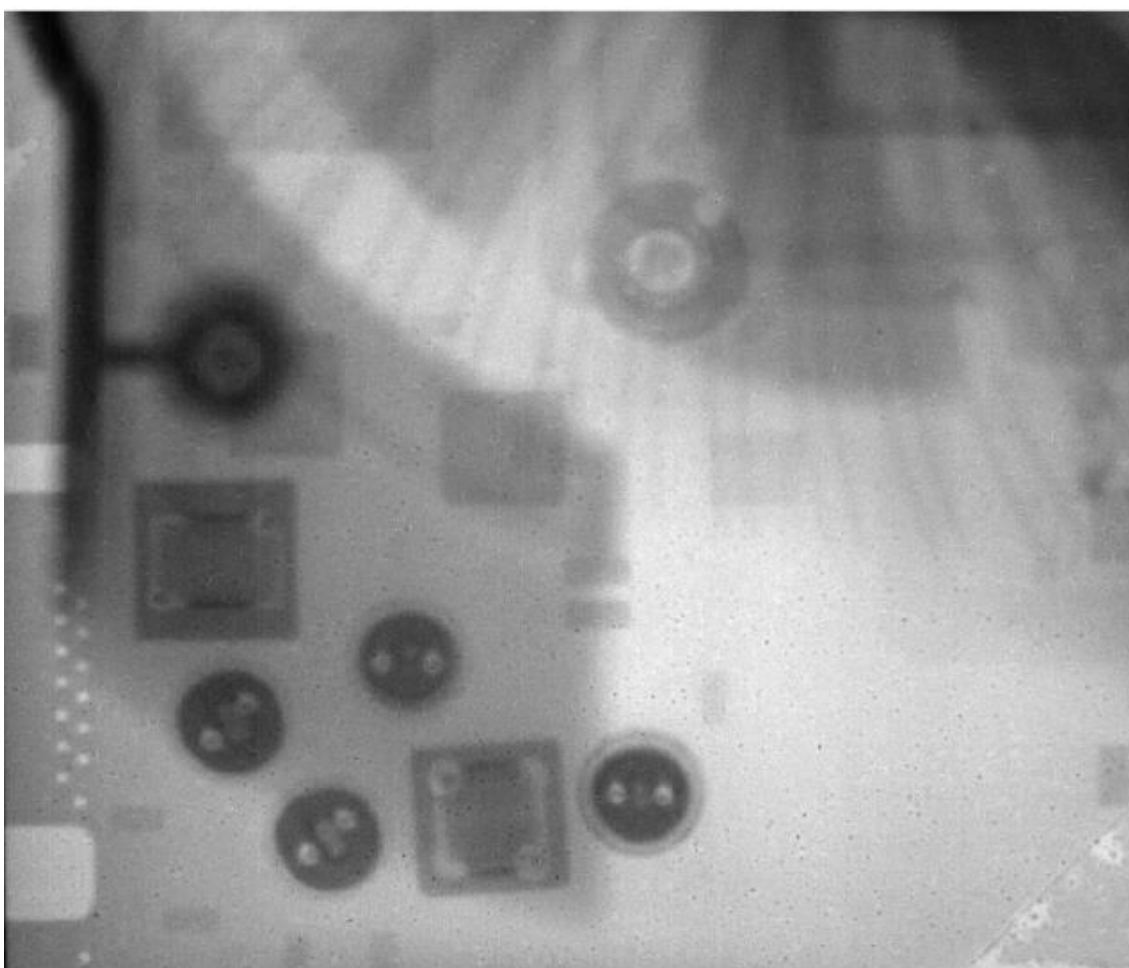


Figure 69. Daubechies 8 wavelet method

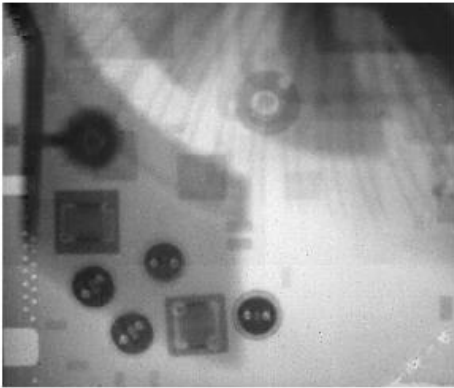
5.3.4. Multilevel DWT Artifact Rejection Wavelet Sensitivity

The choice of wavelet dramatically impacts the reconstruction process. This is most apparent in the artifact rejection mode illustrated in Figure 70. The more complex wavelets (higher Daubechies wavelet number) capture more detail in each LR approximation. As the chosen wavelet used in the reconstruction becomes more complex, the artifact rejection method and edge enhancement method approach each other asymptotically. What is also apparent (but not obvious) is that the features of artifact rejection reconstruction and edge enhancement could be combined/traded at different decomposition levels to achieve a more optimum result.

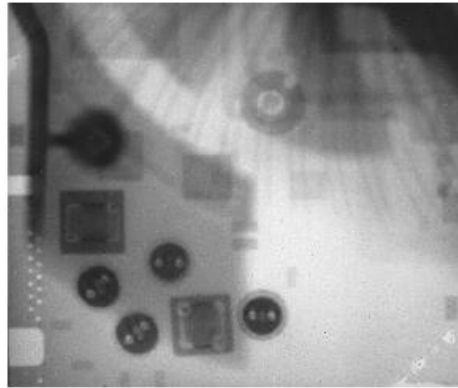
5.3.5. Multilevel DWT Edge Enhancement

The edge enhancement DWT technique uses the high spatial frequency detail from the corresponding image set to form the singular high detail image. Spatial high frequencies are indicative of large step changes in image intensity values and represent the interpretation of an edge. This result is shown in Figure 71.

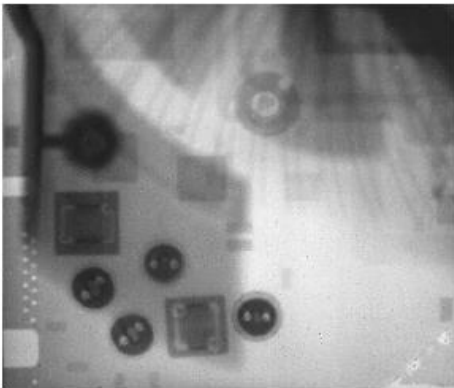
Haar



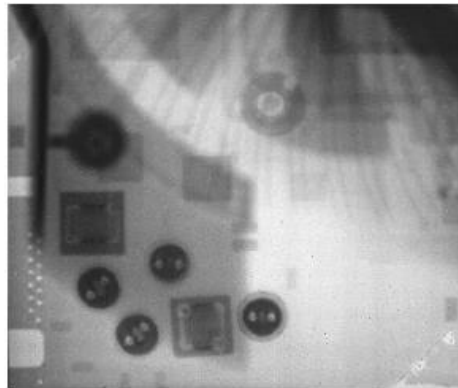
Daubechies 4



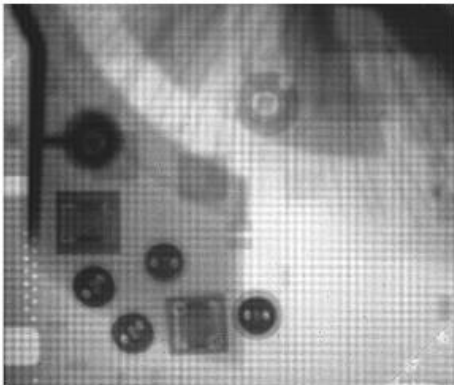
Daubechies 8



Daubechies 16



Daubechies 24



Daubechies 32

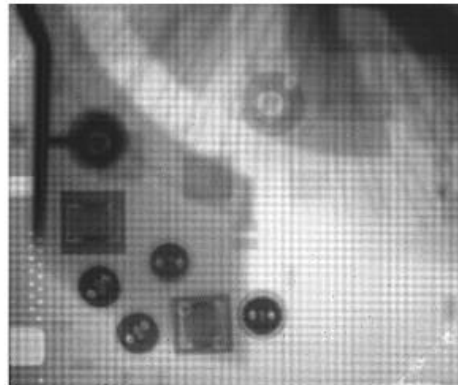


Figure 70. Artifact rejection wavelet sensitivity.

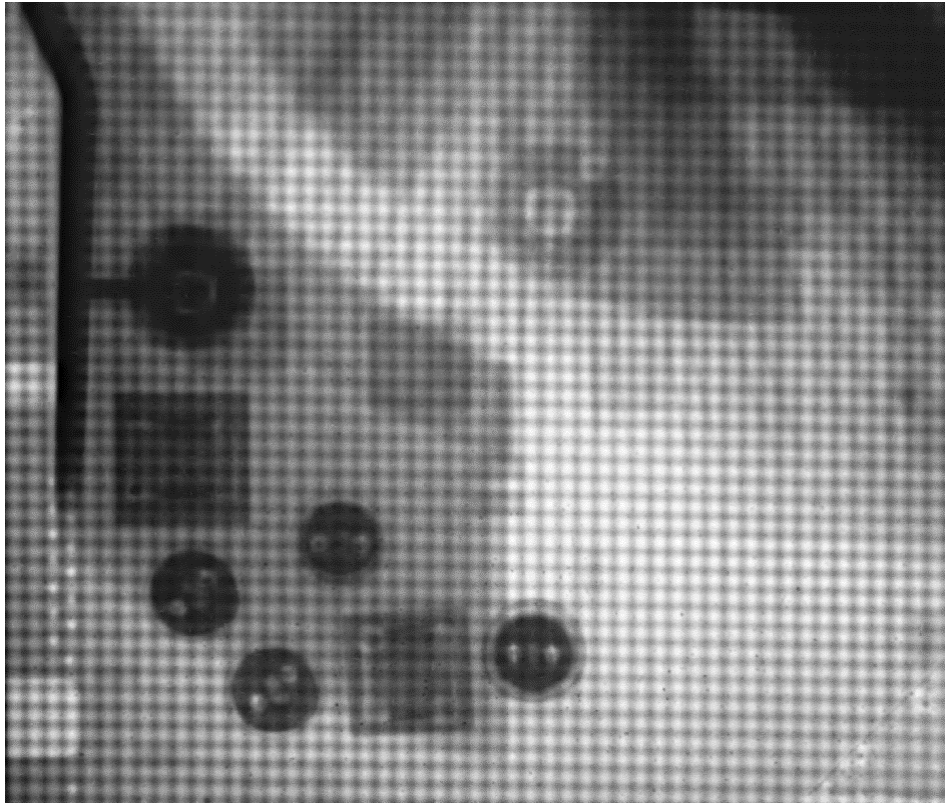
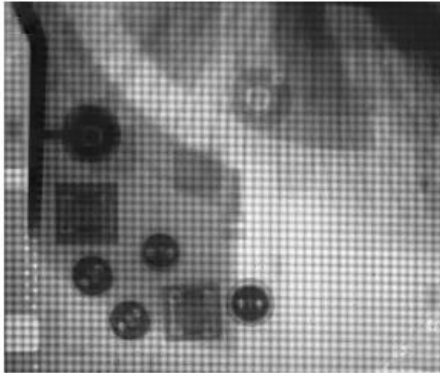


Figure 71. Edge enhancement using Daubechies 8 wavelet method.

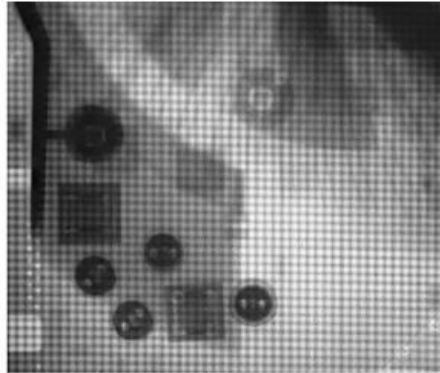
5.3.6. Multilevel DWT Edge Enhancement Wavelet Sensitivity

A sensitivity analysis was performed to determine the optimum wavelet decomposition level for the neutron images. As the wavelet becomes more complex (a higher Daubechies number), fewer decompositions can be made before there is not insufficient information left to decompose and the maximum level is reached. This results in additional image artifacts in which the more complex wavelets appear to imprint a sinusoidal intensity variation near strong edges in the data. This sensitivity analysis is graphically depicted in Figure 72. The “best” reconstruction would be interpreted to be the reconstruction that produced the sharpest rise in image intensity values along a specific edge.

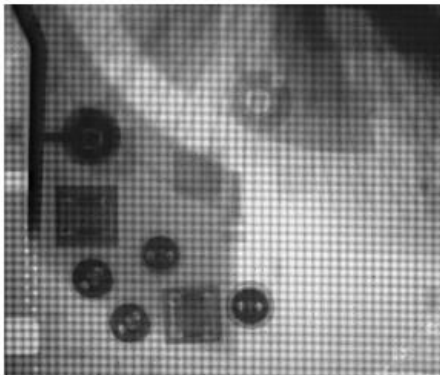
Haar



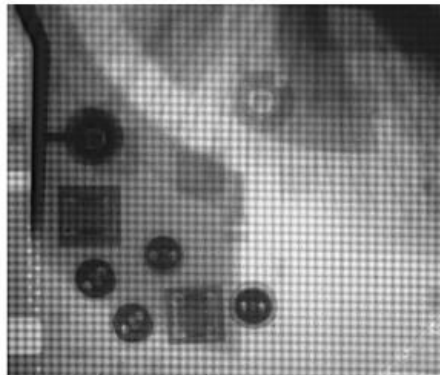
Daubechies 4



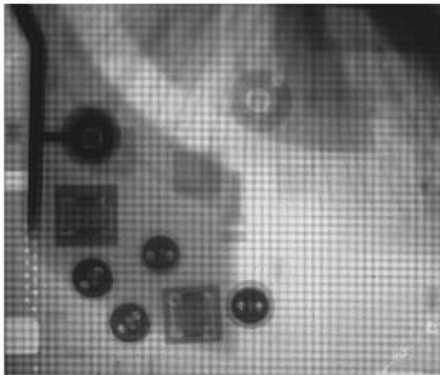
Daubechies 8



Daubechies 16



Daubechies 24



Daubechies 32

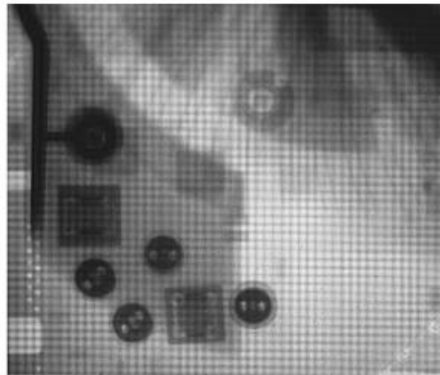


Figure 72. Sensitivity of image reconstruction to Wavelet complexity.

5.4. Data Analysis Summary

The simplest wavelet results in a tile-like image artifact due to the wavelet not being complex enough to capture sufficient detail at the highest level of similarity (the lowest decomposition level). It therefore becomes clear that there is an optimum somewhere in the middle of the wavelet complexity spectrum.

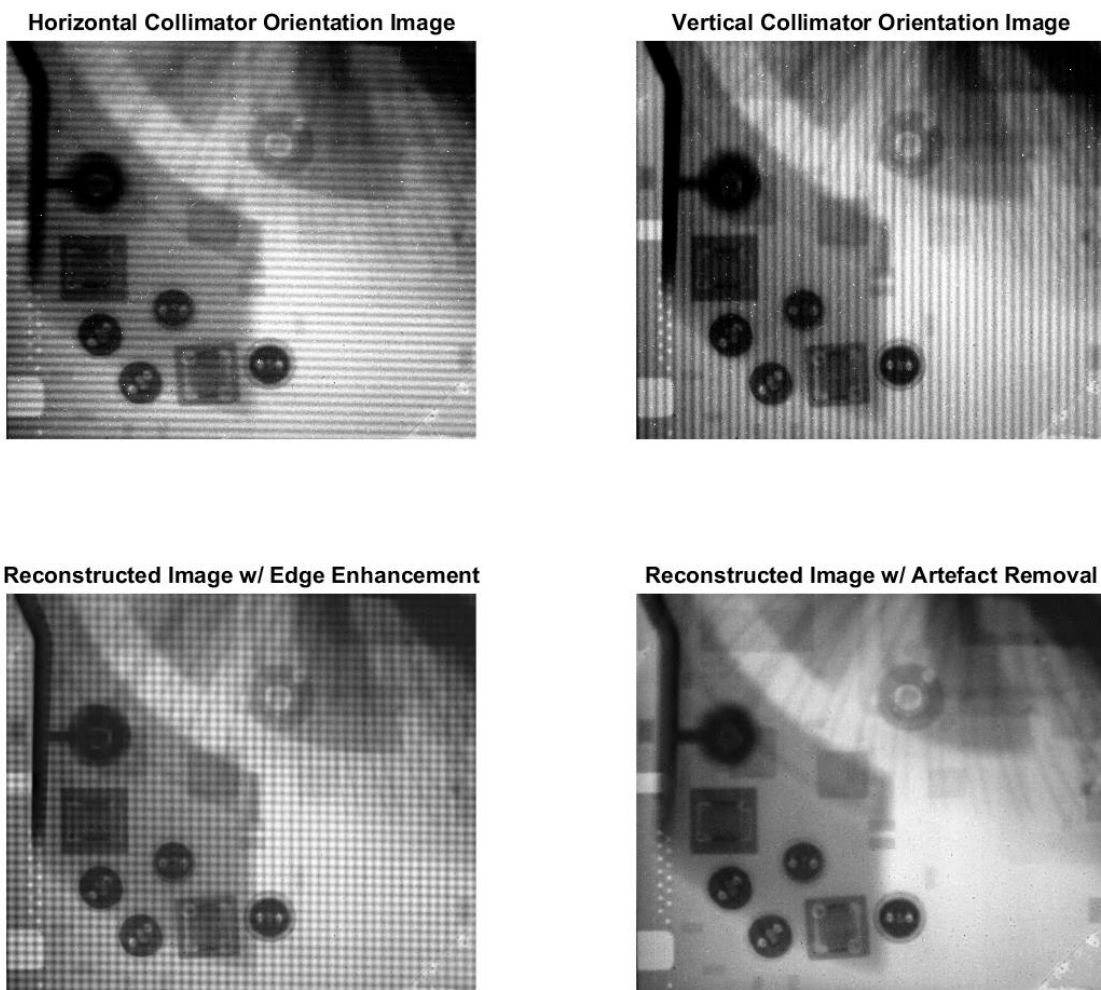


Figure 73. Comparison of images before reconstruction and post reconstruction structures.

The results shown in Figure 73 demonstrate the effectiveness of the DWT methods in extracting the required orthogonal information from the image dataset. The edge enhancement techniques require image preprocessing that involves the open field image to remove the banded artifacts from the dataset. This was impractical due to the time considerations and issues with mechanical backlash in the collimator gear rotation mechanism. It became exceedingly difficult to reproduce the exact same banded illumination pattern consistently; therefore this technique of image normalization was left out of this analysis.

The DWT method has also been shown to be capable of removing the same banded artifacts by excluding the specific data that contained them while seamlessly replacing that information with data that did not contain the artifacts. The applications of DWT methods are growing constantly.

6. CONCLUSIONS AND FUTURE WORK

The outcome of this dissertation was a success: the fusion of anisotropic neutron radiographs was performed with obvious improvements in human readability. While the system yielded the desired small footprint, the high aspect ratio, long-length collimators had unintended consequences with regard to neutron beam spectral content. The gadolinium covered foils preferentially absorbed a large fraction of the thermal neutrons when compared to the historic records for the Cd_{ratio} . This entire work can be summed up in one image where the culmination of effort can be put on display; this image is given in Figure 73; this composite image is composed of the two representative input images and the two main results of the 2D-DWT reconstruction methods developed.

Future work should include the expansion of the algorithm to use directional wavelets, which would allow the use of more images with the collimator oriented at angles in between the x and y-directions used in this dissertation. This additional data would allow a more complete reconstruction that would not require averaging of the diagonal elements of the wavelet transform, and the information would be directly available. In addition to the above expansion, the method could be designed to use different wavelets at different scales to leverage each wavelet's strengths. An adaptive algorithm is desired to determine which data to use in the image reconstruction.

There are changes envisioned for the neutron radiography facility at the TEES NSC. There is an ongoing renovation effort, and the radiography capability is a part of that effort. The radiography cave has been torn down and it is intended to be rebuilt

using a smaller footprint that is now practical due to the high collimation of the neutron beam. This will free up more space for radioisotope production and lab worker safety. Thus, the implications of this work reach further than an academic study and improve the NSC as a world class research facility. In addition, the impacts can be realized in any imaging system where the physical process involved with the acquisition of image data produces anisotropy in the resolution of the data. This could also be utilized in synthetic aperture radar imaging systems in which the scanning radar has different x and y resolution. These impacts and conclusions summarized in the following list.

1. DWTs were successfully used to develop a method to fuse anisotropic resolution images.
2. The anisotropic DWT reconstruction method was shown to be capable of fusing two orthogonal, anisotropic resolution image datasets into a single isotropic image dataset.
3. The anisotropic DWT reconstruction method has also been shown to be capable of removing certain periodic image artifacts from the isotropic dataset. This also depends on the wavelet that is chosen.
4. Future work would include the incorporation of directional wavelets. This would allow for the use of more collimator orientations to improve the reconstruction results.

REFERENCES

- [1] International Atomic Energy Agency, "Neutron Imaging: A Non-Destructive Tool for Materials Testing," IAEA, Vienna, Austria, 2008.
- [2] I. S. Anderson, R. L. McGreevy and H. Z. Bilheux, *Neutron Imaging and Applications*, New York, NY: Springer, 2009.
- [3] A. Athanasiades, N. N. Shehad, C. S. Martin, L. Sun and J. L. Lacy, "Straw Detector for High Rate, High Resolution Neutron Imaging," *IEEE Nuclear Science Symposium Conference Record*, pp. 623-627, 2005.
- [4] International Atomic Energy Agency, "Neutron Radiography Facilities," IAEA, [Online]. Available: http://www-naweb.iaea.org/napc/physics/research_reactors/database/RR%20Data%20Base/datasets/utilization/neutron_rad_list.html. [Accessed 11 8 2014].
- [5] E. Lehmann, H. Pleinert and L. Wiezel, "Design of a Neutron Radiography Facility at the Spallation Source SINQ," *Nuclear Instruments and Methods in Physics Research A*, no. 377, pp. 11-15, 1996.
- [6] CE. C, Joint Research Centre, Petten Establishment, *Neutron Radiography Handbook*, Boston, USA: D. Reidel Publishing Company, 1981.
- [7] A. Sykes, M. Gryaznevich, G. Voss and D. Kingham, "Fusion for Neutrons: a Realisable Fusion Neutron," in *IEEE/NPSS 24th Symposium on Fusion Engineering*, 2011.
- [8] J. G. Fantidis, B. V. Dimitrios, P. Constantinos and V. Nick, "Fast and Thermal Neutron Radiographies Based on a Compact Neutron Generator," *Journal of Theoretical and Applied Physics*, vol. 6, no. 20, pp. 1-8, 2012.
- [9] J. A. Hamley, P. W. McCallum, C. E. Sandifer, T. J. Sutliff and a. J. F. Zakrajsek, "NASA's Radioisotope Power Systems - Plans," in *13th International Energy Conversion Engineering Conference*, Orlando, FL, 2015.
- [10] A. Ainsworth, "Review of Actinide Source Technology," *Journal of the Less-Common Metals*, vol. 122, pp. 383-399, 1986.
- [11] G. M. MacGillivray, "Neutron Radiography Collimator Design," Nray Services

Inc., Petawawa, Ontario, Canada.

- [12] S. A. Werner and A. G. Klein, "Neutron Optics," *Rep. Prog. Phys*, vol. 46, pp. 259-335, 1983.
- [13] Eurocollimator Ltd., "eurocollimators Ltd.," [Online]. Available: <http://www.eurocollimators.com/Resources/Standard%20Mylar%20Foil%20Soller%20Collimators.pdf>. [Accessed 12 12 2015].
- [14] J. C. Domanus, *Practical Neutron Radiography*, Boston: Kluwer Academic Publishers, 1992.
- [15] H. Bilheux, J. Katsaras, C. Stanley, A. Ramanathan, D. Myles and M. Cekanova, "Multi-Scale Applications of Neutron Scattering and Imaging," BSEC-ORNL, Oak Ridge, TN, 2014.
- [16] D. Liu, D. Hussey, M. V. Gubarev, B. D. Ramsey, D. Jacobson, M. Arif, D. E. Moncton and B. Khaykovich, "Demonstration of Achromatic Cold-Neutron Microscope Utilizing Axisymmetric Focusing Mirrors," *Applied Physics Letters*, vol. 102, 2013.
- [17] A. C. Marshall, *Space Nuclear Safety*, Malabar, FL: Krieger Publishing Company, 2008.
- [18] N. Soppera, "Java-based Nuclear Data Information System," OECD, 2014. [Online]. Available: <http://www.oecd-nea.org/janis/>. [Accessed 9 2014].
- [19] I. S. Anderson, R. L. McGreevy and H. Z. Bilheux, *Neutron Imaging and Applications*, New York, NY: Springer, 2009.
- [20] J. S. Brenizer, "A Review of Significant Advances in Neutron Imaging from Conception to the Present," *Physics Procedia*, vol. 43, pp. 10-20, 2013.
- [21] N. Kardjilov, M. Dawson, A. Hilger, I. Manke, M. Strobl, D. Penumadu, F. H. Kim, F. Garcia-Moreno and J. Banhart, "A Highly Adaptive Detector System for High Resolution Neutron Imaging," *Nuclear Instruments and Methods in Physics Research A*, no. 651, pp. 95-99, 2011.
- [22] M. Strobl, I. Manke, N. Kardjilov, A. Hilger, M. Dawson and J. Banhart, "Advances in Neutron Radiography and Tomography," *Journal of Physics D: Applied Physics*, no. 42, p. 21, 2009.

- [23] H. K. Jenssen, B. Oberlander, J. Beenhouwer, J. Sijbers and M. Verwerft, "Neutron Radiography and Tomography Applied to Fuel Degradation During Ramp Tests and Loss of Coolant Accident Tests in a Research Reactor," *Progress in Nuclear Energy*, pp. 1-8, 2013.
- [24] D. Jacobson, B. Allman, P. McMahon, K. Nugent, D. Paganin, M. Arif and S. Werner, "Thermal and Cold Neutron Phase-Contrast Radiography," *Applied Radiation and Isotopes*, no. 61, pp. 547-550, 2004.
- [25] A. E. Craft, D. M. Wachs, M. A. Okuniewski, D. L. Chichester, W. J. Williams, G. C. Papaioannou and A. T. Smolinski, "Neutron Radiography of Irradiated Nuclear Fuel at Idaho National Laboratory," *Physics Procedia*, no. 69, pp. 483-490, 2015.
- [26] T. Smith, H. Bilheux, H. Ray, J.-C. Bilheux and Y. Yan, "High Resolution Neutron Radiography and Tomography of Hydrided Zircaloy-4 Cladding Materials," *Physics Procedia*, no. 69, pp. 478-482, 2015.
- [27] T. Trabold, J. Owejan, D. Jacobson, M. Arif and P. Huffman, "In Situ Investigation of Water Transport in an Operating PEM Fuel Cell Using Neutron Radiography: Part 1 - Experimental Method and Serpentine Flow Field Results," *International Journal of Heat and Mass Transfer*, no. 49, pp. 4712-4720, 2006.
- [28] N. Putra, R. S. Ramadhan, W. N. Septiadi and Sutiarmo, "Visualization of the Boiling Phenomenon Inside a Heat Pipe Using Neutron Radiography," *Experimental Thermal and Fluid Science*, no. 66, pp. 13-27, 2015.
- [29] E. Solórzanoa, E. Laguna-Gutierrez, S. Perez-Tamarita, A. Kaestnerb and M. Rodriguez-Pereza, "Polymer Foam Evolution Characterized by Time-Resolved Neutron Radiography," *Colloids and Surfaces A: Physicochemical and Engineering Aspects*, no. 473, pp. 46-54, 2015.
- [30] D. Jacobson, D. Hussey, E. Baltic, T. Udovic, J. Rush and R. Bowman, "Neutron Imaging Studies of Metal-Hydride Storage Beds," *International Journal of Hydrogen Energy*, vol. 35, no. 23, p. 12837-12845, 2010.
- [31] W. Majewski, "The Case for the Diesel Engine," 2004. [Online]. Available: www.dieselnet.com. [Accessed 30 4 2014].
- [32] J. Zandhuis, C. Finney, T. Toops, S. Daw and T. Fox, "Non-Destructive X-ray Measurement of Soot, Ash, Washcoat and Regeneration Damage in DPFs," in *11th CLEERS Workshop*, Dearborn, MI, 2008.

- [33] A. Strzelec, H. Bilheux, C. Finney, C. Daw, D. Foster, C. Rutland, B. Schillinger and M. Schulz, "Neutron Imaging of Diesel Particulate Filters," in *SAE*, 2009.
- [34] J. E. Dec, "A Conceptual Model of DI Diesel Combustion Based on Laser- Sheet Imaging," in *Society of Automotive Engineers*, 1997.
- [35] G. J. Smallwood, O. L. Guelder and D. R. Snelling, "The Structure of the Dense Core Region in Transient Diesel Sprays," in *25th Symposium (International) on Combustion*, 1994.
- [36] Y. Yue, C. F. Powell, R. Poola, J. Wang and J. K. Schaller, "Quantitative Measurements of Diesel Fuel Spray Characteristics in the Near-Nozzle Region Using X- ray Absorption," *Atomization and Sprays*, vol. 4, no. 11, pp. 470-490, 2001.
- [37] W. K. Pratt, *Digital Image Processing*, New York: John Wiley and Sons, Inc., 2001.
- [38] W. Burger and M. J. Burge, *Digital Image Processing*, New York, NY: Springer, 2008.
- [39] F. Neyenssac, "Contrast Enhancement Using the Laplacian-of-a-Gaussian Filter," *Graphical Models and Image Processing*, vol. 55, no. 6, pp. 447-463, 1993.
- [40] E. Burke, J. Boyle and H. Huemmler, "Gamma-Induced Noise In CCDs," *IEEE Transactions on Nuclear Science*, Vols. NS-28, no. 6, pp. 4068-4073, 1981.
- [41] L. Archambault, T. M. Briere and S. Beddar, "Transient Noise Characterization and Filtration in CCD Cameras Exposed to Stray Radiation from a Medical Linear Accelerator," *Medical Physics*, vol. 35, pp. 4342-4351, 2008.
- [42] J. S. Lim, *Two-Dimensional Signal and Image Processing*, Englewood Cliffs, NJ: Prentice Hall, 1990.
- [43] E. Samei, "Performance of Digital Radiographic Detectors: Quantification and Assessment Methods," *Advances in Digital Radiography*, pp. 37-47, 2003.
- [44] K. Rossmann, "Point Spread-Function, Line Spread-Function, and Modulation Transfer Function," *Radiology*, vol. 93, no. 2, pp. 257-272, 1969.
- [45] E. W. Marchand, "Derivation of the Point Spread Function from the Line Spread Function," *Journal of the Optical Society of America*, vol. 54, no. 7, pp. 915-919, 1964.

- [46] B. Zitova and J. Flusser, "Image Registration Methods: A Survey," *Image and Vision Computing*, vol. 21, pp. 977-1000, 2003.
- [47] B. S. Reddy and B. N. Chatterji, "An FFT-Based Technique for Translation, Rotation, and Scale-Invariant Image Registration," *IEEE Transactions on Image Processing*, vol. 5, no. 8, pp. 1266-1271, August 1996.
- [48] A. K. Chan and C. Peng, *Wavelets for Sensing Technologies*, Norwood, MA: Artech House, Inc., 2003.
- [49] I. Daubechies, "Ten Lectures on Wavelets," in *Society for Industrial and Applied Mathematics*, 1992.
- [50] E. Roullot and e. al., "Modeling Anisotropic Undersampling of Magnetic Resonance Angiographies and Reconstruction of a High-Resolution Isotropic Volume Using Half-Quadratic Regularization Techniques," *Signal Processing*, pp. 743-762, 2004.
- [51] K. M. Hanson, "Introduction to Bayesian image analysis," in *Proceedings in SPIE*, 1993.
- [52] J. Newhouse, Interviewee, *Nuclear Science Center Tour*. [Interview]. 3 10 2014.
- [53] National Instruments, "NI USB-6501 User Guide and Specifications," National Instruments Corporation, Austin, Texas, 2014.
- [54] G. F. Knoll, *Radiation Detection and Measurement*, Hoboken, NJ: John Wiley & Sons, Inc., 2010.
- [55] N. E. Holden, "Neutron Capture Cross Section Standards for BNL 325," Brookhaven National Laboratory Associated Universities, Inc., Upton, New York, 1981.
- [56] R. R. Cook, *Assessment of Uncertainties of Measurement for Calibration and Testing Laboratories*, Australia: National Association of Testing Authorities, 2002.
- [57] V. Lavrakas, "A History of the Neutron," *Journal of Chemical Education*, vol. 26, no. 6, pp. 281-283, 1952.
- [58] J. Chadwick, "Possible Existence of a Neutron," *Nature*, p. 312, 27 February 1932.

APPENDIX A

ADDITIONAL IMAGES

Many images were acquired during the initial setup of the experimental systems. It was decided that many items around the NSC could be examined using the neutron beam from the reactor. This mission was set upon with much vigor.

Test Items

Figure 74 was the first image of an object acquired with the updated neutron imaging system. This image was taken using a one inch collimator. Figure 75 is a cathode ray television that was acquired from the TAMU surplus department. Figure 76 is an ion chamber radiation detector that was previously determined to be inoperable. Figure 77 is a two-stroke leaf blower motor from the NSC machine shop. Figure 78 is an old wrench that was found in a box of neutron imaging equipment from the early 90s, and the aluminum tube came off the foot of the stairs that were used to access the neutron imaging stage. These images were produced using a three-inch-aperture collimator at an approximate distance of 2 m.



Figure 74. Cell phone (left) and hard disk drive (right).

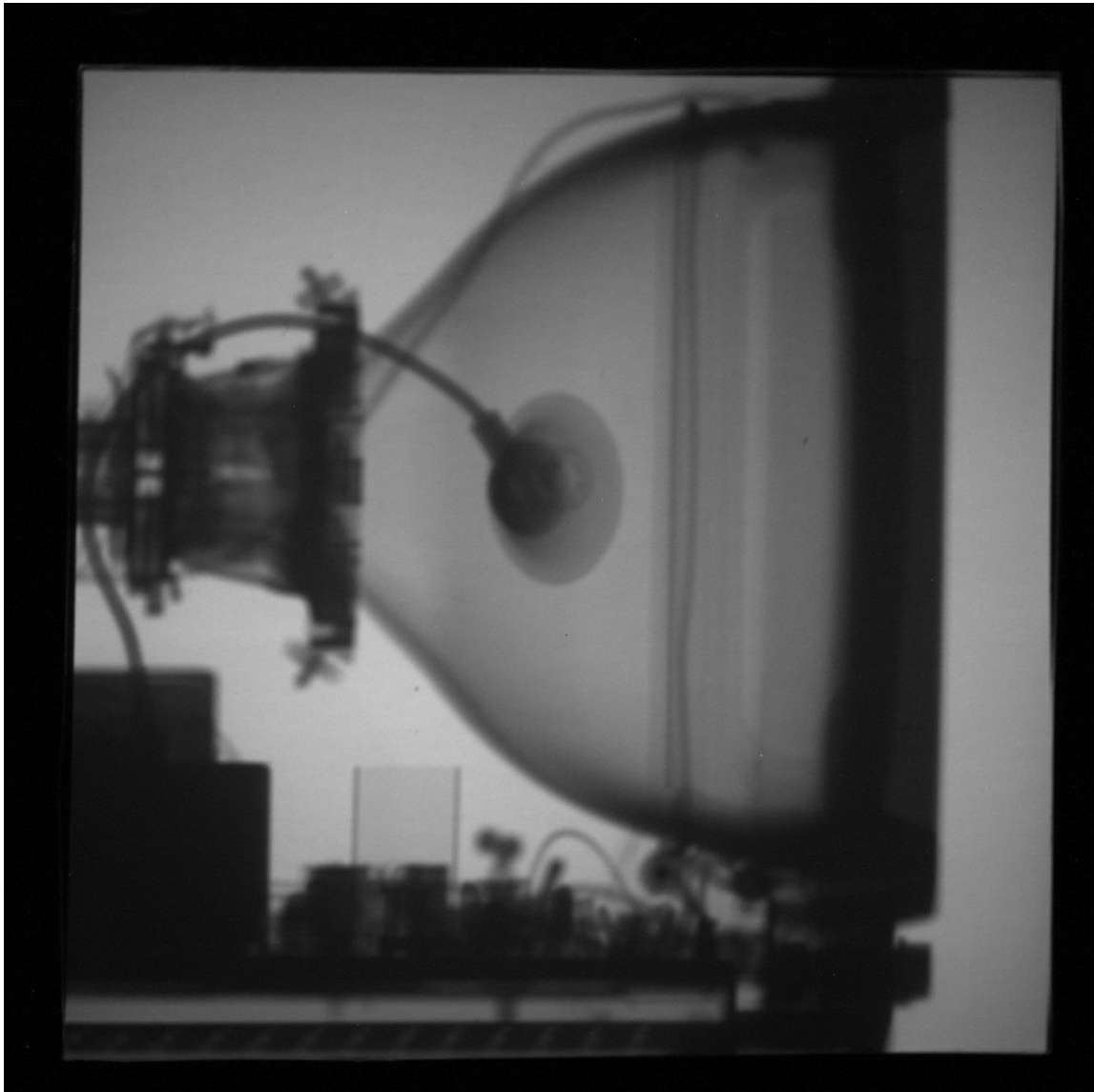


Figure 75. Cathode ray tube television.

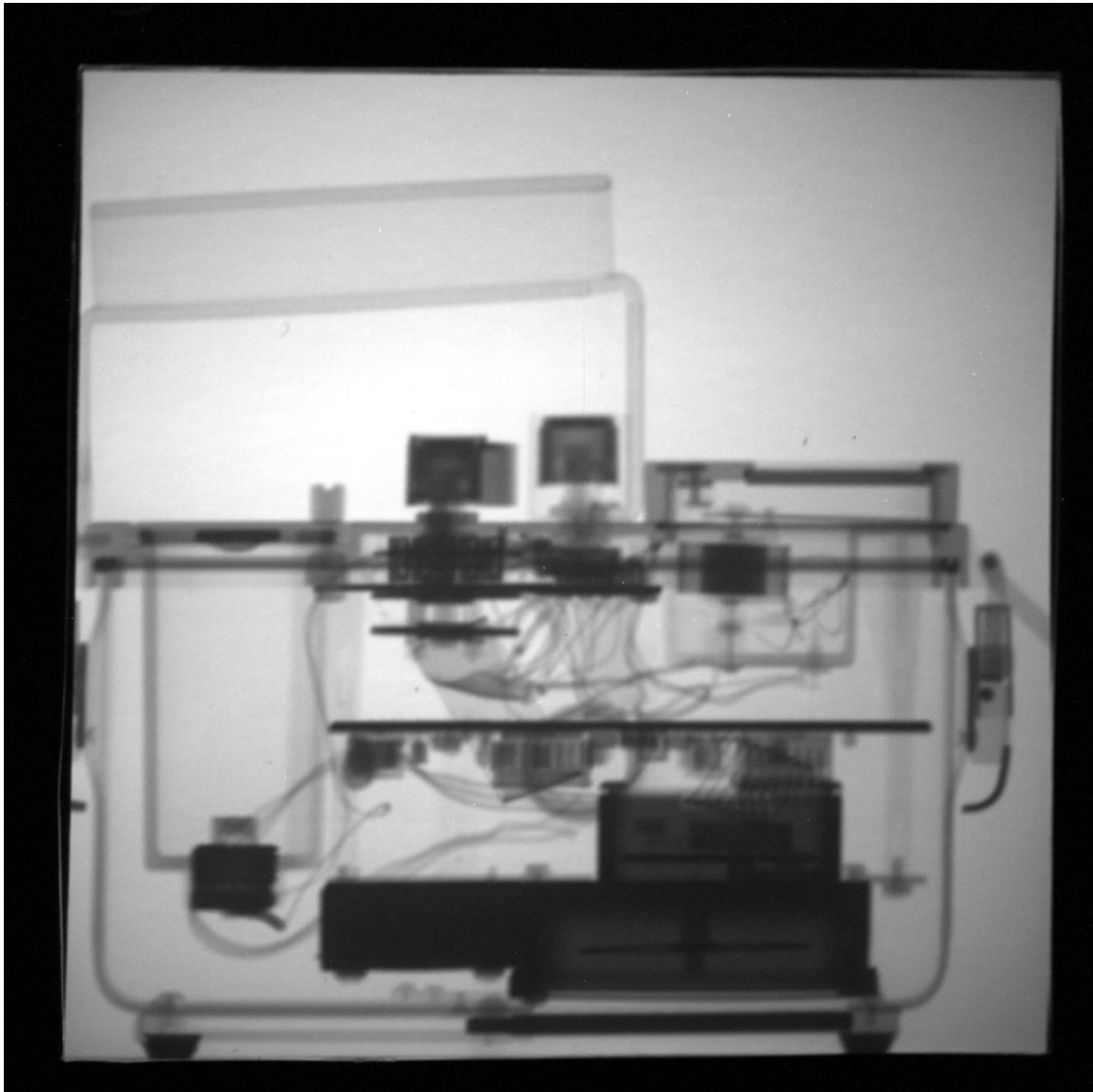


Figure 76. Ion chamber beta and gamma radiation detector (without batteries).

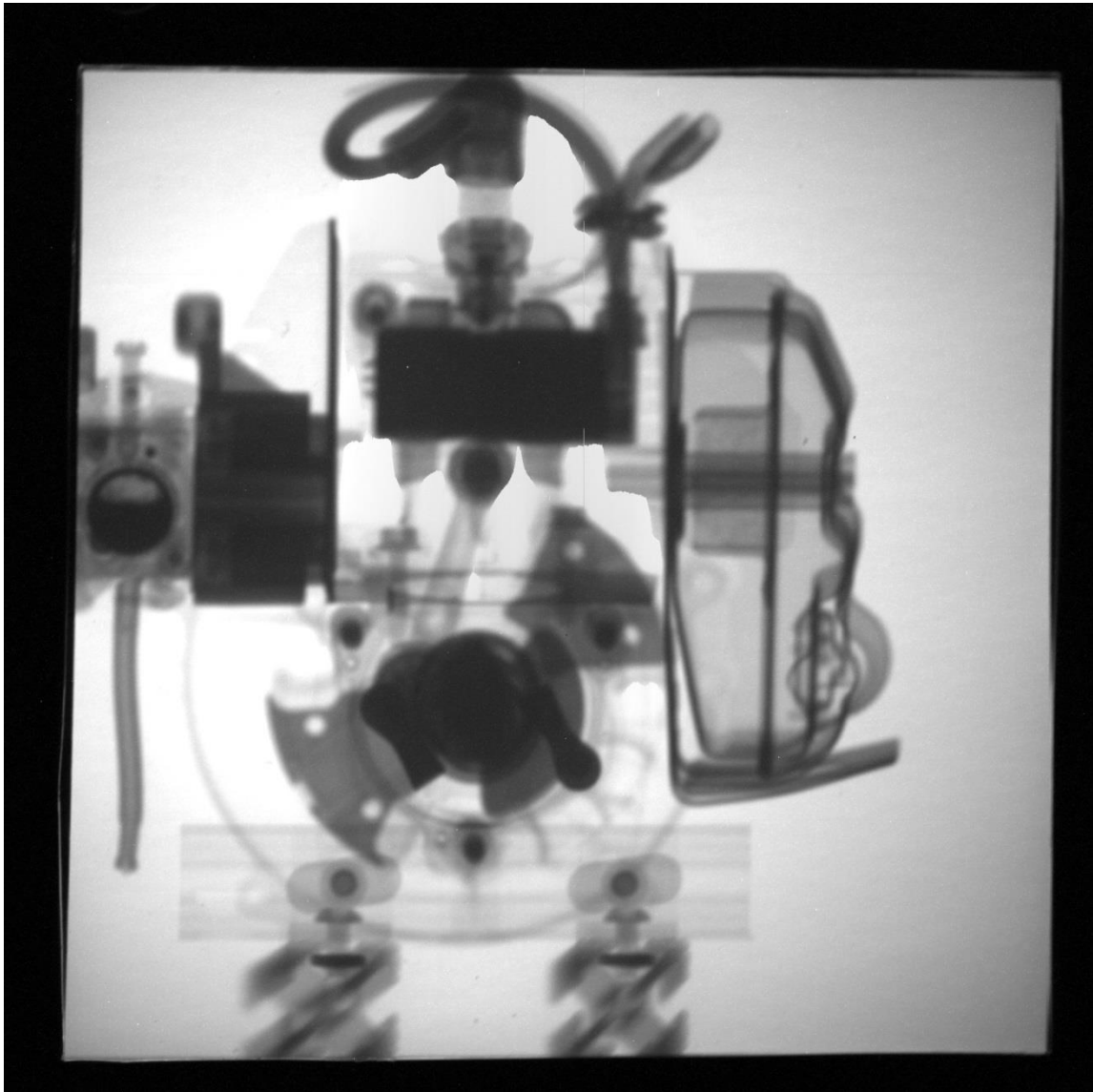


Figure 77. Two-stroke leaf blower motor with the outer plastic shroud removed.

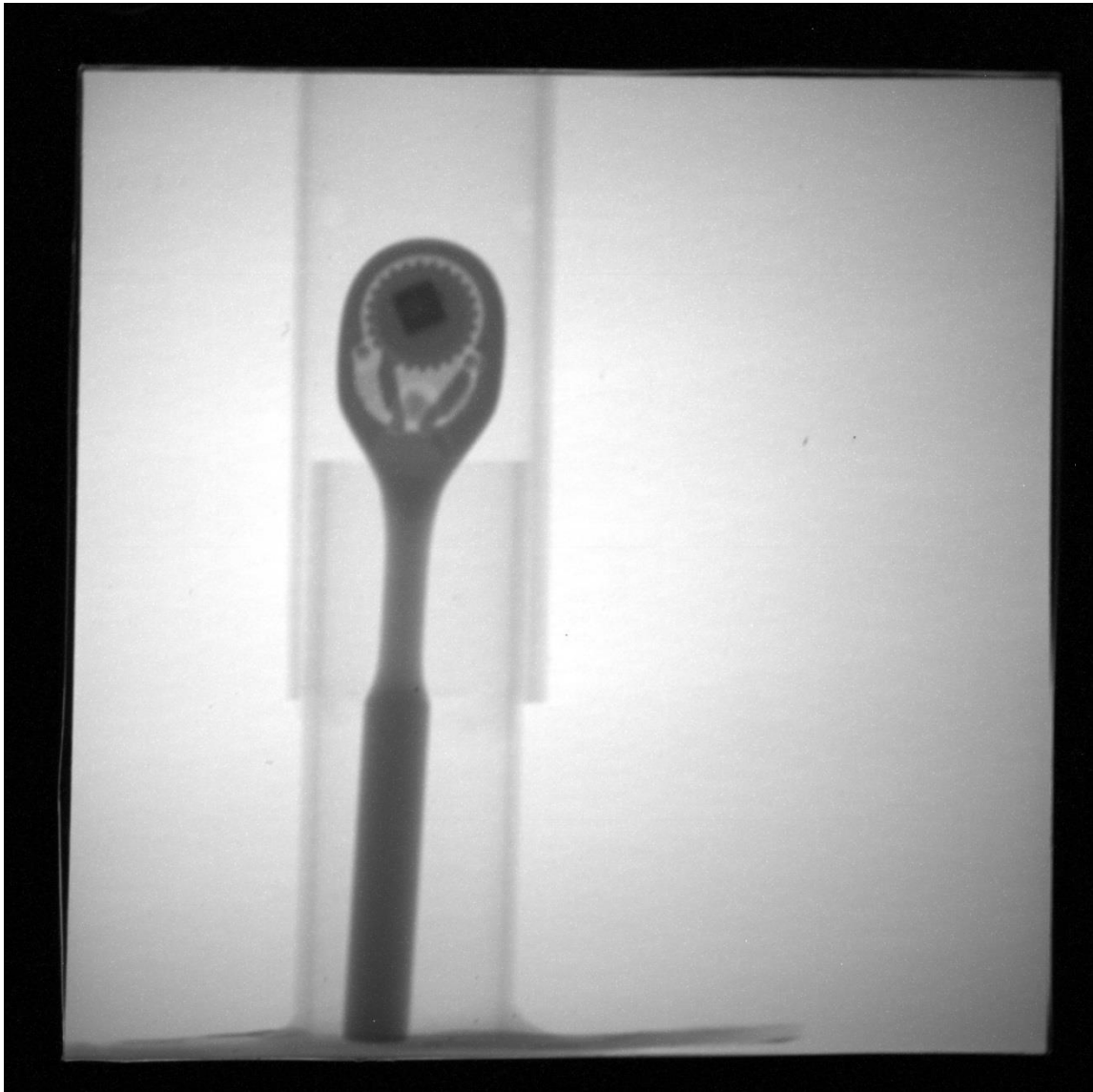


Figure 78. 3/8" socket driver inside of an aluminum tube.



Figure 79. Micropixel neutron camera (left), Swagelok valve (middle), heat pipe (right).

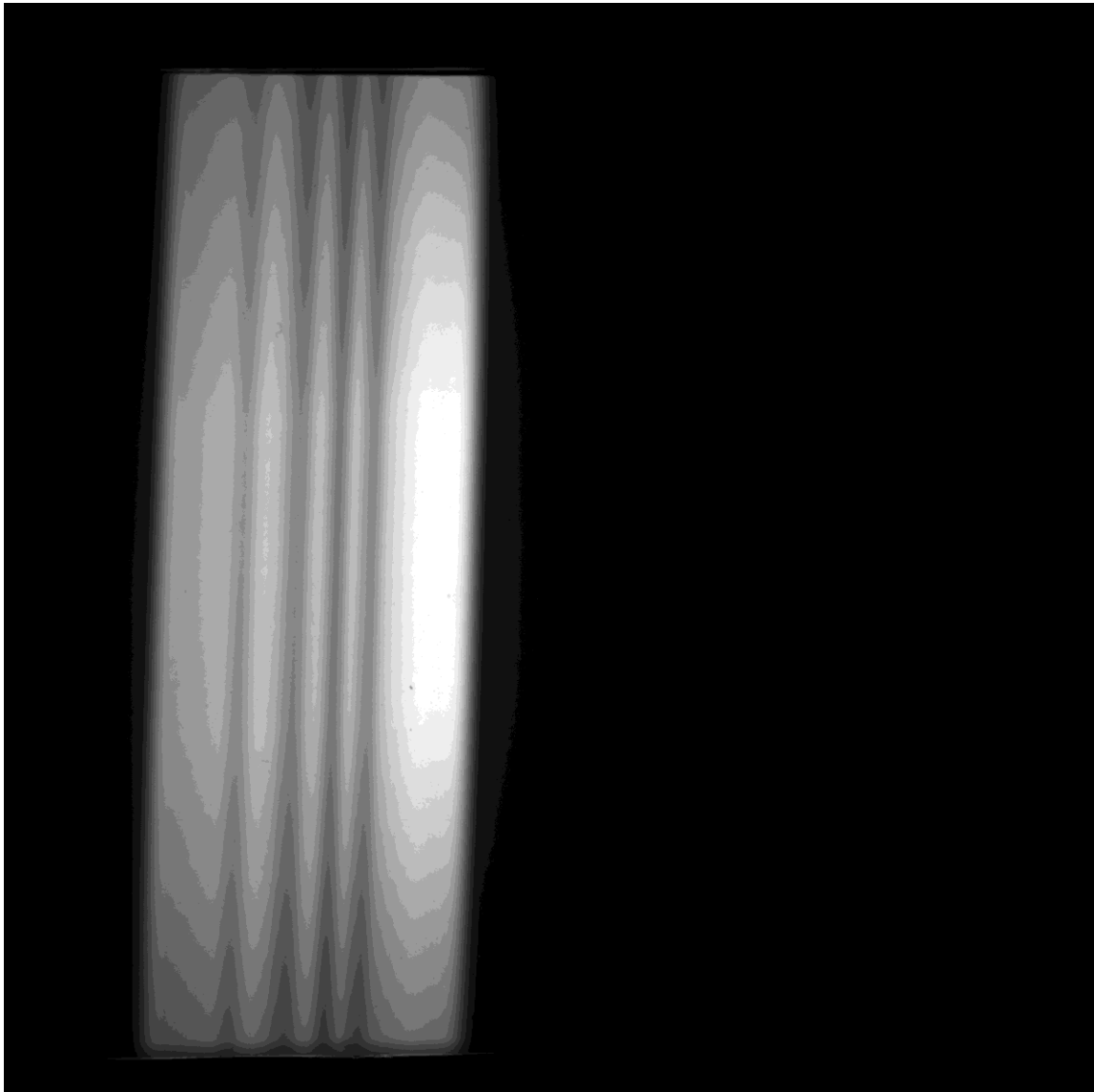


Figure 80. Open field image.

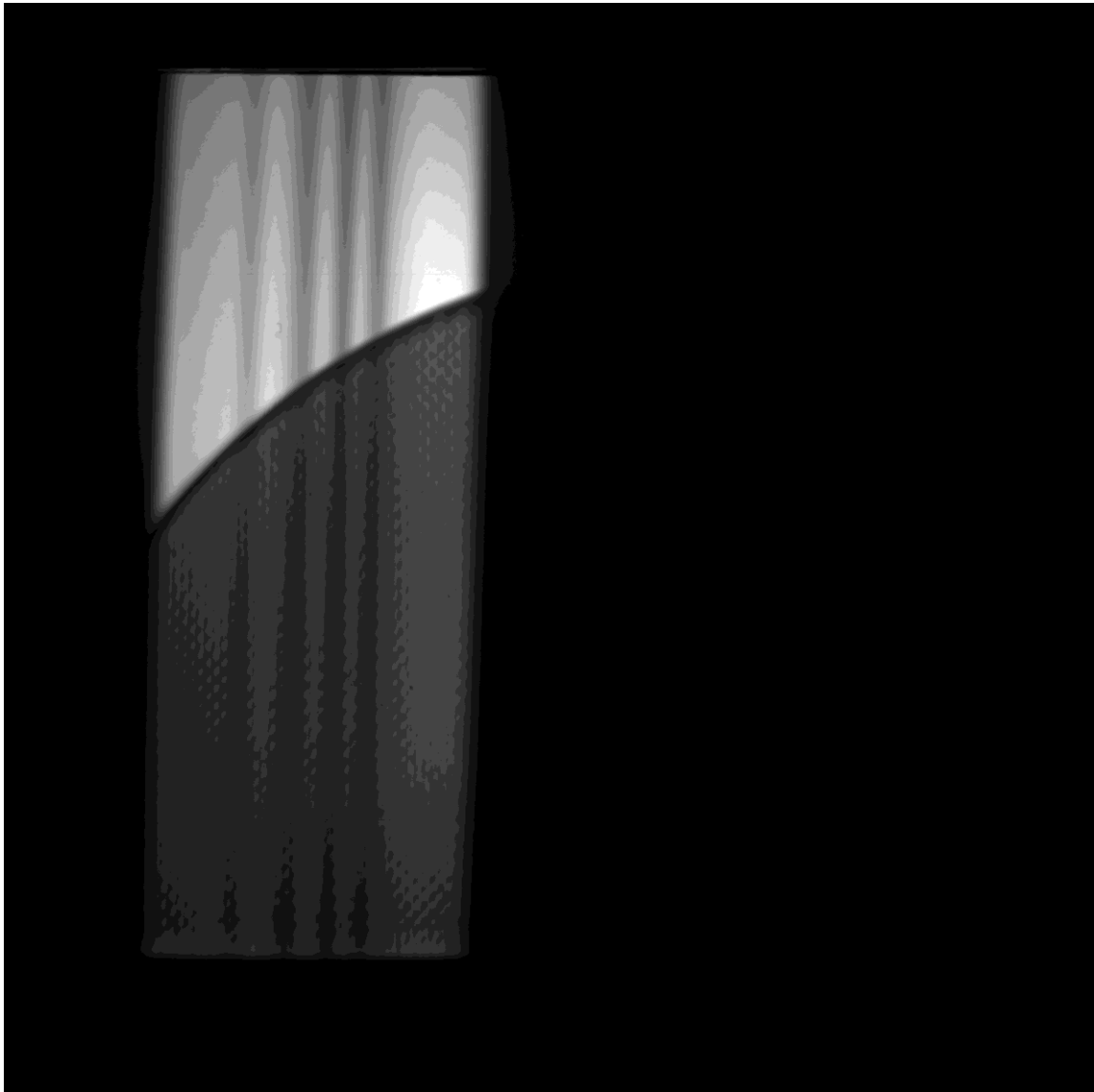


Figure 81. Diesel particulate filter.

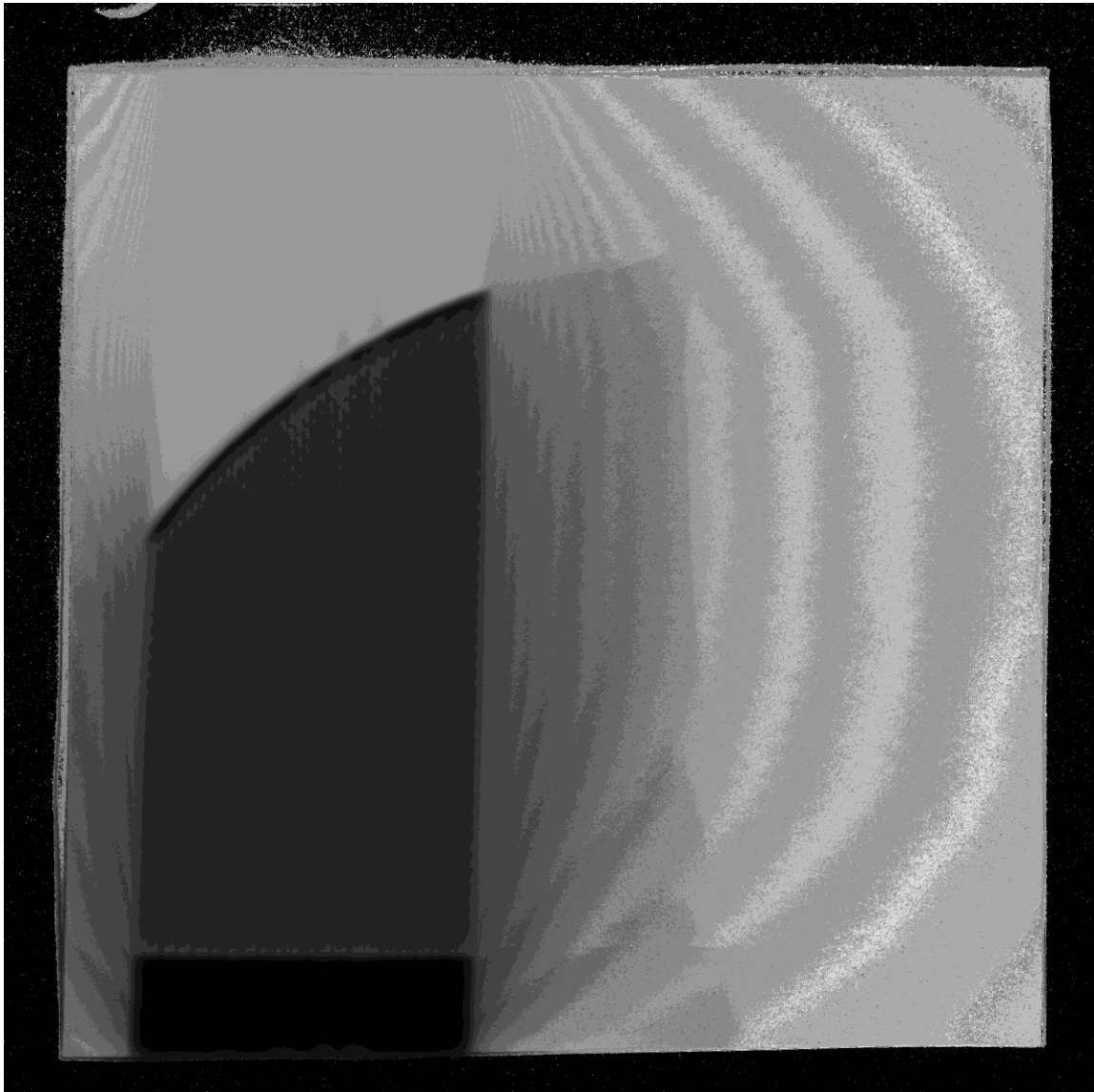


Figure 82. Normalized image using the ratio of the object image to the open field image.

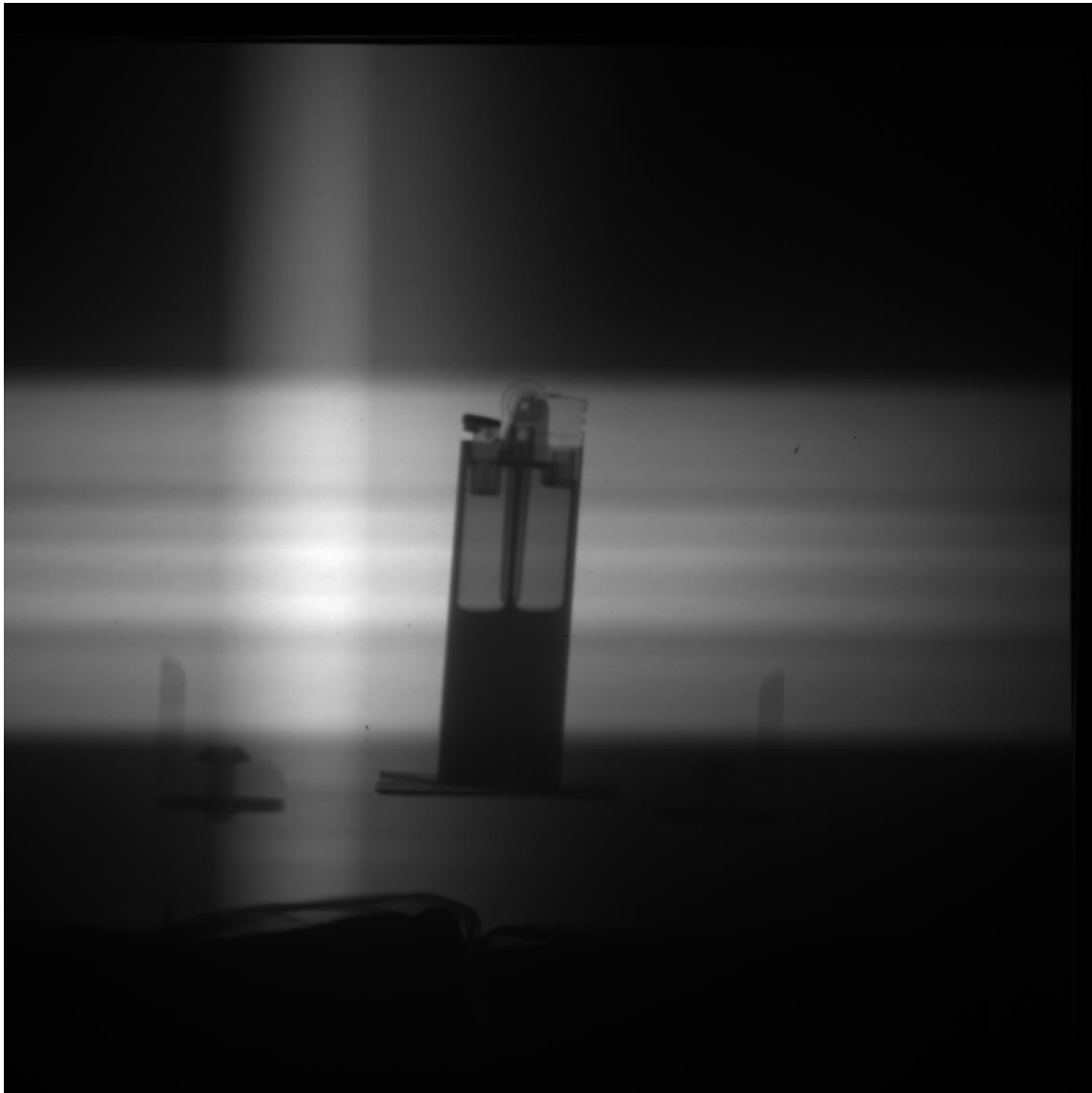


Figure 83. BIC lighter with butane lighter fuel.

Undergraduate Laboratory Items

Additionally, three neutron imaging undergraduate laboratory sections were taught using the NIS1 system. The undergraduate students were instructed to bring potential items of interest to examine in the neutron beam. Before the laboratory began, it was decided to attempt to use both collimators in the neutron beam port. The neutron and

gamma ray window was not replaced before the radiography cave was secured and this resulted in the strange illumination pattern that is apparent in Figure 84 through Figure 91.

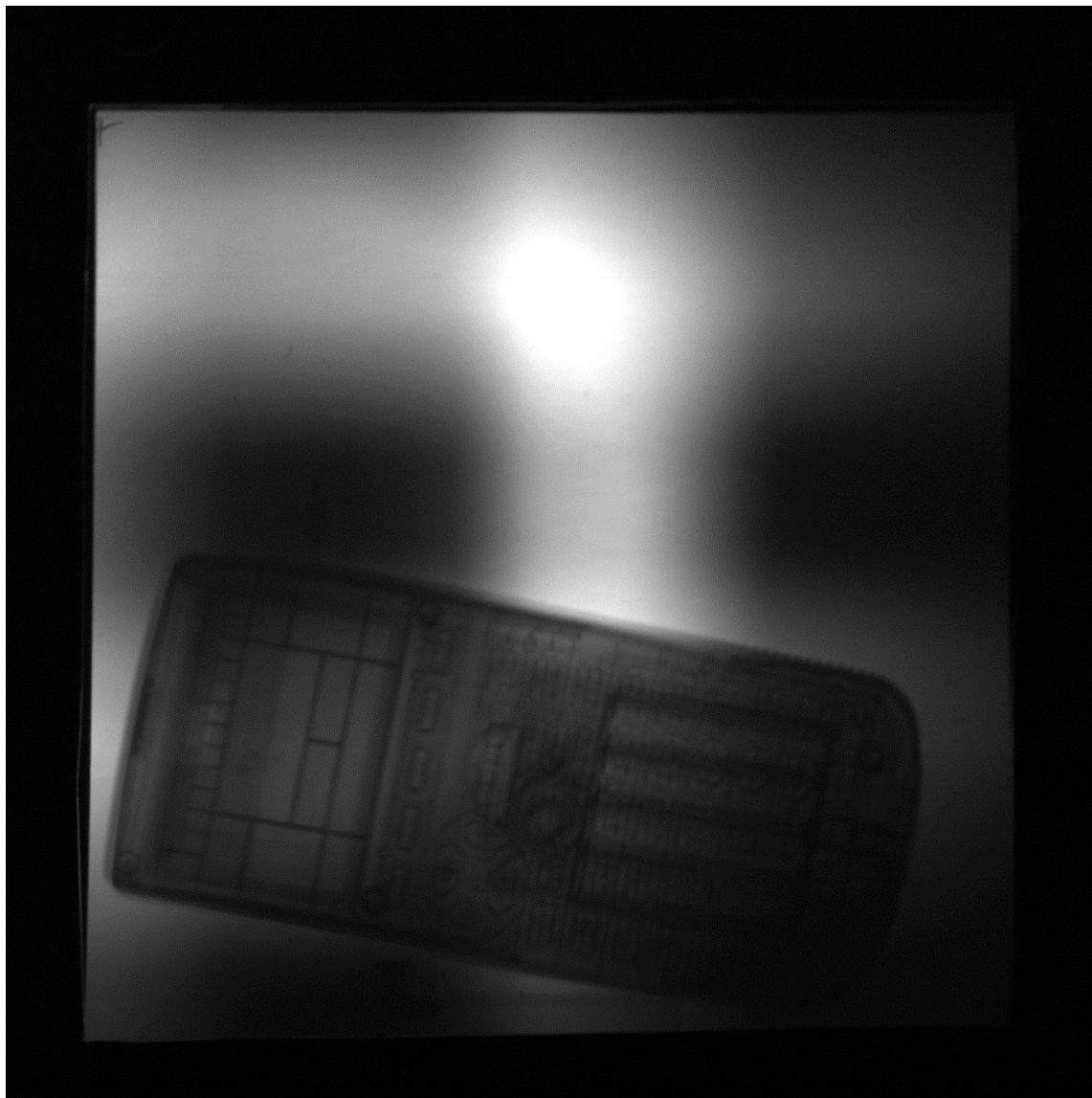


Figure 84. TI-89 calculator.

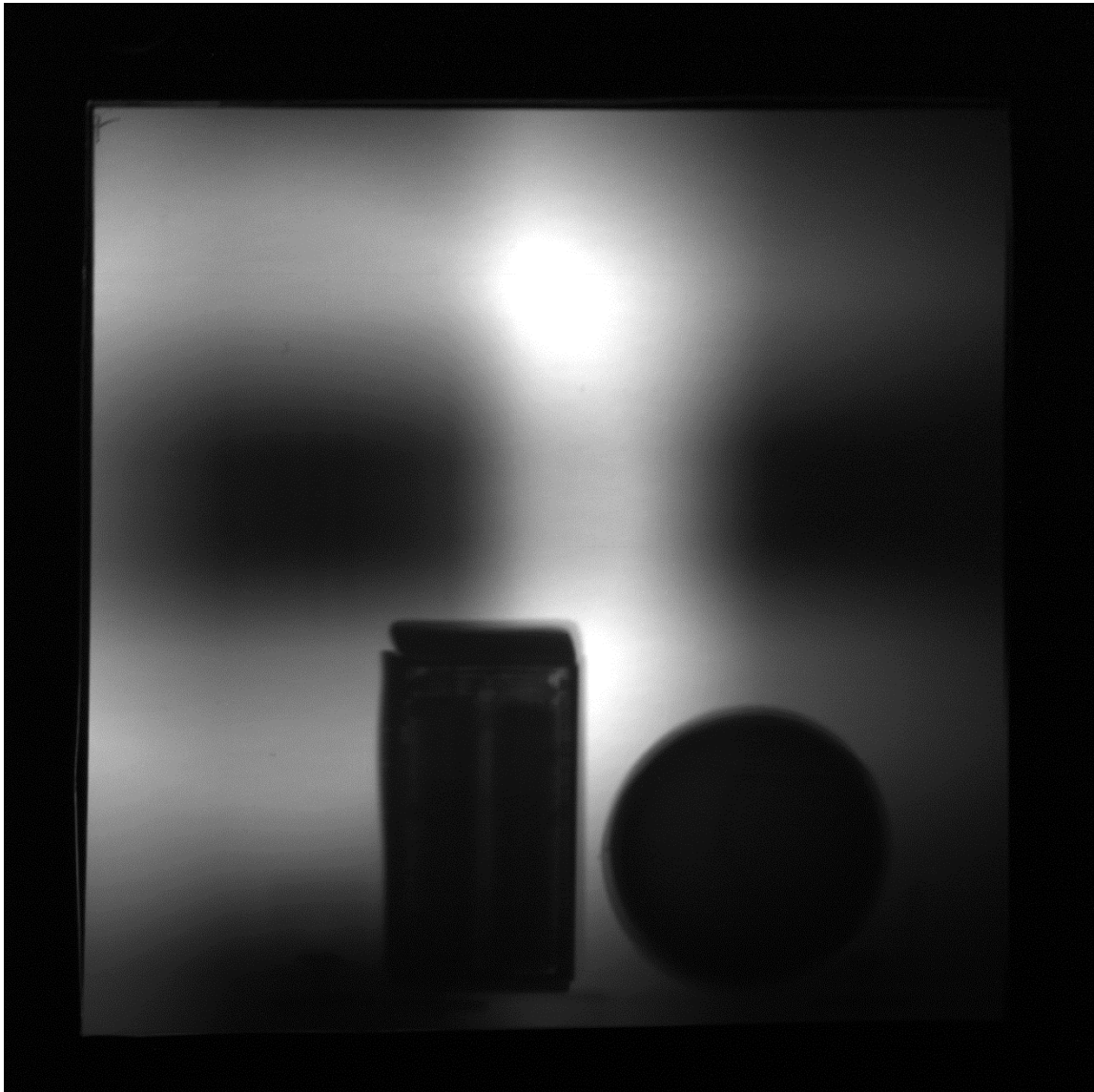


Figure 85.Charger and rubber ball.



Figure 86. Battery operated drill.

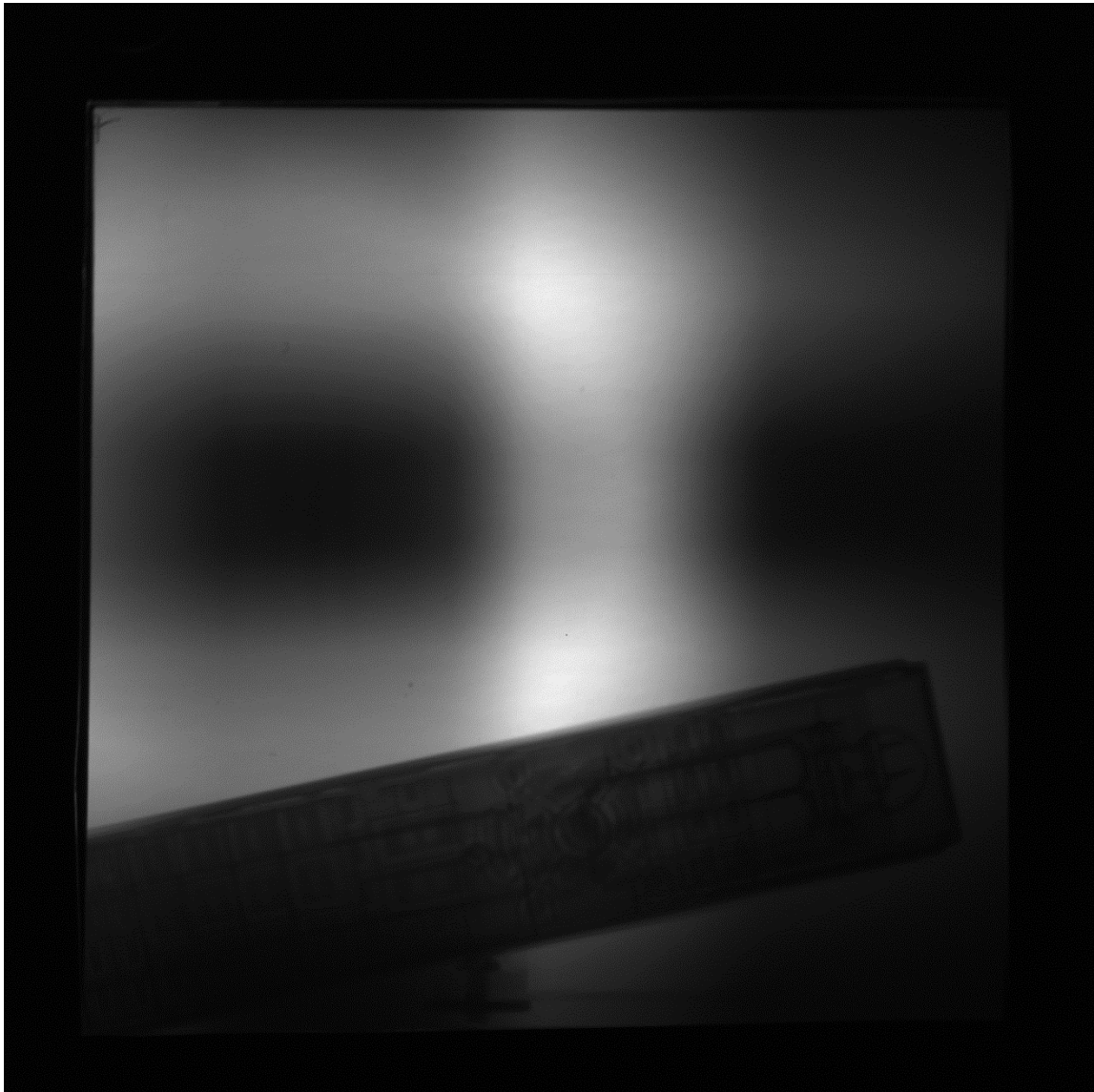


Figure 87. Television remote.

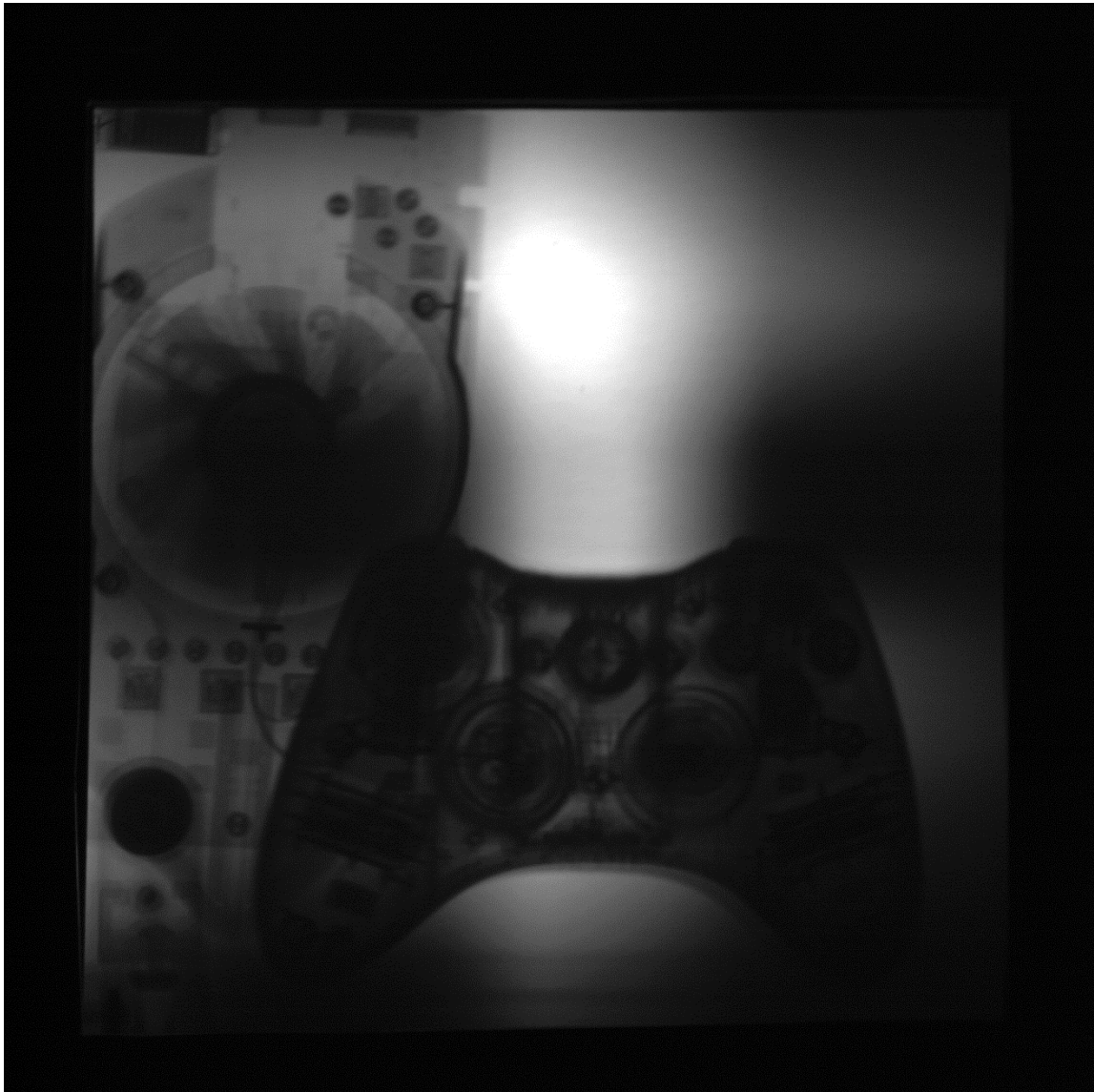


Figure 88. Desktop graphics card (left) and an XBOX 360™ controller (right).



Figure 89. Ion chamber beta and gamma radiation detector.

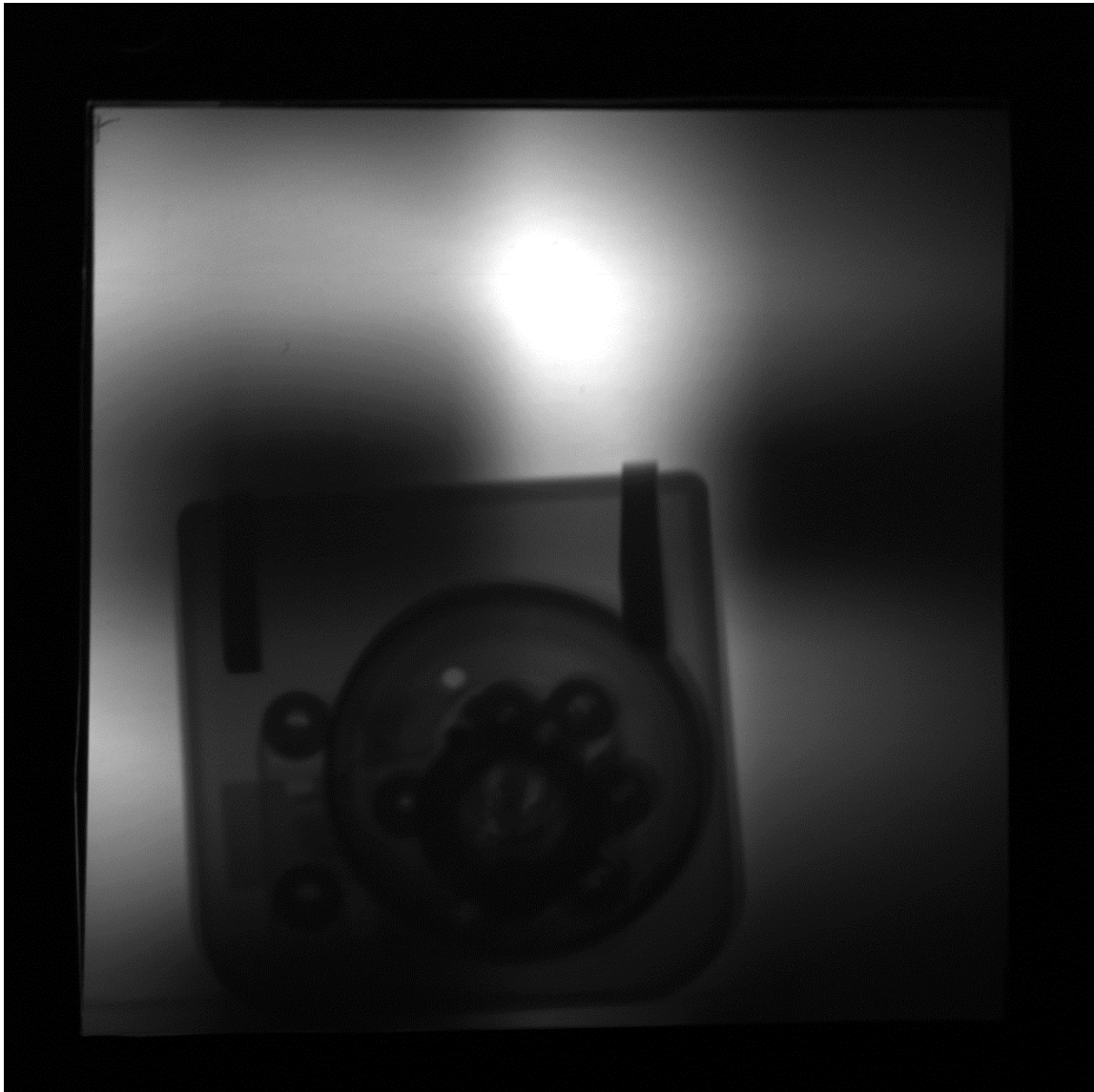


Figure 90. Safe combination lock.



Figure 91. Master lock (left), wrist watch (middle), safe combination lock (right).

Zircaloy Cladding Samples

Two pieces of Zircaloy cladding were also imaged to determine the capability of the neutron imaging system to detect hydrogen content within the cladding specimens. Figure 92 is an image of the two Zircaloy samples and is a perfect example of an image

of weakly attenuating materials. Figure 93 is the same image as Figure 92, but it has the objects of interest removed.

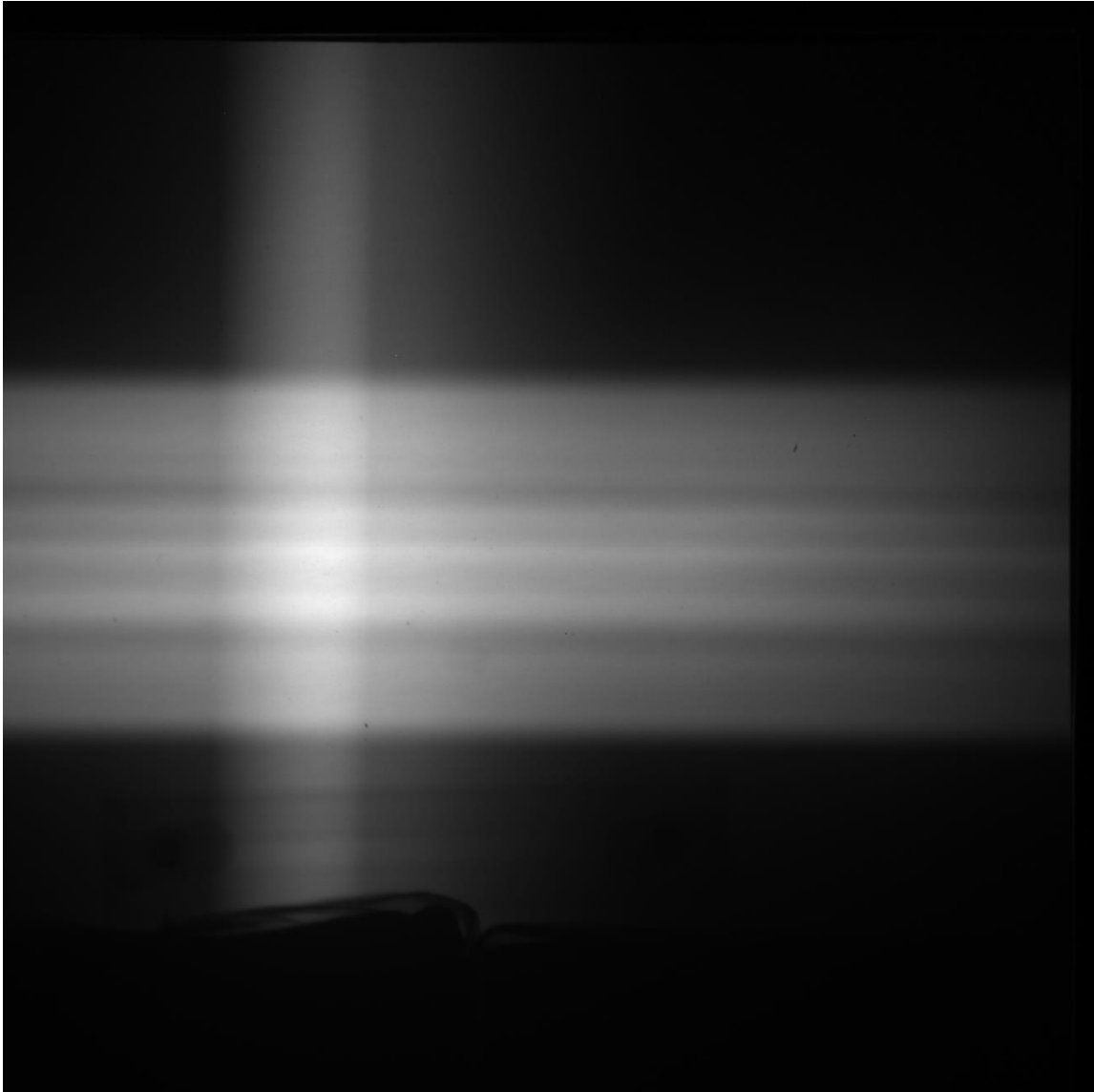


Figure 92. Raw image of the two Zircaloy samples.

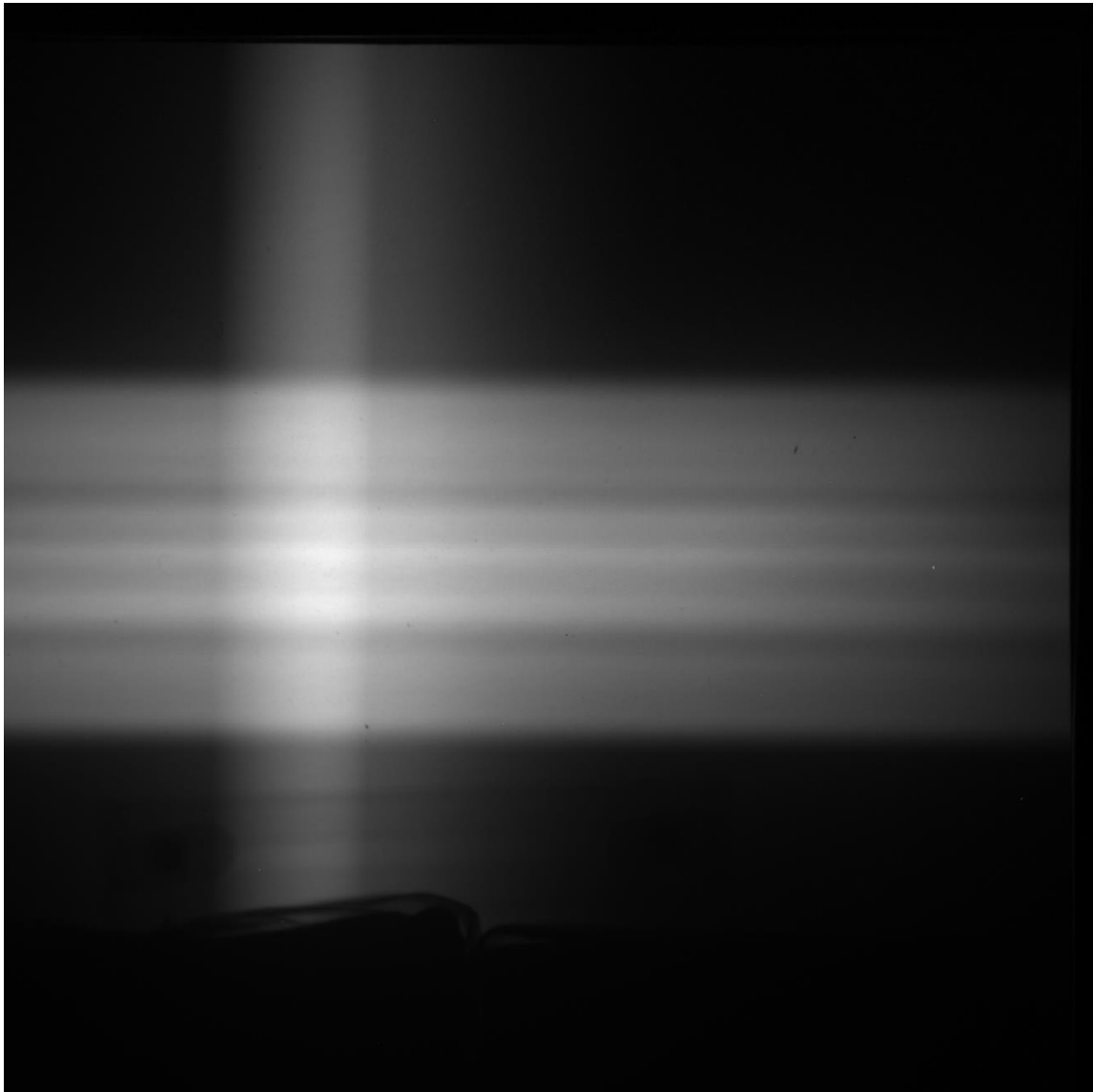


Figure 93. Open field image used to normalize the final image.

Figure 94 is the normalized image in which the open field image was used to remove the beam profile artifacts.



Figure 94. Zircaloy control (left) and hydrided Zircaloy (right) samples.

APPENDIX B

2D-DWT METHOD CODE

```
%% Filtering using the Discrete Wavelet Transform
clear
t0 = now; % Start calculation time
% rect = [800 500 1770 1500];
% data_importW(rect);
%import_processed();
%Stretch(10, [5 5]);
ftype = 'db8';
dwtmode('symw');
load im_data.mat
[i,j,k] = size(image_stack);

% Automatically chose the maximum decomposition level for the image set
level = wmaxlev(size(image_stack(:,:,1)),ftype);
% 1:4 is the vertical set and 5:8 is the horizontal set
for a = 1:k
    [C(:,a),S] = wavedec2(image_stack(:,:,a),level,ftype);
end

% Determine the length of each level of image transform
[n,~] = size(S);
for b = 1:n
    N(b) = S(b,1)*S(b,2);
end

% Determine the transition points from one image to another.
image_points = zeros(1,3*level+1);
image_points(1) = N(1);
for f = 1:level
    for e = 3*f-1:3*f+1
        image_points(e) = image_points(e-1) + N(f+1);
    end
end

[~,m] = size(C);
imageR = zeros(1,m);
for c = 1:image_points(1)
    imageR(c) = mean(C(c,1:k));
end
for f = 1:level
    for e = 3*f-1:3*f+1
        % Horizontal Details
        if e == 3*f-1
            for c = image_points(e-1)+1:image_points(e)
                imageR(c) = mean(C(c,1:4));
            end
        end
    end
end
```

```

        end
        % Verticle Details
    elseif e == 3*f
        for c = image_points(e-1)+1:image_points(e)
            imageR(c) = mean(C(c,5:k));
        end
        % Diagonal Details
    elseif e == 3*f+1
        for c = image_points(e-1)+1:image_points(e)
            imageR(c) = mean(C(c,1:k));
        end
    end
end
end

% Reconstruct the decimated image collection
ReconstructedE = waverec2(imageR,S,ftype);
% Compute Average image
I_ave = (image_stack(:,:,1) + image_stack(:,:,2) + image_stack(:,:,3) +
image_stack(:,:,4) + image_stack(:,:,5) + image_stack(:,:,6) +
image_stack(:,:,7) + image_stack(:,:,8))/8;

clear imageR

[~,m] = size(C);
imageR = zeros(1,m);
for c = 1:image_points(1)
    imageR(c) = mean(C(c,1:k));
end

for f = 1:level
    for e = 3*f-1:3*f+1
        % Horizontal Details
        if e == 3*f-1
            for c = image_points(e-1)+1:image_points(e)
                imageR(c) = mean(C(c,k/2+1:k));
            end
            % Verticle Details
        elseif e == 3*f
            for c = image_points(e-1)+1:image_points(e)
                imageR(c) = mean(C(c,1:k/2));
            end
            % Diagonal Details
        elseif e == 3*f+1
            for c = image_points(e-1)+1:image_points(e)
                imageR(c) = mean(C(c,1:k));
            end
        end
    end
end

% Reconstruct the decimated image collection

```

```

ReconstructedA = waverec2(imageR,S,ftype);

%% Plot the reconstruction next to the average image
figure(1)
subplot(1,2,1); subimage(ReconstructedE,[min(min(ReconstructedE))
max(max(ReconstructedE))]); axis off
title('Reconstructed Image','FontSize',16); axis tight
subplot(1,2,2); subimage(I_ave,[min(min(I_ave)) max(max(I_ave))]); axis
off
title('Average Image','FontSize',16); axis tight

%%
figure(2)
subplot(2,2,1);
subimage(image_stack(:,:,1),[min(min(image_stack(:,:,1)))
max(max(image_stack(:,:,1)))]); axis off
title('Horizontal Collimator Orientation Image','FontSize',16); axis
tight
subplot(2,2,2);
subimage(image_stack(:,:,5),[min(min(image_stack(:,:,5)))
max(max(image_stack(:,:,5)))]); axis off
title('Vertical Collimator Orientation Image','FontSize',16); axis
tight
subplot(2,2,3); subimage(ReconstructedE,[min(min(ReconstructedE))
max(max(ReconstructedE))]); axis off
title('Reconstructed Image w/ Edge Enhancement','FontSize',16); axis
tight
subplot(2,2,4); subimage(ReconstructedA,[min(min(ReconstructedA))
max(max(ReconstructedA))]); axis off
title('Reconstructed Image w/ Artifact Removal','FontSize',16); axis
tight

figure(3)
subplot(1,2,1); subimage(ReconstructedE,[min(min(ReconstructedE))
max(max(ReconstructedE))]); axis off
title('Reconstructed Image','FontSize',16); axis tight

t1 = now;
dur = t1 - t0; dur = days(dur); dur = minutes(dur);
calc_dur_message = ['Calculation Time: ', num2str(dur),' minutes\n'];
filter_message = ['Filter used: ', num2str(ftype)];
disp(calc_dur_message), disp(filter_message), disp(['Maximum decomp
level: ',num2str(level)])

```

APPENDIX C

DISCOVERY OF THE NEUTRON

James Chadwick discovered the neutron in 1932, and three years after that discovery the first image using neutrons was created from the work of Hartmut Kallmann and Ernst Kuhn [57]. The discovery of the neutron has changed the world around us in innumerable ways, but the most palpable have been political, scientific, and economic. The single most notorious use of this astounding discovery was the creation of the atomic weapon, but that is another story that is best left to professional historians and this author would recommend the reader refer to “The Making of the Atomic Bomb” by Richard Rhodes for further enlightenment on the subject of the birth of the atomic age. Ernst Rutherford is often credited as the first person to postulate the existence of neutral particles within the nucleus of every atom (except hydrogen), but it was Nernst who first gave the concept the name neutron (although his account of it being electrically neutral and massless made his idea closer to the neutrino). In fact, it was Rutherford’s published work on the nuclear structure of the atom in 1911 that started to fill in the edges of the puzzle that would form a more coherent model of the atom. After 1911, it was apparent that another particle must be present in the nucleus to account for the atomic masses of the elements. Nine years after his seminal publication, Rutherford made a startlingly accurate prediction of the basic properties: an atomic mass of one, and a neutral electric charge. He later went on to muse about more massive neutral particles with masses of 2, 3, and 4 atomic mass units, yet he was not alone in this hypothesis. A

year later, in 1921, W. D. Harkins made the same assertion, and around the same time three separate authors brought forth theoretical neutral particles of integer atomic mass. Finally, in 1930, Bothe and Becker discovered that a highly penetrating radiation came from the interaction of alpha particles on beryllium. This discovery was one of the corner stones for the experimental discovery of the neutron because it takes a reliable radiation source to make such a discovery. Irene Curie repeated this experiment the following year, but made the assumption that this new radiation was totally comprised of gamma rays. The pace of advancement quickened in 1931 with the discovery that if the radiation from the beryllium was shielded by lead or aluminum there was no discernable attenuation, but if a block of simple paraffin wax was placed in front of the detector, energetic protons were ejected towards the detector. The discovery by Curie and Joliot paved the way for James Chadwick to put the puzzle together since he now had all of the pieces necessary for its completion [57]. On February 27, 1932, Chadwick's letter to the editor of *Nature* was published on the "Possible Existence of a Neutron," in response to the claims by the Curie-Joliot group that the radiations from the alpha and beryllium reaction were gamma rays [58]. A month after this rebuttal came an admission from the Curie-Joliot pair that the character of the radiation emission from beryllium was indeed complex, which served almost as an apology. On June 1, 1932 Chadwick fired the final shot in one of the greatest scientific rivalries for discovery when Chadwick published his article confidently titled "The existence of the neutron." This article bore witness to observations made by Chadwick on the recoil atoms produced by the neutron radiation and produced calculations that determined the neutron should be between 1.005 and

1.008 atomic mass units. This was a smashing victory for science: four significant figures. The currently accepted mass of the neutron is 1.00866491600(43) atomic mass units.